Title

The Impact of Large-Scale Circulation on Recent Rapid Climate Changes in High Northern Latitudes

Permalink

https://escholarship.org/uc/item/3hv137vb

Author

Li, Zhe

Publication Date

2024

Peer reviewed|Thesis/dissertation

UNIVERSITY OF CALIFORNIA

Santa Barbara

The Impact of Large-Scale Circulation on Recent Rapid Climate Changes in High Northern Latitudes

A dissertation submitted in partial satisfaction of the
requirements for the degree Doctor of Philosophy
in Marine Science

by

Zhe Li

Committee in charge:
Professor Qinghua Ding, Chair
Professor Timothy DeVries
Professor Charles Jones

June 2024

The dissertation of Zhe Li is approved.

Timothy DeVries

Charles Jones

Qinghua Ding, Committee Chair

June 2024

The Impact of Large-Scale Circulation on Recent Rapid Climate Changes in High Northern Latitudes

by

Zhe Li

ACKNOWLEDGEMENTS

First and foremost, I would like to express my sincere appreciation to my advisor and committee chair, Professor Qinghua Ding, for his never-ending support and guidance throughout my PhD. He is an exceptional professor, always brimming with research ideas. He gave me the space to develop my own interests and always offered insightful advice and support whenever I needed it. His guidance extended beyond academics to life itself and the way I approach things, helping me grow from a naive student into a potential researcher. Thank you so much Qinghua, for encouraging me to persist in my academic goals. Your admission decision six years ago has truly changed my life. I am really happy to be part of your group for six wonderful years at UCSB.

I also would like to thank my committee members, Professors Charles Jones and Timothy DeVries for their time, effort, and feedback, which greatly improved this work. They were always available for discussions, not only about my research but also other questions I had as a graduate student. Thanks to your timely feedback and invaluable time.

Many thanks to teammate, roommates, and all of my friends in the US, UK, Australia, and China, who shared happiness and encouragement to me through all the ups and downs of my PhD. Special thanks to Yujie, for always being there and supporting me through so many days and nights.

Lastly, I want to dedicate this dissertation to my mother, Longhui Mei, and my father, Yueping Li. Thanks for bringing me to this world and being my safe harbor. Your respect and support for all my decisions mean everything to me. Thanks for your unconditional love. I hope I can make you proud. Special thanks and love go to my dear grandpa, who sadly passed

away during my PhD. I deeply regret not being able to be with him in his final days or share this moment with him. But I know he would be so happy for me and proud of this achievement.

To my mother, Longhui Mei, and my father, Yueping Li

To the memory of my grandpa, Zongtang Li

VITA OF ZHE LI
June 2024

EDUCATION

Bachelor of Arts in Marine Science, Ocean University of China, June 2018

Bachelor of Arts in Marine and Antarctic Science, University of Tasmania, June 2018

Master of Arts in Data Science, University of California, Santa Barbara, June 2024

Doctor of Philosophy in Marine Science, Emphasis in Climate Sciences and Climate Change, University of California, Santa Barbara, June 2024

PROFESSIONAL EMPLOYMENT

2019-2024: Graduate Student Researcher, Earth Research Institute, University of California, Santa Barbara

2019-2023: Teaching Assistant, Department of Geography, University of California, Santa Barbara

PUBLICATIONS

Li, Z., Ding, Q., Steele, M., & Schweiger, A. (2022). Recent upper Arctic Ocean warming expedited by summertime atmospheric processes. *Nature communications, 13*(1), 362.

Topál, D., Ding, Q., Ballinger, T. J., Hanna, E., Fettweis, X., **Li, Z.**, & Pieczka, I. (2022). Discrepancies between observations and climate models of large-scale wind-driven Greenland melt influence sea-level rise projections. *Nature Communications, 13*(1), 6833.

Ballinger, T. J., Moore, K., Ding, Q., Butler, A. H., Overland, J. E., Thoman, R. L., Baxter, I., **Li, Z.**, & Hanna, E. (2024). Simultaneous Bering Sea and Labrador Sea ice melt extremes in March 2023: A confluence of meteorological events aligned with stratosphere-troposphere interactions. *EGUsphere [preprint], 2024*, 1-22.

Wang, Z., Ding, Q., Wu, R., Ballinger, T. J., Guan, B., Bozkurt, D., Nash, D., Baxter, I., Topal, D., **Li, Z.**, Huang, G., Chen, W., Chen, S., Cao, X. Role of atmospheric rivers in shaping long-term Arctic moisture variability. (in revision, *Nature Communications*)

Li, Z., Ding, Q., Ballinger, T. J., Topál, D., Baxter, I. Atmospheric-driven processes in shaping long-term climate variability in Greenland and the broader subpolar North Atlantic. (in revision, *Journal of Climate*)

Li, Z., Ding, Q. A global poleward shift of atmospheric rivers. (under review, *Science Advances*)

Baxter, I., Ding, Q., Ballinger, T., Wang, H., Holland, M., **Li, Z.**, Wu, Y., Feldl, N., Guan, B., Zhu, J. Sources and land capacitor effects mediating observed summer Arctic moistening and water vapor feedback. (Submitted, Nature)

AWARDS

UCSB Graduate Division Dissertation Fellowship, 2023

UCSB International Doctoral Recruitment Fellowship, 2018

FIELDS OF STUDY

Major Field: Ocean and Climate Dynamics

Studies in Climate Dynamics and Modeling with Professor Qinghua Ding

Studies in Ocean-Atmosphere Interactions with Professor Qinghua Ding and Dr. Michael Steele

Studies in Weather Extremes with Professor Qinghua Ding

ABSTRACT

The Impact of Large-Scale Circulation on Recent Rapid Climate Changes in High Northern Latitudes

by

Zhe Li

In recent decades, global warming, predominantly driven by anthropogenic forcing and arising from an energy imbalance due to increased radiative forcing from greenhouse gases, has profoundly impacted Earth's climate systems. This warming is most significant in high northern latitudes, manifesting in various ways, such as sea ice melt, upper ocean warming in the Arctic, the slowdown of the Atlantic Meridional Overturning Circulation (AMOC), Greenland ice sheet retreat, changes in extreme weather patterns and related moisture transport near the Arctic, etc. Previous studies have extensively focused on the role of CO_2 forcing in contributing to these changes, while the influence of internal atmospheric variability - large-scale atmospheric circulation - remains less explored. In particular, these phenomenon were studied separately, which hinders us from gaining a deeper insight into the large-scale climate dynamics behind recent rapid changes in the climate system of high northern latitudes. This dissertation addresses this gap by examining how large-scale atmospheric circulation influences these changes, ranging from studying high northern latitude oceans to understanding circulation-extreme weather interactions. Although these observed rapid

change appear to be disconnected, actually my analyses solidly suggest that they are physically connected by recent large-scale atmospheric circulation variability with dynamical sources in the tropics.

In the following sections, consisting of three components, I focus on recent rapid changes in high northern latitudes: I. upper Arctic Ocean warming; II. subpolar North Atlantic warming hole; III. a poleward shift pattern of atmospheric rivers (ARs) in the extratropics. In the first part, I investigate the role of large-scale circulation in warming the upper Arctic Ocean over the past 40 years. Observational and modeling analyses reveal that internal atmospheric variability, characterized by a multiyear trend in summertime circulation, has significantly contributed to upper ocean warming in the Arctic. Nudging experiments in which the wind fields are constrained toward the observed state suggest that this variability accounts for up to 24% of the warming from 1979 to 2018, and up to 60% from 2000 to 2018. This internal circulation variability is known to be partially driven remotely by tropical sea surface temperature forcing. The second part of this research examines how large-scale circulation shapes ocean-atmosphere interactions in the subpolar North Atlantic (SNA), a key region for atmospheric and oceanic heat exchange between the Arctic and subarctic, as well as for the maintenance of the AMOC. Analysis of observational datasets and model simulations highlights the dominance of regional atmospheric circulation, partially initiated by remote forcing from the tropical Pacific, in driving multidecadal climate variability in the SNA by modulating local atmosphere-ocean interactions and upper ocean heat transport in the region. To further understand moisture transport from low latitudes to the extratropics due to extreme weather events such as ARs, in the last part of this dissertation, I focus on how this large-scale circulation regulates short-term extreme weather variability (e.g. ARs) in the North Pacific

and Atlantic, even in a global scale. Diagnostic analysis indicates that low-frequency sea surface temperature variability in the tropical eastern Pacific, exhibiting a cooling tendency since 2000, drives this poleward shift of ARs, predominantly observed over mid-latitude oceans. Strengthened subtropical high pressures, maintained by a tropical-driven eddy-mean flow feedback, contribute to these observed AR changes.

TABLE OF CONTENTS

Introduction 1

A. Overview 1

A.1 Upper Arctic Ocean warming 1

A.2 Subpolar North Atlantic warming hole 3

A.3 A poleward shift of atmospheric rivers 4

A.4 Large-scale circulation in high northern latitudes 6

B. Dissertation Objectives 8

C. Permissions and Attributions 10

I. Recent Upper Arctic Ocean Warming Expedited by Summertime Atmospheric Processes 11

Abstract 11

A. Introduction 11

B. Methods 13

C. Results 26

C.1 Observed linkage between atmospheric circulation and upper ocean warming 26

C.2 Mechanisms linking JJA atmospheric changes with SON upper ocean temperature 32

C.3 Wind nudging experiments using CESM 34

C.4 Poleward ocean heat transport contribution 43

D. Discussion 46

II. Atmosphere-Driven Processes in Shaping Long-Term Climate Variability in Greenland and the Broader Subpolar North Atlantic 49

Abstract 49

A. Introduction 50

B. Methods 53

C. Results 59

C.1. Subpolar North Atlantic SST changes in observations and climate models 59

C.2. Observed and simulated linkage between SST and overlying atmospheric circulation 66

C.3. Underlying local mechanism driving the air-sea interactions 71

C.4. Remote forcing of the SNA air-sea interaction 78

D. Discussion 82

III. A Global Poleward Shift of Atmospheric Rivers 86

Abstract 86

A. Introduction 86

B. Methods 90

C. Results 96

C.1 Observed and simulated poleward shift of ARs 96

C.2 Statistical relationship between atmospheric circulation and AR frequency 102

C.3 Eddy-mean flow contribution to ARs poleward shift 106

C.4 Fingerprint analysis detecting roles of circulation and SST in regulating ARs 108

D. Discussion 112

Conclusions 117

A. Summary 117

B. Key Results 118

C. Future work 120

References 123

Introduction

A. Overview

A.1 Upper Arctic Ocean warming

High-latitude oceans and atmosphere are integral to the global climate system as they play a large role in the heat balance and carbon fluxes exchanges of the Earth. One of the most significant recent rapid climate changes in high northern latitudes is the rapid warming of the Arctic, Earth's northernmost region, which has undergone rapid warming at approximately twice the rate of the rest of the globe over recent decades (Cohen et al., 2014; Screen & Simmonds, 2010; Serreze & Barry, 2011), a phenomenon known as "Arctic Amplification" (AA). Recent study based on several observational datasets indicates that this rate has accelerated, with the Arctic now warming nearly four times faster than the global average (Rantanen et al., 2022). The primary drivers of AA include both local and remote anthropogenic forcings – such as the positive lapse rate, ice-albedo, and Planck feedbacks (Dai et al., 2019; Pithan & Mauritsen, 2014; Screen & Simmonds, 2010; Stuecker et al., 2018), oceanic heat exchange mechanisms (Beer et al., 2020; Chung et al., 2021), atmospheric and oceanic poleward heat transport (Beer et al., 2020; Y. Huang et al., 2017; Hwang et al., 2011; Kay et al., 2012), and possible interactions among these factors. Despite the limited data in the Arctic Ocean, significant oceanic warming trends, particularly in the Barents Sea, are evident from available observations and model simulations (Beer et al., 2020; Carmack et al., 2015; I. Polyakov et al., 2007; Shu et al., 2021; Skagseth et al., 2020; Steele et al., 2008; Timmermans et al., 2018; J. Zhang, 2005). This warming is a major contributor to the loss of sea ice (Årthun et al., 2019; Carmack et al., 2015; Lique, 2015; I. V. Polyakov et al., 2010;

Ricker et al., 2021; Timmermans et al., 2018) and is influencing changes in both oceanic and atmospheric circulations (Lozier et al., 2019; Shu et al., 2021). It raises growing concerns that a “new normal” of the Arctic will come soon, with more ice-free summers and longer melting seasons expected by the middle of this century (Jahn et al., 2024). These changes increase the risk of tipping points in the Arctic climate system that may eventually have knock-on effects on climate at the lower latitudes.

Two main mechanisms have been identified in previous studies to explain upper Arctic Ocean warming within the context of anthropogenic warming. The primary one is due to recent anthropogenically forced atmospheric warming and concurrent sea ice reduction, which cause more downwelling heat energy entering the Arctic Ocean and consequently accelerate the temperature rise of the upper ocean (Mayer et al., 2016; Steele et al., 2010; Timmermans et al., 2018; J. Zhang, 2005). The second one involves an oceanic process, where the climatological mean ocean circulation combines with warmed surface waters around the Arctic. These surface waters, having absorbed extra atmospheric heat as part of the global warming response, transport this extra heat northward into the Arctic through time-mean northward flowing currents (Carmack et al., 2015; Oldenburg et al., 2018; I. V. Polyakov, Rippeth, et al., 2020; Serreze et al., 2007; Tsubouchi et al., 2021). This transport results in phenomena know as Arctic Atlantification and Pacification, referring to the inflow of anomalously warm Atlantic water through the Barents Sea and Pacific water through the Bering Strait, respectively (I. V. Polyakov, Alkire, et al., 2020). These processes are projected to persist under future global warming scenarios, as indicated by climate model projections (Årthun et al., 2019; I. V. Polyakov, Alkire, et al., 2020; Shu et al., 2021). However, the extent to which internal variability contributes to Arctic Ocean warming remains uncertain, as it is unknown to what degree these are the result of anthropogenic forcing, internal variability, or a combination of both. Particularly, the role of atmospheric internal variability in this context has yet to be thoroughly explored.

A.2 Subpolar North Atlantic warming hole

While global oceans, particularly the Arctic Ocean, are generally expected to warm under anthropogenic global warming, temperature trends are not uniform across the entire global oceans. Notably, a cooling trend in sea surface temperature (SST) has been observed in the subpolar North Atlantic (SNA) over the past century, resulting in the so-called North Atlantic warming hole (Drijfhout et al., 2012; Hansen et al., 2010; Rahmstorf et al., 2015). This coexistence of significant warming in the Pan-Arctic Ocean and this SST cooling tendency in the SNA presents a puzzling feature and is now one of the most active topics in studies of climate changes in high northern latitudes because these regions serve as a vital oceanic pathway between the Atlantic and Pacific Oceans and control a large portion of global ocean heat transport between the two basins. In particular, the climate simulations forced by historical atmospheric forcing and future warming scenarios also exhibit a similar warming hole pattern in the region (Gervais, Shaman and Kushnir, 2018; Menary and Wood, 2018; Chemke, Zanna and Polvani, 2020; Hu and Fedorov, 2020; Keil *et al.*, 2020), indicating the important role of anthropogenic forcing in driving SST variability in the SNA and highlighting the complexity of regional responses to global climate change.

The main causes of the observed recent SNA ocean cooling remain debatable. Most previous studies attribute it to anthropogenic forcing-induced AMOC slowdown and the resultant weaker ocean heat transport convergence into the SNA (Caesar et al., 2018; Chemke et al., 2020; Drijfhout et al., 2012; Gervais et al., 2018; Liu et al., 2020; Menary & Wood, 2018; Rahmstorf et al., 2015). However, the exact mechanisms linking the AMOC slowdown to the warming hole are not fully understood, particularly in light of the limited duration of AMOC measurements and the relatively modest extent of its observed slowdown so far (Wett et al., 2023). Other causes of the warming hole have also been raised, for example, enhanced ocean heat transport out of the North Atlantic into the Arctic Ocean (Keil et al., 2020), import of cold near-surface water masses from the Labrador Sea (Keil et al., 2020), intensified vertical mixing processes (Latif et al., 2022), and reduced net surface solar radiation caused by anthropogenic aerosols (Booth et al., 2012). Recent studies have further suggested that the warming hole pattern could be driven largely by both local and remote atmospheric processes, such as changes of local surface winds induced by local weather processes or atmospheric teleconnections linked to Indian Ocean warming (Josey et al., 2019; Hu & Fedorov, 2020b; Keil et al., 2020; He et al., 2022; L. Li et al., 2022). Although progress has been made to improve our understanding of atmospheric processes influencing the warming hole pattern, the dynamical mechanisms of atmospheric internal variability affecting SST variability in the SNA remains as an open question.

A.3 A poleward shift of atmospheric rivers

ARs are relative long and narrow corridors in the atmosphere that transport large amounts of water vapor across the globe, most commonly in the mid-latitudes and into Polar regions (Y. Zhu & Newell, 1994). These phenomena are associated with the compound interaction of strong extratropical storms and large-scale moisture transport, resulting in significant impacts on midlatitude weather extremes (Lamjiri et al., 2017; Ma, Norris, et al., 2020; McGowan et al., 2021; Waliser & Guan, 2017), poleward moisture transport (Y. Zhu & Newell, 1998), polar moistening (Mattingly et al., 2023; Nash et al., 2018), and various aspects of the extratropical hydrological cycle (Dettinger et al., 2011; Lavers & Villarini, 2015; Viale et al., 2018).

Anthropogenic forcing is widely recognized to induce a distinct poleward shift of extreme weathers, such as midlatitude/extratropical storms (Bengtsson et al., 2006; Chemke, 2022; Lehmann et al., 2014; Priestley & Catto, 2022; Tamarin & Kaspi, 2017; Tamarin-Brodsky & Kaspi, 2017; Wu et al., 2011; Yin, 2005) and tropical cyclones (Anjana & Kumar, 2023; Sharmila & Walsh, 2018; Studholme et al., 2022; Studholme & Gulev, 2018), particularly in the Southern Hemisphere (SH). The observed poleward shift in storm tracks has a parallel in the behavior of ARs, with studies increasingly discussing a concurrent poleward shift in ARs (Gao et al., 2016; Ma, Chen, et al., 2020). However, much of the research on poleward shift of ARs has focused on regional variability, such as the North Atlantic (Gao et al., 2016) and the Southern Hemisphere (Ma, Chen, et al., 2020), with limited attention to a global perspective. Given the interconnected nature of large-scale circulation changes across different regions, understanding AR changes from a global viewpoint is important for predicting their future impacts on the hydrological cycle and associated extremes.

Previous studies primarily attribute the regional shift of ARs to the poleward movement of the westerly jet induced by global warming and additional force due to ozone depletion in the SH (Gao et al., 2016; Ma, Chen, et al., 2020). However, the dominant underlying mechanism driving the global poleward shift of ARs over the past decades is still under debate. Whether the existing theories, that emphasize enhanced moisture concentration and static stability in the atmosphere, as well as a poleward shift in the westerly jet and storms, can confidently explain all key features of the observed global AR changes still remains an open question. The complexity of AR dynamics is yet to be fully understood, especially considering observed variability was also strongly subject to tropical internal variability, such as El Niño-Southern Oscillation (ENSO) and the Pacific Decadal Oscillation (PDO) (G. Chen & Held, 2007; Lu et al., 2008; Staten et al., 2018), which are able to significantly regulate the location and strength of midlatitude jets and width of the Hadley circulation. These independent or interconnected dynamics, originating from both anthropogenic and internal forcing, complicate attribution analyses and emphasize the further need for a better understanding of the causal relationship between different climate drives and observed changes in ARs, particularly the role of tropical-extratropical teleconnections in the global poleward shift of ARs.

A.4 Large-scale circulation in high northern latitudes

Large-scale atmospheric circulation plays a crucial role in recent rapid climate changes observed in high northern latitudes. The Arctic has exhibited a trend toward higher summertime pressure anomalies since 1979. One explanation links these anomalies to a teleconnection from the tropics, which propagates northward via an atmospheric Rossby-wave-train, the so-called Pacific-Arctic teleconnection (PARC) (Baxter et al., 2019; Ding et al., 2014, 2019; Y. Huang et al., 2021). This teleconnection exerts a warming effect through the adiabatic decent of air from the middle to upper troposphere that warms the near surface atmosphere and melts sea ice by regulating temperature, humidity, clouds, and downward longwave radiation in the Arctic atmosphere (Baxter et al., 2019; Ding et al., 2014, 2019; Y. Huang et al., 2021). The PARC, in its positive phase, exhibits a wave train emanating from the tropics to the Arctic, allowing for cold SST anomalies over the eastern tropical Pacific Ocean to remotely enhance Arctic warming near Greenland (Baxter et al., 2019). This process largely arises from internal variability and explains 40% of the trend in September sea ice loss since the 1980s (Ding et al., 2019). It is reasonable to expect that this process also has an impact on upper ocean temperature in high northern latitudes either via the ice-albedo effect or via potential impacts on the northward transport of oceanic heat. In addition, this high pressure has exhibited more complex behaviors over the past century and its spatial pattern has a strong loading over the North Atlantic (Ding et al., 2014; Feng et al., 2021), which may exert a forcing on local SST variability. Given the essential role of tropical-high latitude teleconnections in bridging the impact of tropical SST forcing with the high latitudes' ocean and atmosphere, the remote effects of tropical Pacific Ocean SST are also expected to act as another novel forcing for the warming Arctic-cooling SNA coexistence. These teleconnections may also play a crucial role in the dynamics of ARs, as the tropical-extratropical connections via ENSO can potentially drive the poleward shift pattern of ARs, especially in the North Hemispheric extratropics. This emphasizes the interconnectedness of the tropical and high-latitude systems and their impact on weather and climate variability.

However, the detailed processes linking this atmospheric internal variability with upper ocean temperature and extreme weather events in high northern latitudes via either local atmospheric processes or remote tropical effects remain unexamined. Because interactions between anthropogenically forced and internally generated processes and feedback are complex, it is often difficult to identify a clear cause-and-effect relationship. Current climate models own some limitations in simulating observed changes in atmospheric circulation, ocean temperature, and ARs in high northern latitudes, complicating our estimates of the sensitivity of each physical process associated with the warming Arctic-cooling SNA coexistence and ARs poleward shift. These limitations still pose key projection uncertainties.

Therefore, a better understanding of the relative roles of each forcing on recent rapid climate changes in high northern latitudes is desirable.

B. Dissertation Objectives

The recent rapid climate changes in high northern latitudes, including the observed coexistence of Arctic Ocean warming and SNA cooling, have attracted ample attention. However, the detailed mechanisms explaining these oceanic features remain unclear, with much of focus in previous studies being on their anthropogenic origins. In addition, while the poleward shift of ARs has been discussed, particularly in the North Atlantic and the SH, studies predominantly focus on regional variability and attribute these regional changes to the poleward movement of the westerly jet induced by global warming. **Therefore, the overarching goal of this dissertation is to assess the impact of large-scale atmospheric circulation on high northern latitude oceans and ARs by examining the causal dynamic mechanisms**. This research aims to elucidate the physical mechanisms driving the observed coexistence of Arctic Ocean warming (Chapter I) and SNA cooling (Chapter II) through wind-driven adiabatic processes related to large-scale atmospheric circulation and its remote linkage with tropical forcing, as well as changes in ARs in the high northern latitudes, even in the global scale (Chapter III). By using observational data and climate model simulations, this study seeks to identify the relative roles of anthropogenic forcing and internal variability in shaping these climate phenomena in high northern latitudes and to improve the predictive capabilities of climate models.

The research objectives of this dissertation are outlined as follows:

1. Investigate how atmospheric circulation shapes recent sea ice melting and upper ocean warming in the Arctic.

2. Examine the sensitivity of the SNA warming hole to local atmospheric forcing jointly with oceanic processes and the underlying mechanisms, including the importance of eastern tropical Pacific Ocean SST to the formation of the SNA warming hole through the Pacific-North Atlantic atmospheric teleconnection.
3. Understand the recent poleward shift of ARs in high northern latitudes and even in the global scale and its related climate-weather interactions.

The first chapter of this dissertation focuses on the atmosphere-ocean interactions in the Arctic. By using observational and modeling analyses, this chapter aims to quantity the contribution of internal atmospheric variability to recent Arctic Ocean warming and assess its implications for sea ice-albedo feedback and temperature trends. Nudging experiments are utilized to isolate the effects of anthropogenic forcing and internal variability on Arctic Ocean warming.

The second chapter examines the physical mechanisms behind the SNA warming hole. This involves analyzing the sensitivity of the SNA warming hole to local atmospheric forcing and oceanic processes. The chapter aims to understand the importance of eastern Pacific Ocean SST to the formation of the SNA warming hole through the Pacific-North Atlantic atmospheric teleconnection. By analyzing observational datasets and CMIP6 model simulations, this chapter explores the contributions of AMOC slowdown, oceanic heat transport, and atmospheric circulations (e.g., tropical influences) to the SNA warming hole. A new model experiment is conducted to isolate the impact of large-scale winds on regional climate variability, with a focus on atmosphere-ocean interactions.

The final chapter focuses on recent poleward shift of ARs in high northern latitudes and their related climate-weather interactions. Through diagnostic analysis of reanalysis data and large ensemble simulations, this chapter aims to identify the driving mechanisms behind the observed global changes in AR patterns, focusing on the poleward shift of ARs and its relation to large-scale atmospheric circulation changes. This chapter will assess the performance of climate models in replicating AR features and their projections under future warming scenarios, highlighting the role of tropical-extratropical teleconnection dynamics and climate-weather interactions.

C. Permissions and Attributions

1. The content of chapter 1 is the result of a collaboration with Qinghua Ding, and has previously appeared in Nature Communications (Li et al., 2022). It is reproduced here with the permission of Springer Nature: https://www.nature.com/articles/s41467-022-28047-8.

I. Recent Upper Arctic Ocean Warming Expedited by Summertime Atmospheric Processes

Material adapted from: ‘Li et al., Recent upper Arctic Ocean warming expedited by summertime atmospheric processes, Nature Communications, published [2022], [Springer Nature]’

Abstract

The observed upper (0 – 50 m) Arctic Ocean warming since 1979 has been primarily attributed to anthropogenically driven changes in the high latitudes. Here, using both observational and modeling analyses, we demonstrate that a multiyear trend in the summertime large-scale atmospheric circulation, which we ascribe to internal variability, has played an important role in upper ocean warming in summer and fall over the past four decades due to sea ice-albedo effect induced by atmospheric dynamics. Nudging experiments in which the wind fields are constrained toward the observed state support this mechanism and suggest that the internal variability contribution to recent upper Arctic Ocean warming accounts for up to one quarter of warming over the past four decades and up to 60% of warming from 2000 to 2018. This suggests that climate models need to replicate this important internal process in order to realistically simulate Arctic Ocean temperature variability and trends.

A. Introduction

Recent global warming fueled by increasing anthropogenic greenhouse gases is most prominent in the Arctic with significant atmospheric (Cohen et al., 2014; Fyfe et al., 2013; Landrum & Holland, 2020; Perlwitz et al., 2015; Screen & Francis, 2016) and oceanic warming (Beer et al., 2020; Carmack et al., 2015; I. Polyakov et al., 2007; Shu et al., 2021a; Skagseth et al., 2020; Steele et al., 2008; Timmermans et al., 2018; J. Zhang, 2005) and pronounced sea ice and land ice melting (Notz & Stroeve, 2016; I. V. Polyakov et al., 2012; J. C. Stroeve et al., 2014; J. Stroeve & Notz, 2018; R. Zhang, 2015). Warming of the upper ocean in the Arctic is contributing to sea ice loss (Årthun et al., 2019; Carmack et al., 2015; Lique, 2015; I. V. Polyakov et al., 2010; Ricker et al., 2021; Timmermans et al., 2018) and changes of ocean circulation (Lozier et al., 2019; Shu et al., 2021). However, our understanding of Arctic upper ocean temperature variability in the past decades and its main drivers remains limited, with previous studies mainly focusing on two processes. The primary one is due to recent sea ice reduction, which allows the ocean to gain more heat (Mayer et al., 2016; Steele et al., 2010; Timmermans et al., 2018; J. Zhang, 2005). The secondary one involves ocean advection with heat transported into the Arctic Ocean by the time-mean northward-flowing currents (Carmack et al., 2015; Oldenburg et al., 2018; I. V. Polyakov, Rippeth, et al., 2020; Serreze et al., 2007; Tsubouchi et al., 2021).

While the above processes have been extensively examined in the context of anthropogenic warming, the role of internal variability in Arctic Ocean warming is unclear. In the past decades, a strengthened cyclonic oceanic circulation in the Eurasian sector has been observed (Lindsay & Zhang, 2005; Proshutinsky et al., 2015; Timmermans & Marshall, 2020) as well as a stronger Beaufort Gyre in the American sector (Krishfield et al., 2014; Proshutinsky et al., 2015; Timmermans et al., 2018; Timmermans & Marshall, 2020). However, it is unknown to what degree these are the result of anthropogenic forcing, internal variability, or a combination of both. In particular, the Arctic has exhibited a trend toward higher summertime pressure anomalies since 1979. One explanation links these anomalies to a teleconnection from the tropics which propagates northward via an atmospheric wave train, exerting a warming effect that melts sea ice by regulating temperature, humidity, clouds, and downward longwave radiation in the Arctic atmosphere (Baxter et al., 2019; Y. Huang et al., 2021). This process arises from internal variability and explains 40% of the trend in sea ice loss in September since the 1980s (Ding et al., 2019). It is reasonable to expect that this process also has an impact on upper ocean temperature either via the ice-albedo effect or via potential impacts on the northward transport of oceanic heat. However, the detailed processes linking this atmospheric internal variability with upper ocean temperature remain unexamined. Because interactions between anthropogenically forced and internally generated processes and feedback are complex, it is often difficult to identify a clear cause-and-effect relationship. Given the importance of upper ocean temperature in stabilizing and shaping the high latitude climate in the Arctic (Rigor et al., 2000; Smedsrud et al., 2021), a better understanding of the relative roles of each forcing in recent Arctic Ocean warming is desirable.

In this work, we investigate how atmospheric internal variability has regulated upper ocean temperature in the melting season over the last four decades. We seek a physical understanding of the underlying mechanism of atmospheric internal variability and a quantification of its contribution to the recent warming compared with that due to anthropogenic forcing.

B. Methods

B.1 Reanalysis and observation data

In situ observations of the upper ocean temperature are very limited and sparse in the Arctic Ocean compared to the North Atlantic (Uotila et al., 2019), which inhibits our ability to study the multi-decadal large-scale variability of climate diagnostics, such as heat and salinity budgets. However, observational constraints on future anthropogenic warming critically depend on accurate estimates of past ocean temperature change. Reanalyses are another tool that provide multi-variate dynamical consistency in both spatial and temporal dimensions (Storto et al., 2019). We primarily use the Ocean Reanalysis System 5 (ORAS5) (Zuo et al., 2019) in this study to investigate the changes in upper ocean temperature and heat transport and their relationship with atmospheric variability over the past four decades. The ORAS5 dataset (the horizontal resolution is about 0.25° × 0.25°) is constructed by the ECMWF global operational ensemble reanalysis system containing an eddy-permitting ocean and sea-ice system and the OCEAN5 system. Reprocessed sea surface temperature from HadISST2 and OSTIA operational, sea-ice concentration from OSTIA and OSTIA operation, in situ temperature/salinity profiles from EN4 with XBT/MBT correction and GTS operational, and satellite sea level anomaly from AVISO DT2014 with revised MDT are assimilated in this system via NEMOVAR (Mogensen & Balmaseda, 2012) using a 5 day assimilation window with a model time step of 1200s (Zuo et al., 2019). Global mean sea-level changes are constrained using AVISO DT2015 L4 MSLA and NRT. The atmospheric forcing of ORAS5 is derived from ERA-40 (before 1979), ERA-Interim (1979 – 2015), and ECMWF NWP (2015 – present) (Zuo et al., 2019). ORAS5 includes five ensemble members and covers the period from 1979 onwards. In this study, the ensemble mean of the five members is analyzed. Although various in situ observations are assimilated in ORAS5, there are only a limited number of temperature/salinity profiles in the EN4 product in the central Arctic Ocean, which may potentially degrade the accuracy of ORAS5 in reflecting real observations over the region.

To evaluate the ORAS5, we compare its upper (0 – 50 m average) ocean temperature changes in the Arctic Ocean over the period 1979 to 2018 with other widely used reanalysis products (SODA3.4.2 (Carton et al., 2018) & GECCO3 (Köhl, 2020)) and observation (WOA18 (Boyer et al., 2019)). All ocean temperatures used in the calculations are potential temperatures, and we convert in situ temperature from WOA18 to potential temperature to be consistent with other reanalyses. The trends of upper ocean temperature time series in ORAS5 and SODA3.4.2 are similar with 0.165°C per decade for ORAS5 and 0.187°C per decade for SODA3.4.2 (note the shorter time period from 1980 to 2016), both of which are smaller than that of GECCO3 (0.279°C per decade). However, more important for this study, the variabilities of temperature time series and spatial patterns of upper ocean temperature trends in the three reanalyses are consistent (Fig. I.1a & Supplementary Fig. I.1). Comparisons with 'observation' only dataset is complicated by the fact that WOA18 only provides decadal monthly means of temperature for three decades (1985 – 1994, 1995 – 2004, 2005 – 2017), but the decadal average of upper ocean temperature time series derived from ORAS5 over two decadal periods (1985 – 1994 & 1995 – 2004) are close to that in WOA18, while it is slightly larger than WOA18 over the period 2005 – 2017 (Fig. I.1a). Spatial patterns of long-term trends of upper ocean temperature derived from reanalyses are similar to WOA18 with pattern correlation coefficients of 0.74 for ORAS5, 0.65 for SODA3.4.2 and 0.64 for GECCO3 (and ORAS5 has the highest correlation), although GECCO3 exhibits stronger warming than WOA18 over the whole basin (Supplementary Fig. I.2). In addition, observational data from the UpTempO Buoy Project (Banzon et al., 2020) was used to compare with reanalyses and we find that they well replicate UpTempO upper ocean temperature variability from 2000 to 2017 (Fig. I.1a). Based on these evaluations, we believe that ORAS5 is a reliable data source for this study.

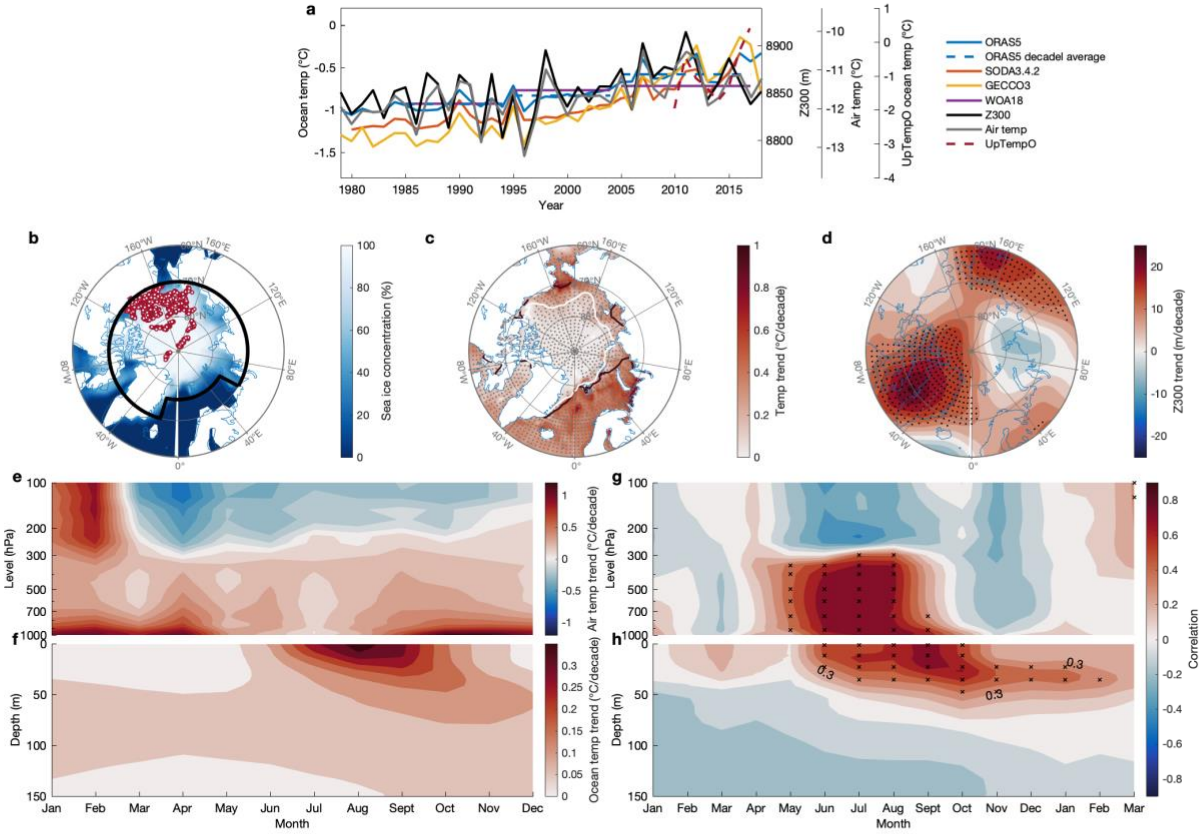

Figure I.1. Relationship between the summer large-scale atmospheric circulation and upper ocean temperature in fall. **a** The Arctic Ocean domain-average time series for SON upper (0 – 50 m average) ocean temperature (°C) using three different reanalysis data (ORAS5, SODA3.4.2, and GECCO3) and observation data (WOA18), JJA Z300 (m), and JJA tropospheric (surface to 300 hPa average) air temperature (°C) over the region circled by the black contour in **b** using the ERA5 reanalysis, and upper (0 – 50 m) ocean temperature (°C) using UpTempO buoy data (marked by red dots in **b**). **b** Climatology of JJA sea ice concentration from the National Snow and Ice Data Center (NSIDC) Nimbus-7 SMMR and DMSP SSM/I-SSMIS passive microwave monthly sea-ice product version 1 for the period 1979 – 2018. The area enclosed by the solid black line in **b** indicates the domain used for the following calculations. Red dots are UpTempO buoy data positions. **c** Linear trend (°C per decade) of SON upper ocean temperature from the ORAS5 reanalysis (1979 – 2018). September sea ice edges for the periods 1979 – 1988 mean (the first 10 years) and 2009 – 2018 mean (the last 10 years) are shown by the black and white contours, respectively. **d** Linear trend (m per decade) of JJA Z300 from the ERA5 reanalysis (1979 – 2018). **e-f** Monthly cross-section of the linear trend (°C per decade) of domain-average air temperature over 1000 – 100 hPa from the ERA5 reanalysis (1979 – 2018) in **e**, and ocean temperature (°C per decade) over 0 – 150 m depth from the ORAS5 reanalysis (1979 – 2018) in **f**. **g-h** Lead-Lag correlations of JJA domain-average tropospheric air temperature (gray line in **a**) with domain-average air temperature in **g**, and with domain-average ocean temperature in **h**, for each month (the last three months: Jan-Feb-Mar are the months in the next year) and layer (atmosphere: from 1000 – 100 hPa; ocean: from 0 – 150 m) for the period 1979 – 2018. All linear trends are removed in calculating the correlations in **g&h**. Black and gray stippling in all plots indicates statistically significant correlations or trends at the 95% confidence level.

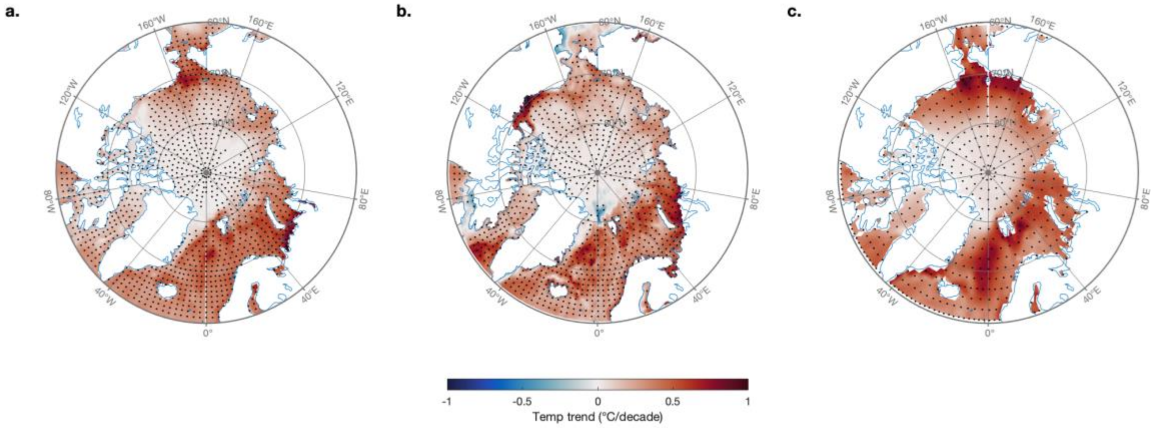

Supplementary Fig. I.1. Linear trend (°C per decade) of SON upper ocean temperature using three different reanalysis data (ORAS5 in **a**, SODA3.4.2 in **b**, and GECCO3 in **c**) (1979 – 2018). SODA3.4.2 only provides data from 1980 to 2016, which is different from the other two reanalyses. Black stippling in all plots indicates statistically significant trends at the 95% confidence level.

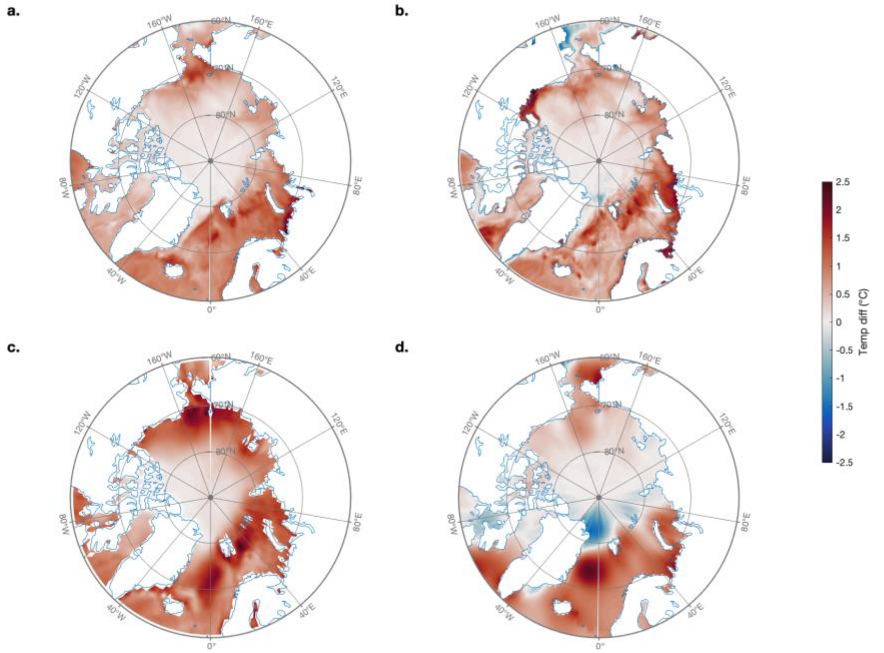

Supplementary Fig. I.2. Differences of SON upper ocean temperature between the periods 1985 – 1994 mean and 2005 – 2017 mean using three different reanalyses (ORAS5 in **a**, SODA3.4.2 in **b**, and GECCO3 in **c**) and observation data (WOA18 in **d**). SODA3.4.2 only provides data from 1980 to 2016, which excludes the data of year 2017 to calculate temperature difference.

We also use monthly circulation, air temperature, and radiation fields from 1979 to 2018 from ERA5 reanalysis data (Hersbach, Bell, Berrisford, Hirahara, Horányi, Muñoz-Sabater, et al., 2020). Monthly sea ice concentration is obtained from Nimbus-7 SSMR and DMSP SSM/I-SSMIS passive microwave data version-1 provided by the National Snow and Ice Data Center (NSIDC) (Cavalieri, Donald et al., 1996).

B.2 Maximum covariance analysis (MCA)

MCA (Bretherton et al., 1992; Wallace et al., 1992) is used to determine the dominant covarying patterns of high-latitude atmospheric circulation and upper ocean warming in the Arctic. MCA analysis is applied by using singular value decomposition on the temporal covariance matrix between JJA NH high-latitude (60° – 90°N) Z300 and SON upper (0 – 50 m average) ocean temperature over the Arctic (70° – 90°N). Simply put, MCA analysis can isolate the most coherent pairs of the spatial patterns and identify a linear relationship between two different fields that are most closely coupled. The leading modes show the spatial patterns and time series of the two fields that are optimally coupled. The corresponding squared singular value represents the squared covariance fraction (SCF), which indicates the relative importance of that pair of vectors in relationship to the total covariance in the two fields.

B.3 Radiation fluxes

Net downward heat flux (Q_{net}) is calculated as the following, with units of $\mathrm{W\ m^{-2}}$

$$Q_{net} = DLR - ULR + DSR - USR + SHF + LHF \tag{1}$$

where DLR and ULR are downwelling and upwelling longwave radiations, respectively; DSR and USR are downwelling and upwelling shortwave radiations, respectively; SHF is sensible heat flux; LHF is latent heat flux. All radiative flux variables are positive downward and represent heat transferred from the atmosphere to the surface.

B.4 Wind-nudging experiments using CESM1

Because we are interested in the contribution of wind forcing to upper ocean warming in the Arctic in our model simulations, we use 6-hourly ERA5 wind fields for nudging. The experiments consist of five 40-year historical runs from 1979 to 2018 using the CESM1 fully-coupled model (Hurrell et al., 2013). In these runs, Arctic (north of 60°N) atmospheric winds from the surface to the top of the atmosphere in the model are fully nudged to the corresponding 6-hourly ERA5 winds (the relaxation timescale of the nudging is about 6 hours) with various different sea ice initial conditions derived from a long (150 year) spin-up simulation, and there is no nudging effect everywhere else. Anthropogenic forcing is held constant in the nudging experiments and spin-up run at the level of year 2000 (i.e. CO_2 is set at 367 ppm) so that greenhouse gas concentrations throughout the integration is very close to the observed 40-yr averaged values (i.e. CO_2 at 369 ppm). To address the issue of "assimilation shock", the tendency of models to equilibrate to imposed winds, we first run a 150-year perpetual simulation with the model continuously nudged to winds in year 1979 in the Arctic (from the surface to the top of atmosphere) and forced by constant anthropogenic forcing from year 2000. In this spin-up, the model takes almost 100 years for the Arctic mean upper ocean temperature to adapt to wind fields and then varies stably around a constant level afterwards (Supplementary Fig. I.3). The model states on Jan. 1 of the last 5 years of this spin up are then separately used as initial conditions to reinitiate a set of new five members of 40-yr nudging simulations in which imposed winds in the Arctic are allowed to vary from 1979 to 2018. In this study, we focus on the ensemble mean of these five members to understand wind forcing on ocean temperature and other fields in the Arctic. In addition, one advantage of this set of simulations is that the POP2 of the CESM1 can simulate the solar shortwave radiation heat flux penetrating into the ocean boundary layer (Q_{short_bl}), which is calculated by the KPP vertical mixing scheme and not available in ORAS5. This variable will tell us how much of incoming shortwave flux at the surface can be absorbed by the whole depth of the ocean surface boundary layer in each oceanic grid based on the fraction of solar short-wave flux penetrating to the bottom of this layer (Van Roekel et al., 2018).

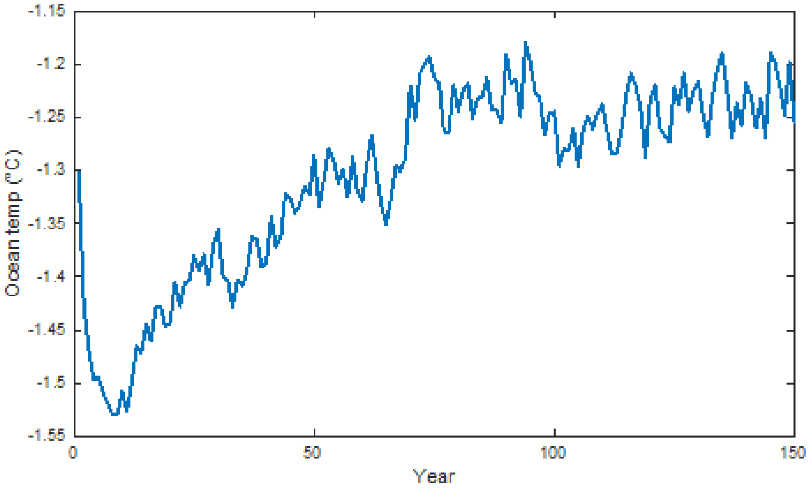

Supplementary Fig. I.3. The Arctic Ocean domain-average upper (0 – 50 m average) ocean temperature (°C) in SON during 150-yr spin-up perpetual run.

B.5 The mean sea ice and oceanic states simulated by wind-nudging experiments

Although we are interested in the anomalous response to imposed winds, an examination of the simulated sea ice and oceanic mean states is necessary to ensure that the model can capture similar climatology in ORAS5 to prepare the model to reasonably respond to imposed forcing. We examine the long-term (1979 – 2018) mean March and September sea ice extent in observations (Supplementary Fig. I.4a&b) and the ensemble mean of five 40-yr nudging experiments (Supplementary Fig. I.4c&d). Nudging experiments appear to have a good skill to capture the observed sea ice states over the Arctic, with slightly smaller extent in September than observed. Supplementary Fig. I.5 shows a comparison of the long-term mean (1979 – 2018) February and August ocean temperature and salinity in ORAS5 reanalysis (a, c, e, & g) and wind nudging experiments (b, d, f, & h) over a vertical cross-section from Alaska to Svalbard via the North Pole. The model captures the inflow of warm, salty Atlantic Water near Svalbard, although its salinity is too high at the inflow and its depth interval within the Arctic Ocean is deeper than that in ORAS5. A realistic signature of the Beaufort Gyre between Alaska and the North Pole is seen as concave up (i.e., downwelling) isohaline and isothermal contours. Ocean surface summer warming and freshening is also captured in the model. However, deficiencies still remain: One is the absence of a warm summer Pacific Water layer in the Canada Basin in the model and the other is the cooler mean state of upper ocean temperature in the model. These are common issues even in some regional models (Steele et al., 2011).

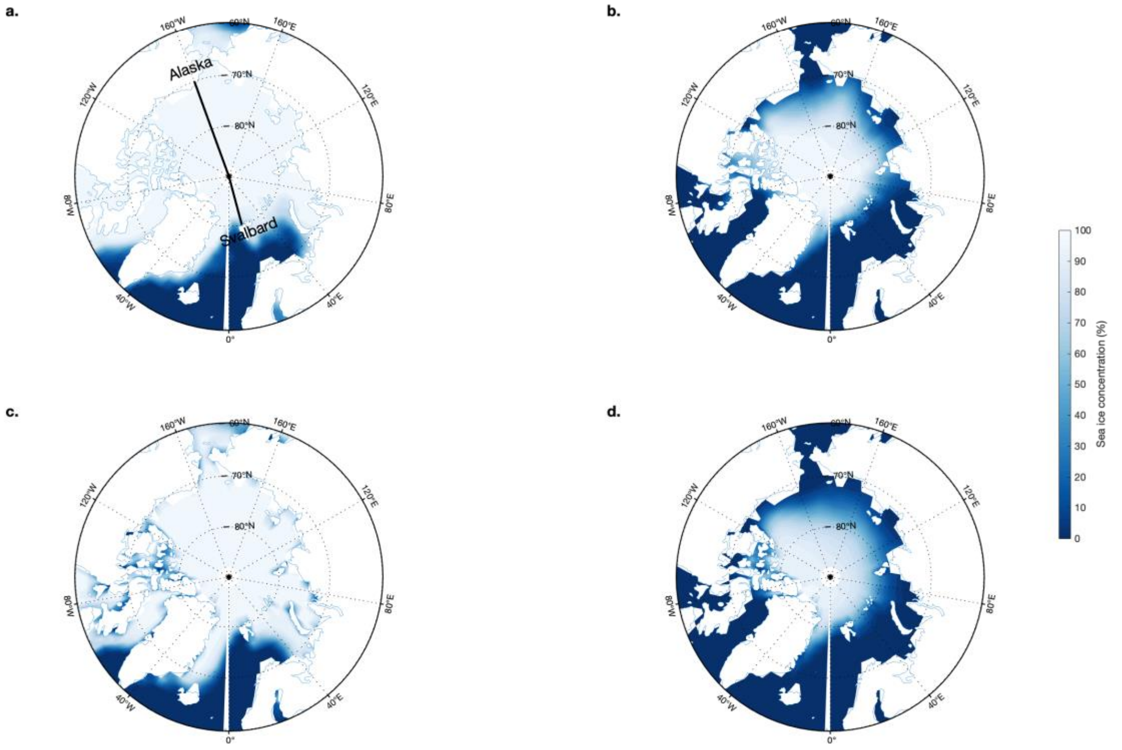

Supplementary Fig. I.4. a&c Climatology of March sea ice concentration from the NSIDC Nimbus-7 SMMR and DMSP SSM/I-SSMIS passive microwave monthly sea-ice product version 1 in **a** and from the ensemble average of the five wind nudging experiments in **c** for the period 1979 - 2018. **b&d** Climatology of September sea ice concentration from the NSIDC Nimbus-7 SMMR and DMSP SSM/I-SSMIS passive microwave monthly sea-ice product version 1 in **b** and from the ensemble average of the five wind nudging experiments in **d** for the period 1979 - 2018. The solid black line in **a** from Alaska to Svalbard is used in **Supplementary Fig. I.5** for the vertical cross section plots.

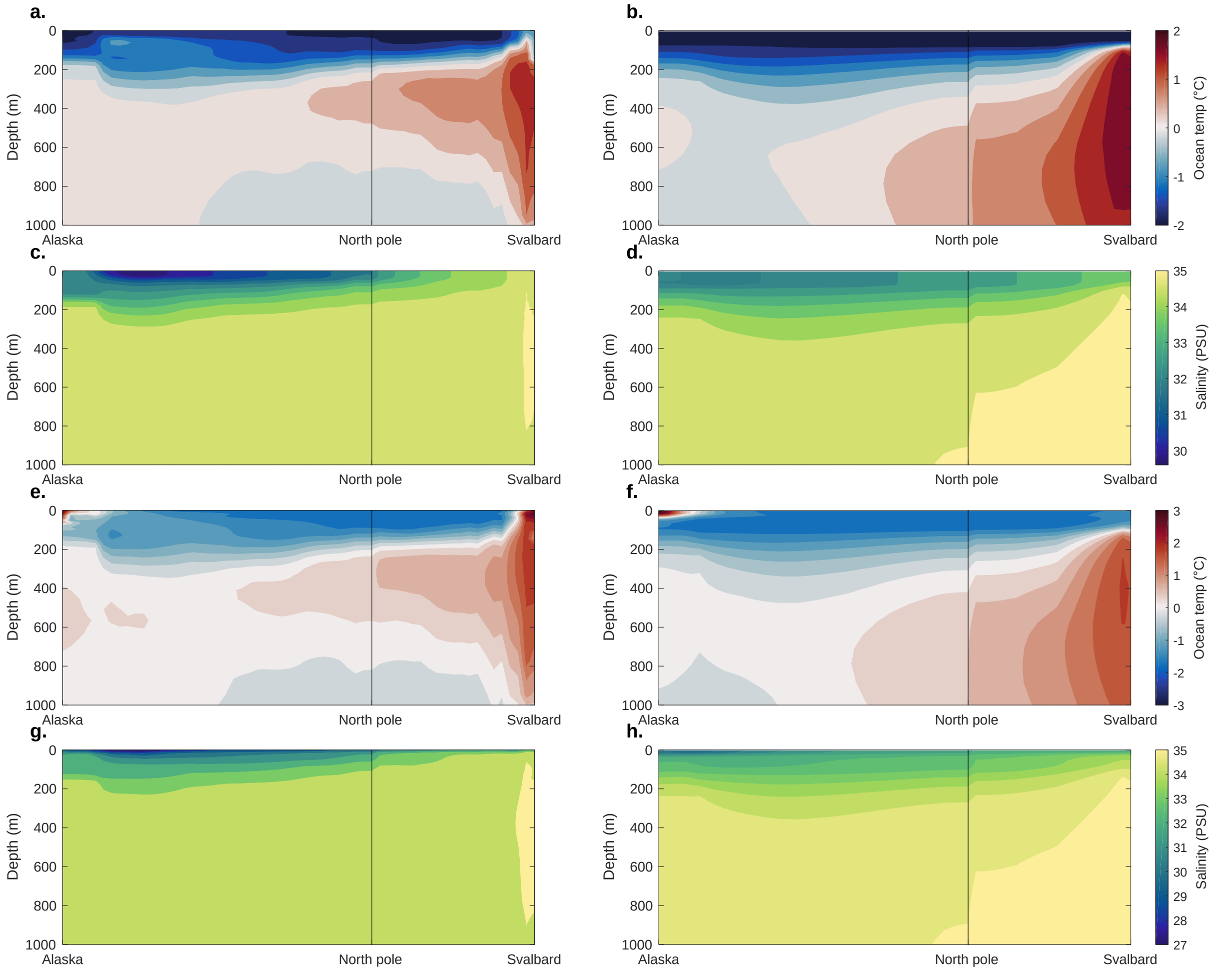

Supplementary Fig. I.5. a&b Climatology of February ocean temperature over the years 1979 – 2018 for a vertical cross section Alaska-North Pole-Svalbard over 0 – 1000 m depth from the ORAS5 reanalysis in **a** and from the ensemble average of the five wind nudging experiments in **b. c&d** Same as **a&b** but for salinity**. e-h** Same as **a-d**, but for mean August.

B.6 Poleward ocean heat transport

For a given depth layer, poleward ocean heat transport (POHT) is calculated as the cross-section integral of temperature multiplied by meridional ocean velocity, seawater density and the specific heat capacity, with units of Watts:

$$\mathrm{POHT}(V_R, t) = \int_D^0 \int_{west}^{east} V(\theta - \theta_r) dz \cdot dx \cdot C_P \cdot \rho \tag{2}$$

where D is the depth of ocean which we take to be 50 m, V is temperature minus a reference temperature, C_P = 4200 $\mathrm{J} \cdot \mathrm{kg}^{-1} \cdot \mathrm{C}^{-1}$ is the seawater specific heat capacity, and ρ

is seawater density. We assume the density of ocean water as a constant 1027 $\mathrm{kg \cdot m^{-3}}$ for the Atlantic Gate and 1025 $\mathrm{kg \cdot m^{-3}}$ for the Pacific Gate because density has not changed much in reality. As prior works, we use θ_r = 0℃ for the Atlantic Gate (Årthun et al., 2019) and θ_r = -1.9℃ for the Pacific Gate (R. Woodgate et al., 2015; R. A. Woodgate, 2018; R. A. Woodgate et al., 2010, 2012). Cross sections are indicated by blue and green contours in the stereographic projection for the Atlantic Gate (15°W – 60°E longitude at 76°N latitude) and the Pacific Gate (170°E – 160°W longitude at 70°N latitude). We also split the POHT through the Atlantic Gate into two branches through the Fram Strait (15°W – 15°E longitude at 76°N latitude) and Barents Sea (20°E – 60°E longitude at 76°N latitude). The heat inflow in the upper 50 m through the Bering Strait is sufficient to modify the ocean temperature in the upper 50 m because the Bering Strait is only 50 m deep. Over the Atlantic sector, the variability of POHT through the Atlantic Gate from 0 – 300 m or 0 – 2500 m is similar to that in the upper 50 m because the Atlantic water inflow is largely barotropic (Supplementary Fig. I.6). Considering that the upper 50 m ocean temperature is the most sensitive to the heat inflow in the upper 50 m, we primarily focus on the POHT at this level in this study. We also note that there is a mismatch between the magnitudes of simulated POHT and that in ORAS5 through the two gateways. The main source of this mismatch appears to be the underestimated intensity of poleward volume transport in the model (Supplementary Fig. I.7d&e).

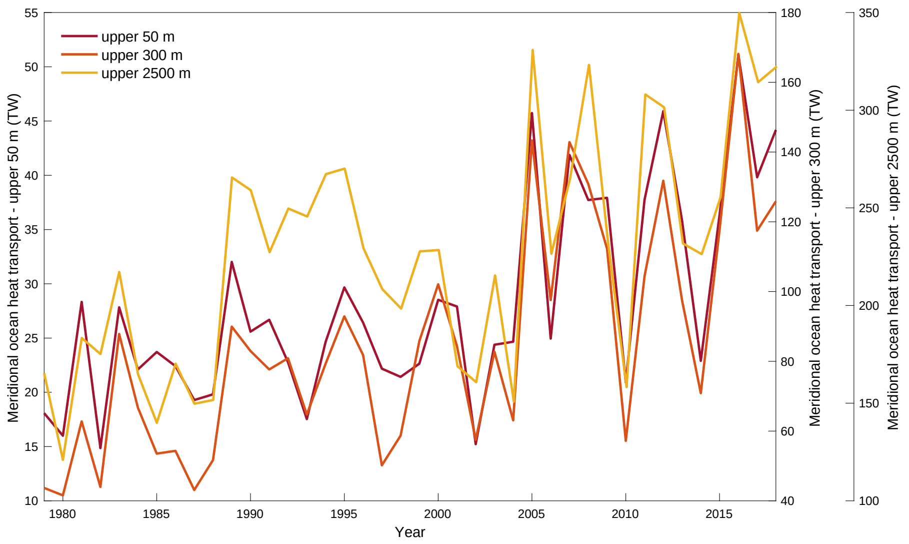

Supplementary Fig. I.6. SON POHT (TW) through the Atlantic Gate within the upper 50 m, 300 m, and 2500 m from 1979 to 2018 using the ORAS5 reanalysis.

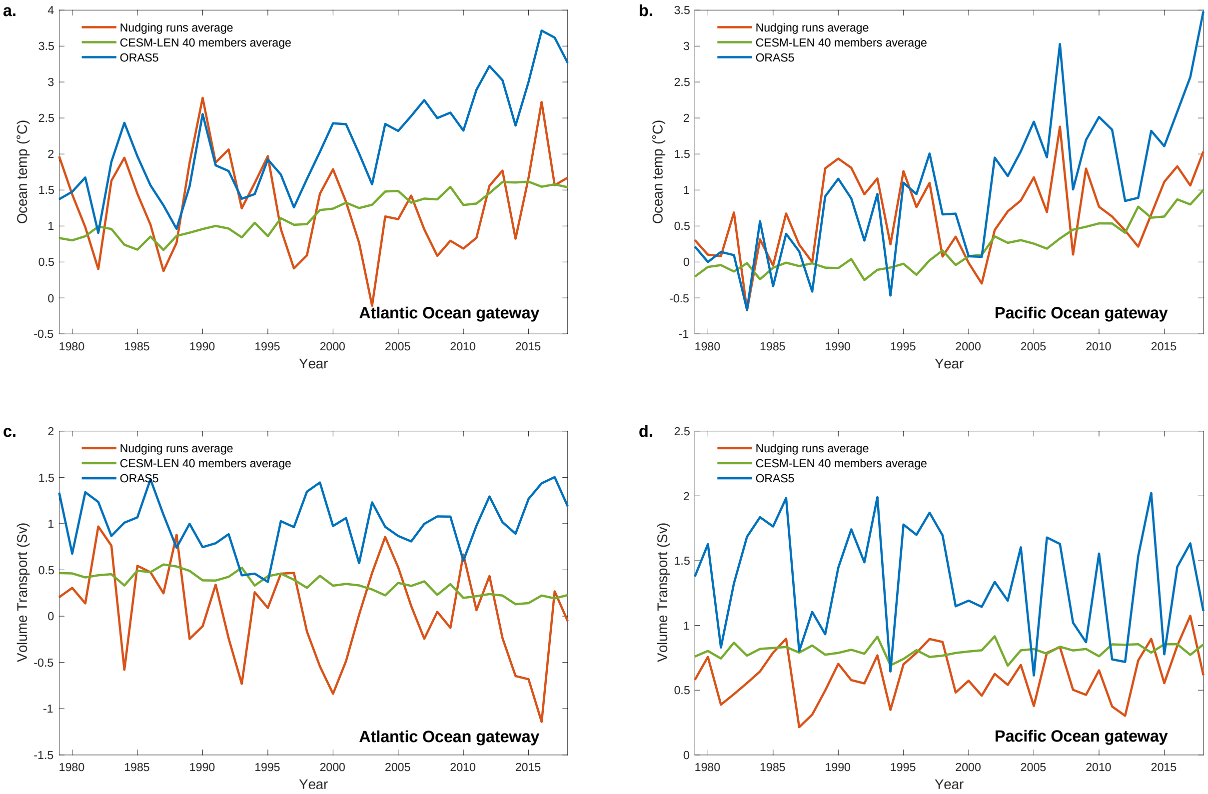

Supplementary Fig. I.7. **a&b** SON cross section-average upper (0 – 50 m average) ocean temperature (°C) along the Atlantic Ocean gateway in **a**, and along the Pacific Ocean gateway in **b** from the ensemble average of the five wind nudging experiments (red line), the CESM-LEN 40 members average (green line), and the ORAS5 reanalysis (blue line) for the period 1979 – 2018. **c&d** Same as **a&b** but for the poleward volume transport (Sv) in the upper 50 m in SON.

B.7 Significance of correlation

The statistical significance of the correlation coefficient accounts for the autocorrelation in the time series by using an effective sample size N^* (Bretherton et al., 1999):

$$N^* = N\frac{1-r_1r_2}{1+r_1r_2} \tag{3}$$

where N is the number of available time steps and r_1 and r_2 are lag-one autocorrelation coefficients of each variable. A confidence level of 95% is used in this study to determine the significance of correlations and composites.

C. Results

C.1 Observed linkage between atmospheric circulation and upper ocean warming

The Arctic Ocean exhibits strong warming trends and year-to-year variability of the upper 50 m in the last four decades in summer and fall (Steele et al., 2008) (Fig. I.1a). This layer, defined as the upper ocean in this study, resides above the Pacific Waters (PW) located between 50 to 150 m depth and Atlantic Waters (AW) located between 200 m and 800 m. Thus, its temperature variability impacts the overlying sea ice and the efficiency of the heat exchange between the ocean and atmosphere. To understand upper ocean temperature variability related to summertime atmospheric and sea ice processes, we focus on the area confined by the long-term mean (1979 – 2018) June-July-August (JJA) Arctic sea ice extent (approximated by black line in Fig. I.1b). Within this area, the upper ocean is fully covered by sea ice for large parts of the year but has some exposure to the atmosphere from June to October with the maximum in September when the sea ice reaches its minimum extent. Thus, an interaction between the atmosphere and the upper ocean is expected during these ice-free months.

Associated with recent atmospheric warming trends that are apparent throughout the year (Fig. I.1e), ocean warming trends over the upper 150 m feature a tilted downward intrusion starting from June-August at the surface and propagating downward toward 50 m by fall (i.e, by September-October-November, or SON; Fig. I.1f). This downward heat transfer suggests that recent fall upper ocean warming (Fig. I.1a) originates from more absorption of heat at the surface in summer (i.e, JJA) because the sea ice-albedo effect which is more efficient in summer allows stronger oceanic uptake of solar radiation during ice melting seasons. This connection operates well on interannual time scales, with the causal direction examined by a lead-lag relationship between JJA Pan-Arctic tropospheric (surface to 300 hPa) average air temperature and ocean temperature in each month and depth (Fig. I.1g&h). It is clear that JJA atmospheric warming significantly precedes upper ocean warming from early summer to the following fall and even winter since it takes time to melt sea ice and then warm the ocean due to the larger heat capacities of ocean and sea ice. This calculation suggests that atmospheric forcing drives ocean warming rather than the reverse in summer.

This subsurface fall warming is primarily confined to the Beaufort, Chukchi, and East Siberian Seas (hereafter collectively referred to the “Pacific Peripheral Seas Sector”, or PPSS) and the Laptev, Kara, Barents, Norwegian, and Greenland Seas (hereafter referred to as the “Atlantic Peripheral Seas Sector”, or APSS; Fig. I.1c). The former is the area where the most pronounced sea ice decline in the melting season has been observed since 1979 (Fig. I.1c). Concomitant with the trends in upper ocean warming is a trend in the atmospheric upper tropospheric circulation: for example, geopotential height at the tropopause at 300 hPa (Z300:

its variability is a measure of temperature variations of the entire air column below 300 hPa; a higher Z300 also means that the circulation changes toward a pattern with stronger anticyclonic movement in the Northern Hemisphere) has been rising over northeastern Canada and Greenland (Fig. I.1d). The calculation using the Arctic Ocean domain average variables suggests that the SON upper ocean (0 – 50 m average) temperature (using reanalysis data; see Methods) has a close association with summertime (i.e, JJA) values of both Z300 and tropospheric air temperature (Table I.1). A similar but slightly weaker relationship is observed between the domain average JJA upper ocean temperature with the simultaneous domain average Z300 and tropospheric air temperature (Table I.1). SON oceanic warming may reflect an accumulation of changes over JJA due to the larger heat capacities of ocean and sea ice. Thus, the JJA atmosphere – SON ocean connection becomes more significant than the simultaneous connection and the dynamics of this lag relationship will be the focus of this study.

	JJA Z300	JJA tropospheric air temp
SON upper ocean temp		
Corr (with trend)	0.56	0.74
Corr (without trend)	0.48	0.66
JJA upper ocean temp		
Corr (with trend)	0.53	0.69
Corr (without trend)	0.45	0.57

Table I.1. Correlations between the summer large-scale atmospheric circulation and upper ocean temperature in fall & summer. Correlations of JJA/SON Arctic Ocean domain-average upper (0 – 50 m average) ocean temperature with JJA domain-average Z300 and tropospheric (surface to 300 hPa average) air temperature with trends and without trends respectively.

To illustrate the lag process that links the JJA atmospheric circulation pattern to SON upper ocean temperature change, we correlate the domain average SON upper ocean temperature with the spatial fields of JJA Z300 and tropospheric air temperature in the Arctic respectively (Supplementary Fig. I.8a&b). An Arctic summer with higher-than-average Z300 and warmer tropospheric air temperature centered over Greenland and the Arctic Ocean appears to consistently precede a warmer-than-average upper ocean in the Arctic in SON (Supplementary Fig. I.8a&b). Importantly, the pattern derived from the detrended variables exhibits a very similar structure to that using raw data, suggesting that the impacts of the JJA atmospheric circulation on the SON upper ocean temperature change also exist on interannual and longer time scales. This domain average SON upper ocean temperature related circulation pattern shows a strong similarity with the linear trend of JJA Z300 field in the past 40 years and therefore upper ocean warming appears to be driven by the atmospheric circulation trend in JJA. Figure I.1g&h also indicate that atmospheric warming in JJA influences the ocean surface at zero lag, and influences deeper layers later i.e., in SON.

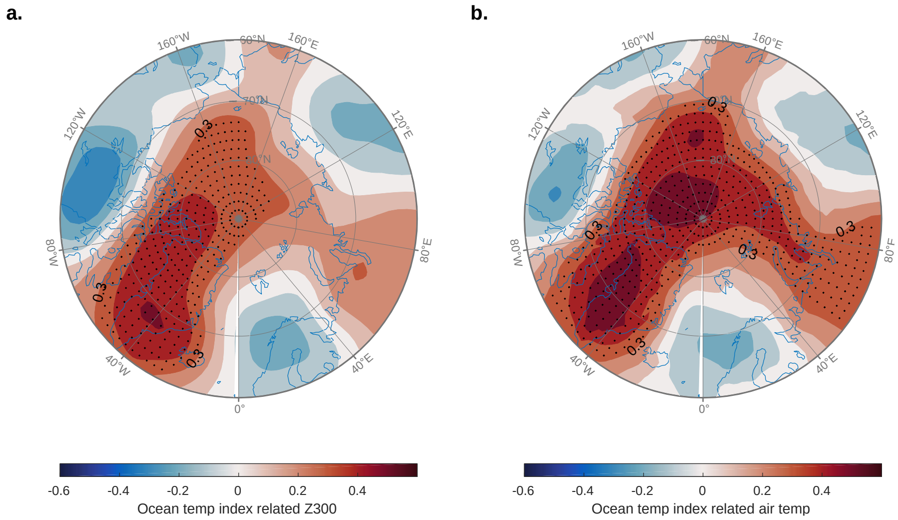

Supplementary Fig. I.8. Correlation of domain-average SON upper ocean temperature in **Fig. 1a** with the spatial fields of JJA Z300 in **a** and JJA tropospheric (surface to 300 hPa average) air temperature in **b** for the period 1979 – 2018. All linear trends are removed in calculating the correlations. Black stippling in all plots indicates statistically significant correlations at the 95% confidence level.

To investigate whether the links between atmospheric warming and ocean are tied to fundamental modes of variability with a spatially coherent structure, we performed a maximum covariance analysis (MCA) between the JJA atmospheric circulation and SON upper ocean temperature in the Arctic. Supplementary Fig. I.9a-c show results using detrended variables. The patterns and correlations are similar to those using raw data (not shown). The leading mode of MCA analysis accounts for the majority of covariance (36%, see Methods) and dominates the linkage of the two fields. The ocean temperature pattern of MCA1 exhibits increased temperature mostly in the PPSS and is closely coupled with a Z300 pattern characterized by a prominent high pressure over northeastern Canada and Greenland, which has been suggested by Ding et al. (2019) to be a critical driver of sea ice variability in the past decades (Supplementary Fig. I.9a&b). The MCA1 time series of the two patterns are highly correlated (r = 0.74) and are almost identical to the time evolution of detrended observed upper Arctic domain-average ocean temperature in SON (Supplementary Fig. I.9c). The Z300 and ocean temperature patterns revealed by the leading MCA mode feature a striking resemblance with the observed trend patterns in JJA Z300 and SON upper ocean temperature fields (Supplementary Fig. I.9a&b & Fig. I.1c&d), suggesting that there exists a physical link between changes in observed upper ocean temperature and the atmospheric circulation characterized by the Z300 pattern. Since the MCA analysis is performed on detrended data, the close match between the observed trends and the MCA patterns suggests that the observed trend to a substantial degree arises from internal variability rather than secular trends.

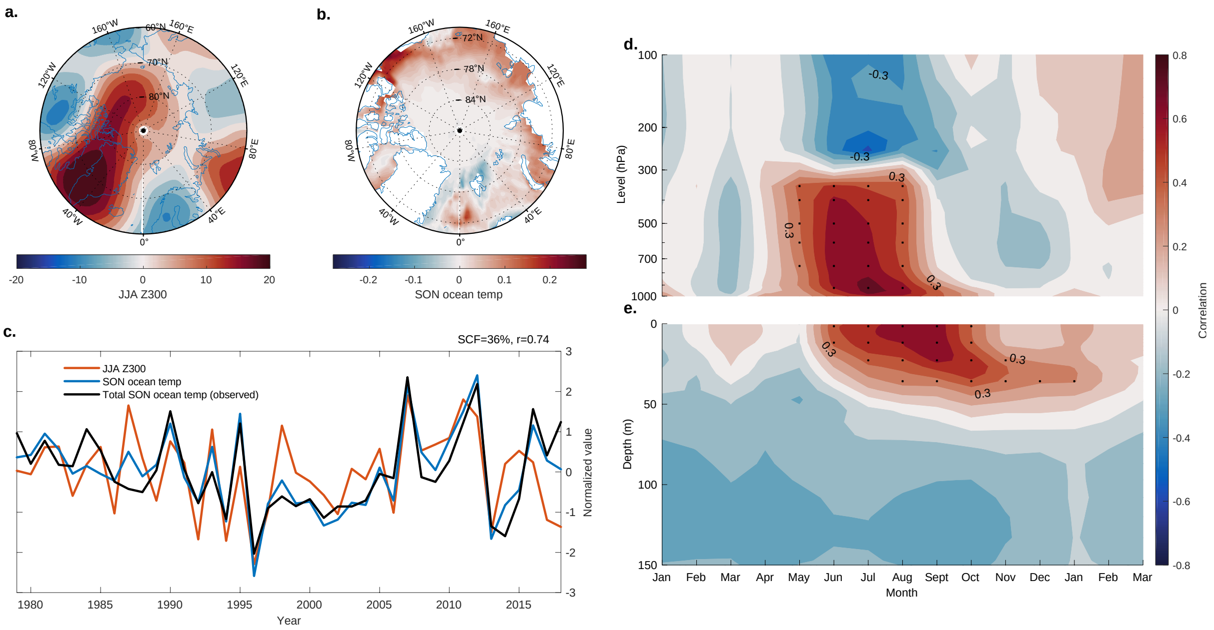

Supplementary Fig. I.9. a-c The leading patterns of covariability and their time series from a MCA of JJA Northern Hemisphere high-latitude (60° – 90°N) Z300 and SON upper (0 – 50 m average) ocean temperature in the Arctic (70° – 90°N) for the period 1979 – 2018, where all fields are detrended. The patterns of Z300 and ocean temperature that accompany the first MCA mode are shown in **a** and **b**, respectively. The normalized time series of the MCA1 JJA Z300 (red line) and MCA1 SON ocean temperature (blue line) patterns, and total SON domain-average upper ocean temperature from the reanalysis (black line) are shown in **c**. The squared covariance fraction (SCF) showed in **c**. indicates that the first mode accounts for 36% of the covariance, and the correlation between the time series of JJA Z300 and SON ocean temperature mode is 0.74. **d&e** Correlation of MCA1 JJA Z300 time series (red line in **c**) with domain-average air temperature in **d**, and with domain-average ocean temperature in **e**, for each month (the last three months: Jan-Feb-Mar are the months in the next year) and layer (atmosphere: from 1000 – 100 hPa; ocean: from 0 – 150 m) for the period 1979 – 2018. All linear trends are removed in calculating the correlations in **d&e**. Black stippling in all plots indicates statistically significant correlations at the 95% confidence level.

To further illustrate the association between atmospheric and oceanic temperature, we calculate the lead-lag correlation between the MCA1 JJA Z300 time series with domain-average air temperature within the Arctic for each month and layer (Supplementary Fig. I.9d&e). Prominent ocean temperature rise succeeding the JJA atmospheric warming starts to appear in early summer near the surface and then exhibits a strong downward intrusion into lower layers to ~ 50 m until the following fall and even winter (Supplementary Fig. I.9e). This lead-lag correlation pattern looks very similar to the temporal evolution pattern associated with the observed JJA tropospheric air temperature (Fig. I.1h) and long-term trend of upper ocean temperature in the Arctic Ocean (Fig. I.1f), suggesting the contribution of recent summertime atmospheric warming to the following upper Arctic Ocean warming in SON. These results collectively suggest that a portion of the SON upper ocean warming trend in the past decades results from JJA atmospheric circulation variability on an interdecadal time scale.

C.2 Mechanisms linking JJA atmospheric changes with SON upper ocean temperature

What processes link JJA atmospheric warming to SON upper ocean warming beneath? Ding et al. (2017) showed that a JJA high pressure anomaly can melt summer sea ice through increased downwelling longwave radiation at the surface. To investigate how a similar mechanism affects upper ocean temperature, we examine the surface energy transfer between the atmosphere and the ocean. Arctic domain averages of SON upper ocean temperature, September sea ice area (SIA), and JJA tropospheric average air temperature are highly correlated with JJA net downward heat flux (Q_{net}), all of which exhibit a patch of significant correlations over the Arctic Ocean (Fig. I.2a-c, positive for temperature (Fig. I.2a&c) and negative for sea ice area (Fig. I.2b)). Domain averages of ocean temperature, SIA, and air temperature co-vary with Q_{net} with detrended correlations of 0.73 to 0.88 (Fig. I.2d). This co-variability suggests that atmospheric warming during JJA first melts sea ice, and then warms the resulting open water in the following months.

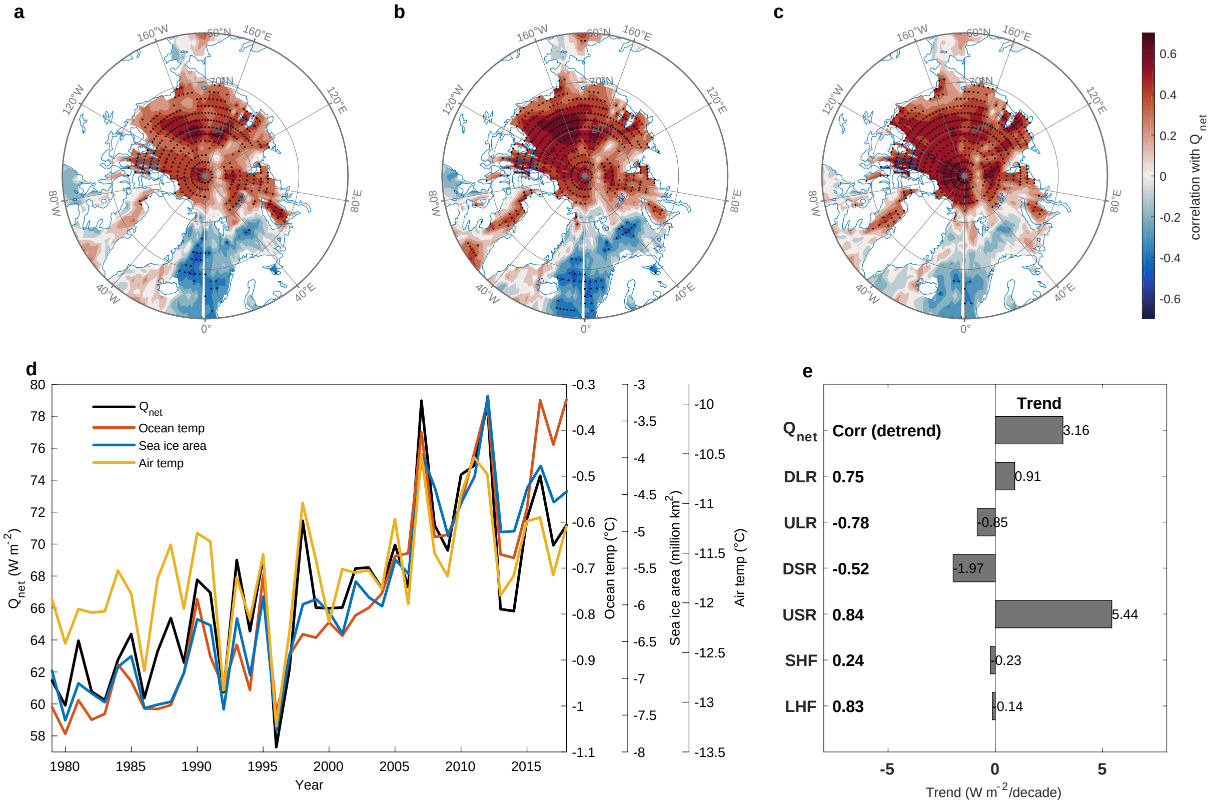

Figure I.2. Important role of radiation fluxes in linking atmosphere, sea ice and ocean. a-c Correlations of 1979 – 2018 ERA5 reanalysis JJA net heat flux (Q_{net}) field with three time series, i.e., **a** SON domain-average upper (0 – 50 m average) ocean temperature, **b** September sea ice area (SIA; average over 70° – 90°N, 0 – 360°, the sign of SIA is reversed for simplicity of comparison with plots **a&c**), and **c** JJA domain-average tropospheric (surface to 300 hPa average) air temperature. **d** Domain-average time series for JJA Q_{net} (W m^{-2}), SON upper ocean temperature (°C), September SIA (million km^2, the sign of SIA is reversed), and JJA tropospheric air temperature (°C) from 1979 – 2018. **e** Linear trends (W m^{-2} per decade) of JJA domain-averages of net heat flux (Q_{net}), downwelling longwave radiation (DLR), upwelling longwave radiation (ULR), downwelling shortwave radiation (DSR), upwelling shortwave radiation (USR), sensible heat flux (SHF), and latent heat flux (LHF) from the ERA5 reanalysis (1979 – 2018). All radiative flux variables are positive downward. Correlations of JJA domain-average net heat flux (Q_{net}) with JJA domain-averages of DLR, ULR, DSR, USR, SHF, and LHF in the ERA5 reanalysis for the period 1979 – 2018 are shown in bold next to the y-axis. All linear trends are removed in calculating the correlations in **a-c** and **e**. Black stippling in all plots indicates statistically significant correlations at the 95% confidence level.

Next, we examine the trends and correlations between domain average of JJA Q_{net} with the individual component fluxes (see Methods; Eq. 1) over the past 40 years. The increasing trend in Q_{net} is mostly due to reduced upwelling shortwave radiation (USR), and secondarily to increased fluxes in downwelling longwave radiation (DLR) at the surface (Fig. I.2e). Further, DLR and USR are two major contributors in determining Q_{net} at the surface on both interannual and interdecadal time scales (Fig. I.2d&e). As the surface albedo decreases with sea ice melt, more solar radiation is absorbed by the darker ocean (Y. Huang et al., 2021; Serreze et al., 2009; Serreze & Barry, 2011). Downwelling shortwave radiation (DSR) decreases substantially over the 40 years, but this is a secondary effect resulting from the reduction of multiple reflection between a shrinking sea ice coverage and clouds (Kapsch et al., 2016; Kashiwase et al., 2017; Wendler et al., 1981). Thus, DLR and USR serve as the key fluxes to link JJA air temperature and SON upper ocean temperature in the Arctic.

C.3 Wind nudging experiments using CESM

To provide additional evidence that changes in atmospheric circulation are driving the rise of upper ocean temperature through an adiabatic warming process, we conduct a set of nudging experiments to quantify the effect of the atmospheric circulation on upper ocean temperature in the Arctic. In this experiment we nudge winds of the Community Climate System Model 1 (Hurrell et al., 2013) (CESM1, which provides a nudging capability) to reanalysis while anthropogenic forcing is fixed at the level of year 2000 (CO_2 = 367 ppm), which is very close to the observed mean CO_2 concentration over the past 40 years (CO_2 = 369 ppm; see Methods). The goal of this experiment is to assess the contribution of wind forcing on sea ice melting and upper ocean warming by comparing the nudging experiment with the historical simulations of the same model and the observational evidence. Since the same model is used in both the historical and nudging experiment, the comparison of the two sets of experiments (CESM Large Ensemble (CESM-LEN) Project (Kay et al., 2015) vs. nudging experiments) sheds light on the respective role of winds and anthropogenic forcing in recent changes of upper ocean temperature. First, we examine the response of CESM1 to anthropogenic forcing by examining the 40-member ensemble mean of the historical simulation. The 40-member ensemble is considered sufficient to largely remove the effect of internal variability and thereby only reflects the external forcing. We examine upper tropospheric (300 hPa) winds as an indicator of the larger scale circulation. Unlike the observed upper tropospheric wind trend in ERA5, the wind trend due to anthropogenic forcing is very weak and only accounts for a small part of observed trends (Supplementary Fig. I.10). This suggests that the observed upper air wind trend in the past four decades is primarily due to internal variability of the climate system. The nudging experiment consists of five 40-yr historical runs from 1979 to 2018, in which simulated winds within the Arctic (north of 60°N) are nudged to the corresponding 6-hourly ERA5 winds (see Methods). The five members are initiated with different atmosphere, sea ice and oceanic conditions on 1979/1/1 (see Methods) and the ensemble mean of the five realizations is analyzed hereafter to remove impacts of initial conditions in the simulations. The climatology of sea ice concentration, ocean temperature, and salinity in the Arctic in the ensemble mean of these 40-yr nudging runs exhibits roughly similar patterns and magnitude as the ORAS5 reanalysis (Supplementary Fig. I.4&5; See Methods), which gives us confidence that the model has sufficient skill to simulate the mean state in the Arctic Ocean.

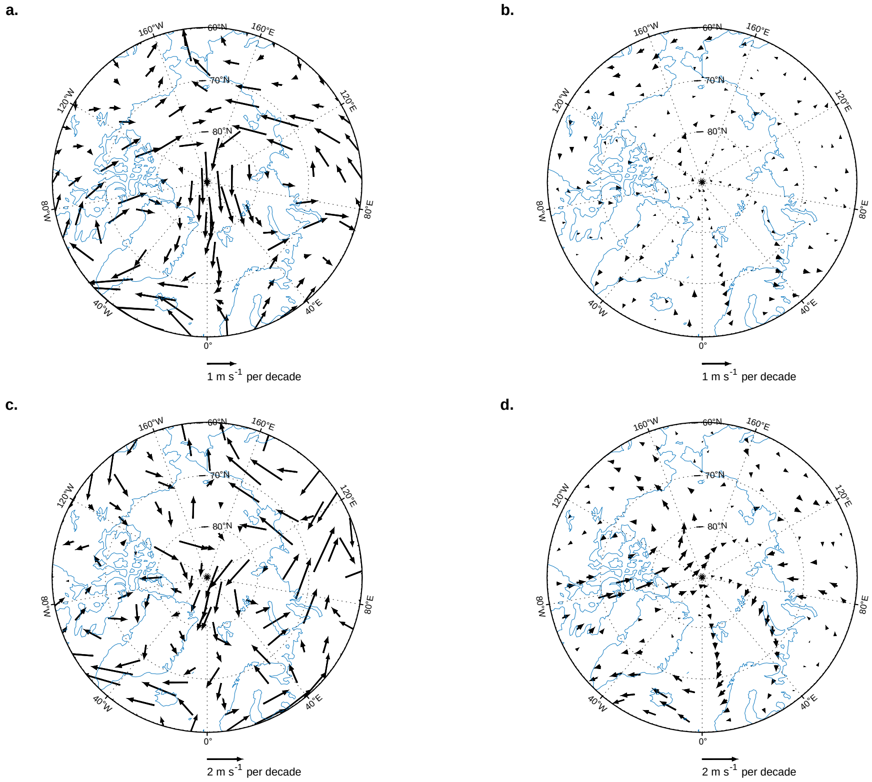

Supplementary Fig. I.10. Linear trends of JJA 300hPa wind (m s^{-1} per decade) from the ERA5 reanalysis for the period 1979 - 2018 in **a** and the period 2000 - 2018 in **c** and from the 40-member ensemble mean of CESM-LEN for the period 1979 - 2018 in **b** and the period 2000 -2018 in **d**.

The simulated spatial pattern of upper ocean temperature trend is similar to that in ORAS5 in the PPSS from 1979 to 2018 and the pattern in the PPSS and APSS for the 2000 – 2018 period although the temperature increases are slightly weaker (Fig. I.3c-f). It is particularly noted that the warming in the Barents Sea in the nudging simulations bears strong resemblance to ORAS5 for the 2000 – 2018 period (Fig. I.3e&f), with the spatial correlation coefficient between these two trend patterns (Fig. I.3e&f) within the Arctic (north of 70°N) reaching 0.77. The simulated domain average SON upper ocean temperature shows a highly correlated temporal variation with ORAS5 (for the period 1979 – 2018: r = 0.63 with trend, r = 0.67 without trend; for the period 2000 – 2018: r = 0.91 with trend, r = 0.80 without trend) on both interannual and interdecadal time scales (Fig. I.3a). This suggests that the wind-driven circulation change indeed plays an important role in upper ocean warming in the Arctic. The mean trend in the simulated upper ocean temperature in the five nudging runs is 0.04°C per decade, while that in the ensemble mean of the 40 CESM-LEN members is 0.09°C per decade. The combined upper ocean temperature trend due to the two forcings is 0.13°C per decade, which is slightly lower than the trend of 0.17°C per decade in ORAS5 over the last 40 years, suggesting that the sum of these two forcings can explain most of SON upper ocean warming. Based on their contributions to the warming in ORAS5 (0.04/0.17 and 0.09/0.17), we estimate that the internal, wind-driven variability accounts for 24% of upper ocean warming while anthropogenic forcing accounts for 53% of upper ocean warming over the past 40 years. While the wind-driven ocean warming is largely confined to the Chukchi, East Siberian, and Laptev Seas over the 40-year period, substantial warming in the Atlantic sector shows little connection with wind driven processes. This changes when we perform a similar calculation for the period 2000 – 2018, when reanalysis wind and ocean data in the Arctic are more reliable (Dee et al., 2011; Desbiolles et al., 2017), and upper ocean temperatures warmed significantly. In this case, we find that internal wind-driven variability has become even more important and over the Pan-Arctic Ocean, explaining about 60% of the Pan-Arctic Ocean warming trend from 2000 – 2018. A caveat is that anthropogenic warming likely has an imprint on the reanalysis winds which are used to drive the nudging run, although this part appears to be small (Supplementary Fig. I.10). This means that our estimates of the role of internal variability on SON upper ocean warming (24% over 1979 – 2018 and 60% over 2000 – 2018) are likely upper bounds.

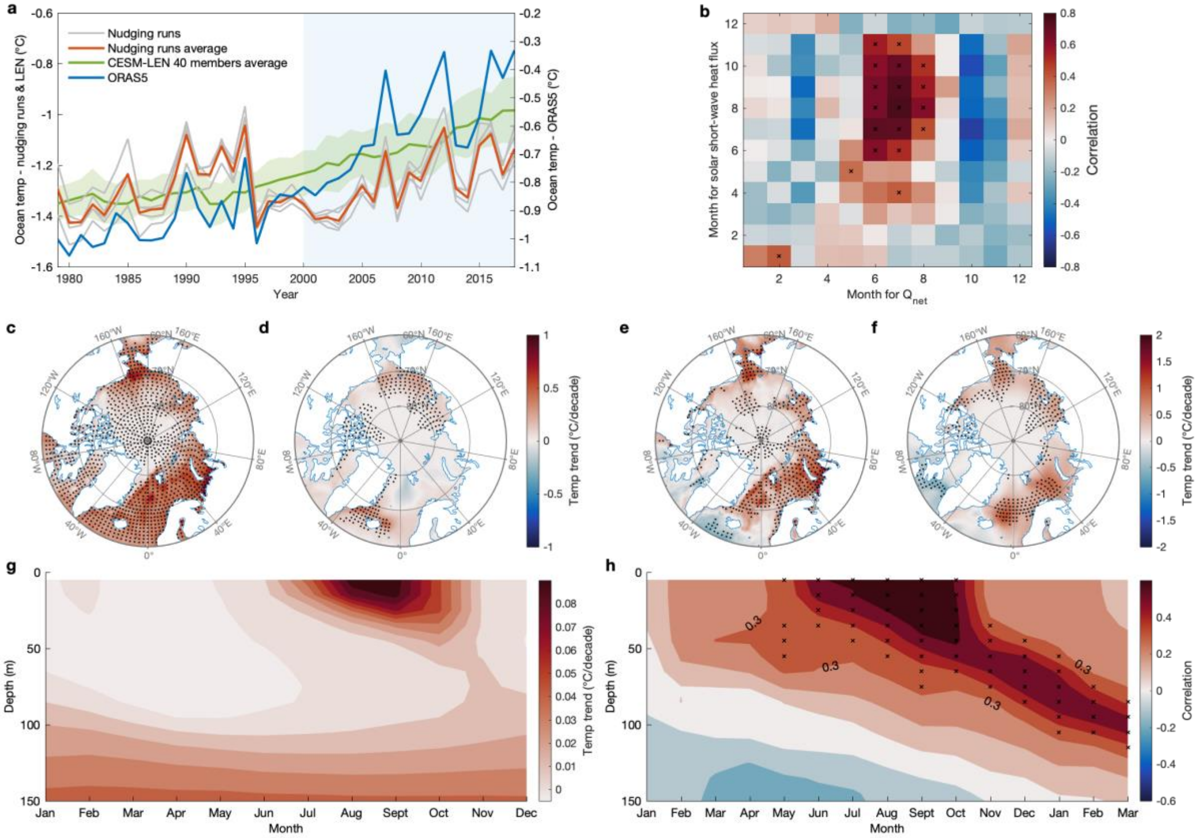

Figure I.3. Simulated impact of summertime atmospheric processes on Arctic Ocean temperature in the wind nudging experiments. a SON Arctic Ocean domain-average upper (0 – 50 m average) ocean temperature (°C) in the five wind nudging experiments (grey line) from 1979 to 2018, CESM–LEN 40 members average (green line), and ORAS5 reanalysis (blue line) from 1979 to 2018. The red line represents the ensemble average of the five wind nudging experiments. The green shading represents the one standard deviation spread of the all CESM-LEN 40 members away from the ensemble mean. **b** Correlations of monthly domain-average solar shortwave heat flux absorbed in the ocean boundary layer with monthly domain-average net heat flux (Q_{net}) at the surface for any pair of two months for the period 1979 – 2018 from the ensemble average of the five wind nudging experiments. **c-d** Linear trend (°C per decade) of upper ocean temperature from the ORAS5 reanalysis in **c**, and from the ensemble average of the five wind nudging experiments in **d** for the period 1979 – 2018. **e-f** The same as **c-d**, but for the period 2000 – 2018. **g** Monthly cross-section of the linear trend (°C per decade) of domain-average ocean temperature over 0 – 150 m depth for the period 1979 – 2018 from the ensemble average of the five wind nudging experiments. **h** Correlation of JJA domain-average tropospheric air temperature with domain-average ocean temperature, for each month (the last three months: Jan-Feb-Mar are the months in the next year) and depth (from 0 – 150 m) for the period 1979 – 2018 from the ensemble average of the five wind nudging experiments. All linear trends are removed in calculating the correlations in **b&h**. Black stippling in all plots indicates statistically significant correlations or trends at the 95% confidence level.

In order to check that the model is accurately simulating ocean conditions, we next compare the simulated upper ocean temperature trend in the nudging experiments (see Fig.

I.3g) with that in ORAS5. Comparison with Fig. I.1f indicates that the model is capturing the main warming, although its magnitude is only 25% of values in ORAS5. The lagged correlation between simulated domain average JJA tropospheric air temperature and domain average ocean temperature also yields a similar pattern as the counterpart in ORAS5 in Fig. I.1h, i.e., significant JJA atmospheric warming precedes the ocean temperature rise that shows a strong downward intrusion into lower layers from June through the following winter (Fig. I.3h).

Consistent with observations in ERA5, DLR and USR in both the nudging and historical runs are the two main factors contributing to the positive Q_{net} trend over the past 40 years (Supplementary Fig. I.11a). In the nudging runs, wind-driven impacts on DLR and USR are comparable with that due to CO_2 forcing, suggesting that large-scale circulation variability plays a similar role as CO_2 forcing in triggering the sea ice-albedo effect seen as an increase of USR in Supplementary Fig. I.11a. Nudging CESM1 to observed winds yields simulated DLR and USR averages capturing over 50% of the observed variability in those energy balance components, with r = 0.72 and 0.74 for DLR and USR respectively (Supplementary Fig. I.11b).

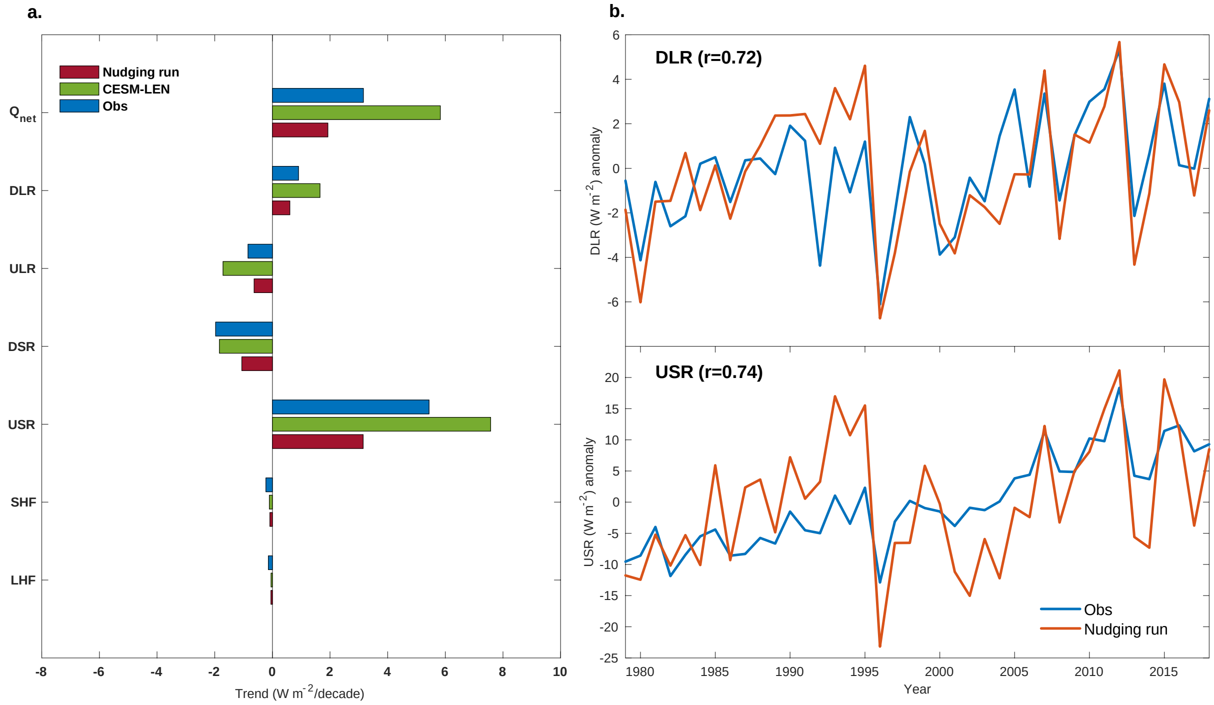

Supplementary Fig. I.11. **a** Linear trends (W m^{-2} per decade) of JJA Arctic domain-averages of net heat flux (Q$_{net}$), DLR, ULR, DSR, USR, SHF, and LHF in the ensemble average of the five wind nudging experiments (red bars), the ensemble average of CESM-LEN 40 members (green bars), and the ERA5 reanalysis (blue bars) (1979 - 2018), and all radiative flux variables are positive downward. **b** JJA Arctic domain-average DLR and USR anomalies (unit: W m^{-2}) in the ensemble average of the five wind nudging experiments (red line) and the ERA5 reanalysis (blue line).

To better understand mechanisms contributing to upper oceanic warming and its deepening in our nudging runs, we examine the trends of SON mixed layer depth (MLD) in the Arctic Ocean. The deepening of MLD is observed in both ORAS5 and the nudging runs since 1979, especially for the period from 2000 to 2018 (Supplementary Fig. I.12), indicating that the wind-driven vertical mixing can partially explain enhanced downward heat transport in the upper ocean through increasing the MLD. Although the vertical mixing is overestimated in the simulations compared with that in ORAS5 (Supplementary Fig. I.12a&d; Fig. I.3h), it remains unclear which one is closer to observations since most climate models and reanalyses contain large uncertainties to capture the MLD and its variability in the Arctic (Ilıcak et al., 2016). Furthermore, to trace how changes in Q$_{net}$ propagate into the upper ocean where they can contribute to warming, we examine the relationship of Q_{net} with the solar shortwave radiation heat flux penetrating into the ocean boundary layer (Q_{short_bl}; see Methods) for our nudging runs. This layer on average is ~ the upper 30 m of the ocean in the nudging runs. An increase in SON Q_{short_bl} from 1979 – 2018 is primarily confined to the PPSS (Supplementary Fig. I.13a) (Perovich et al., 2007). High correlations between JJA domain average Q_{net} and Q_{short_bl} field in JJA exist over the peripheral seas (the Beaufort, Chukchi, East Siberian, Laptev, and Kara Seas) but shift to the entire Arctic Ocean for SON (Supplementary Fig. I.13b&c). Fig. I.3b more clearly reveals the temporal relationship of Q_{net} and Q_{short_bl}, showing that Q_{net} in JJA is highly correlated with simultaneous and subsequent Q_{short_bl} until November, with highest correlations when Q_{net} leads Q_{short_bl} by one month. The spatial and temporal lead-lag relationship of Q_{net} and Q_{short_bl} is what is expected if changes in Q_{net} first drive sea ice loss and subsequent upper ocean warming. This provides the physical mechanism that ties large-scale wind variability and its effect on Q_{net} to upper ocean warming via the ice-albedo effect and the deepening of the MLD.

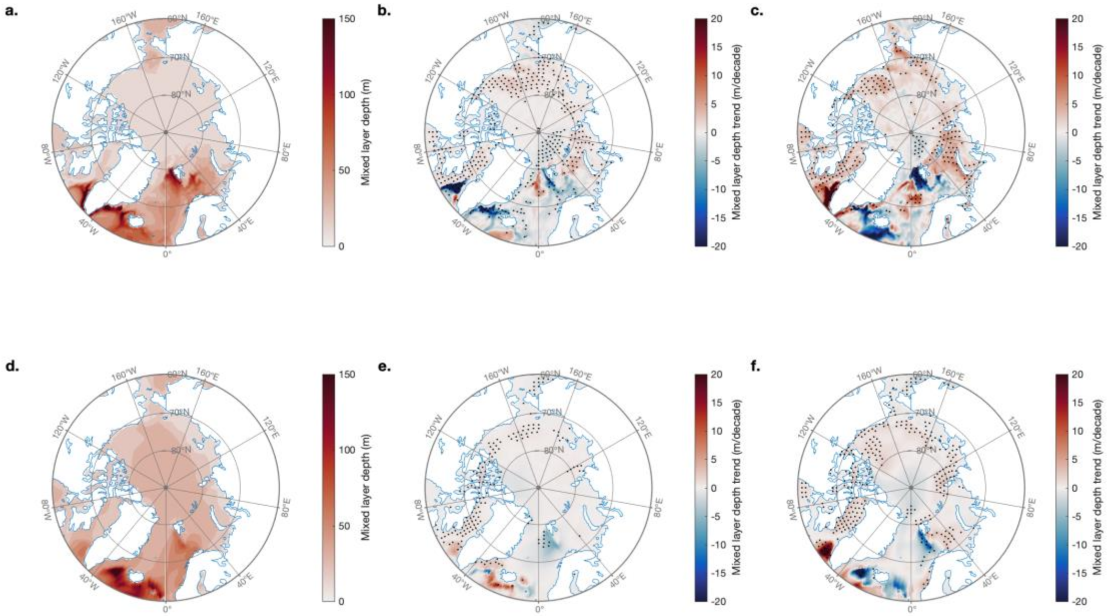

Supplementary Fig. I.12. **a** Climatology (m) of the mixed layer depth in SON from the ORAS5 reanalysis for the period 1979 – 2018. **b-c** Linear trend (m per decade) of the mixed layer depth in SON for the period 1979 – 2018 in **b**, and for the period 2000 – 2018 in **c** from the ORAS5 reanalysis. **d-f** Same as **a-c**, but from the ensemble average of the five wind nudging experiments. Black stippling in all plots indicates statistically significant trends at the 95% confidence level.

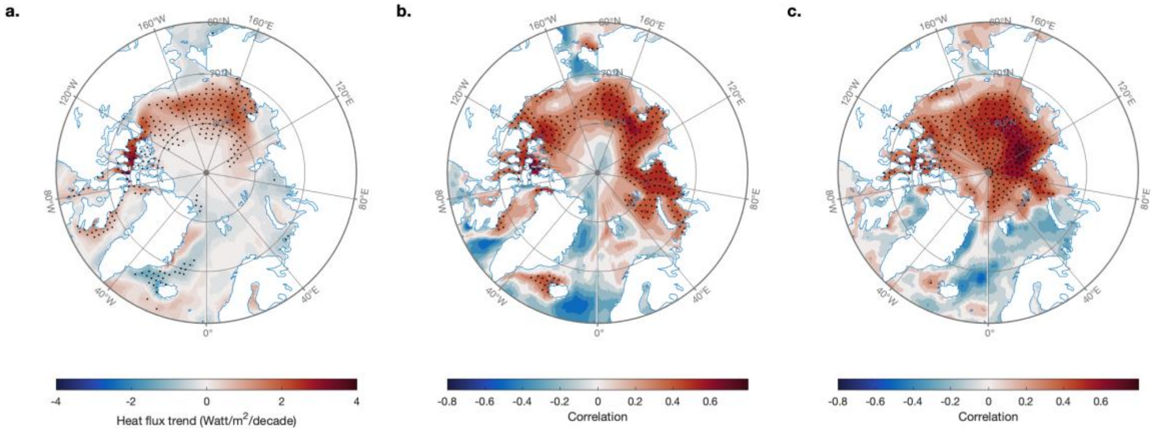

Supplementary Fig. I.13. **a** Linear trend (W m^{-2} per decade) of solar shortwave heat flux in the ocean boundary layer (Q_{short_bl}) field in SON from the ensemble average of the five wind nudging experiments for the period 1979 – 2018. **b-c** Correlation of JJA domain-average net heat flux (Q_{net}) with Q_{short_bl} field in JJA in **b**, and in SON in **c** from the ensemble average of the five wind nudging experiments for the period 1979 – 2018. Black stippling in all plots indicates statistically significant correlations or trends at the 95% confidence level.

C.4 Poleward ocean heat transport contribution

Although the nudging runs well-replicate the upper ocean temperature rise in the Arctic, especially over the PPSS, model vs. reanalysis (ORAS5) differences remain (e.g., Fig. I.3c&d). This indicates that some additional factors not directly captured by atmospheric wind forcing may play a role in driving changes in the Arctic, especially over the APSS. Poleward ocean heat transport (POHT) is in part driven by winds but are also affected by large scale ocean dynamics that are not directly tied to winds (or at least not at the time scales considered here). We consider POHT in the upper 50 m through two separate gates into the Arctic Ocean, a Pacific Gate measuring heat inflow through the Bering Strait and an Atlantic Gate measuring net heat inflow from the Nordic Seas (Fig. I.4a). In this section, we explore the role of POHT on upper ocean warming, although we do not provide a quantitative “variance explained” analysis as in previous sections. This is because an exercise that would involve ocean state nudging is beyond the scope of this study.

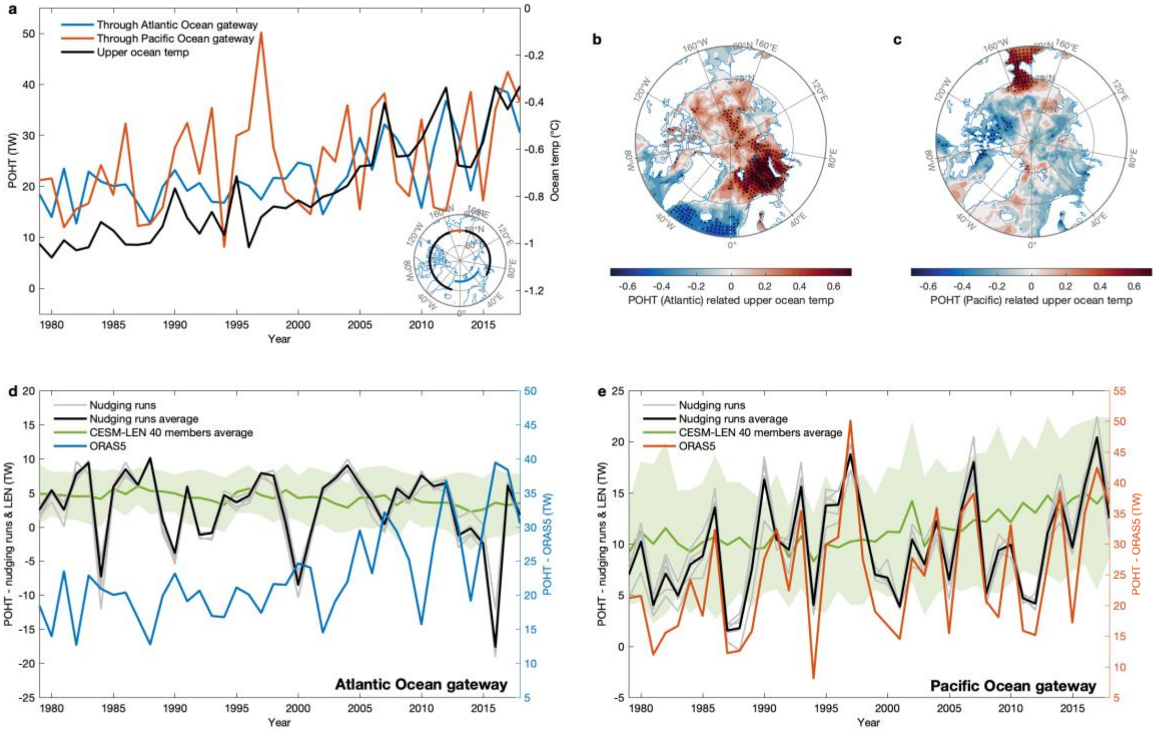

Figure I.4. Poleward ocean heat transport through the Atlantic & Pacific Ocean gateways in fall. a SON poleward ocean heat transport (POHT; unit: TW, 1TW = 10^{12} W) within upper 50 m through the Atlantic Ocean gateway (blue line) and Pacific Ocean gateway (red line), and SON domain-average upper (0 – 50 m average) ocean temperature (°C, black line) using the ORAS5 reanalysis for the period 1979 – 2018. The Atlantic and Pacific Ocean gateways are indicated by the blue and red contours in the stereographic projection (lower right in **a**). **b-c** Correlations of 1979-2018 SON upper ocean temperature field with two time series, i.e., **b** SON upper 50 m POHT through the Atlantic Ocean gateway in **a** (blue line), **c** SON upper 50 m POHT through the Pacific Ocean gateway in **a** (red line)**. d&e** SON upper 50 m POHT (TW) from 1979 to 2018 through the Atlantic Ocean gateway in **d,** and through the Pacific Ocean gateway in **e** from the five wind nudging experiments (grey lines, and ensemble average in black line), CESM-LEN 40 members average (green line), and the ORAS5 reanalysis (blue line for the Atlantic Ocean gateway, red line for the Pacific Ocean gateway). The green shading represents the one standard deviation spread of the all CESM-LEN 40 members away from the ensemble mean. All linear trends are removed in calculating the correlations in **b&c**. Black stippling in all plots indicates statistically significant correlations at the 95% confidence level. POHT through the Atlantic Ocean and Pacific Ocean gateways are calculated using different reference temperatures (0℃ for the Pacific Ocean gateway and -1.9℃ for the Atlantic Ocean gateway, respectively).

SON upper 50 m POHT through the Atlantic Gate derived from ORAS5 shows an upward trend since 2000 (Fig. I.4a), especially via the branch of that through the Barents Sea (Supplementary Fig. I.14b), and is strongly correlated with SON upper ocean temperature on both interannual and interdecadal time scales for the period 1979 – 2018 (r = 0.80 with trend;

r = 0.58 without trend). Correlating the POHT time series with upper ocean temperature field shows that the variability of POHT through the Atlantic Gate in SON strongly affects the Barents and Kara Seas (Fig. I.4b). The cause of the high correlations in the parts of the central Arctic Ocean is puzzling. One possible reason is that an air-sea heat flux exchange is able to quickly take the warm signal from the Barents and Kara Seas to the central Arctic Ocean via the atmosphere (J. Zhang et al., 1998). This simultaneous connection may also result from some influences in preceding seasons that can regulate upper ocean temperature in both the central Arctic Ocean and the Barents and Kara Seas. In contrast, POHT through the Pacific Gate has an increasing trend as well (Fig. I.4a) but only affects the Chukchi Sea (Fig. I.4c).

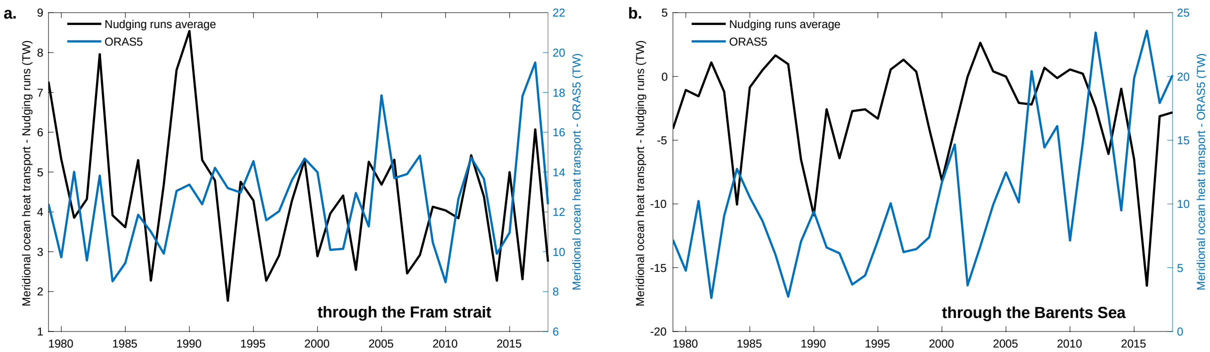

Supplementary Fig. I.14. SON POHT (TW) within upper 50 m from 1979 to 2018 through the Fram Strait in **a,** and through the Barents Sea in **b** from the ensemble average of the five wind nudging experiments (black line) and the ORAS5 reanalysis (blue line).

The variability of simulated SON upper 50 m POHT through the Pacific Gate in the wind nudging runs very successfully capture the counterpart in ORAS5 (Fig. I.4e; r = 0.9 with trends, r = 0.89 without trends), but this is not the case for the Atlantic Gate (Fig. I.4d & Supplementary Fig. I.14). This suggests that winds play an important role in driving POHT through the Bering Strait (Danielson et al., 2014; W. Zhang et al., 2020). Nevertheless, wind-driven POHT through the Bering Strait only has a weak correlation with upper ocean temperature in the interior of the basin and appears to have little impact on Pan-Arctic Ocean warming. We also compare SON upper 50 m POHT via the Atlantic Gate in the nudging runs with that in the 40-member ensemble means of the historical simulation in CESM (Fig. I.4d&e). None of these capture the increasing trend of POHT through the Atlantic Gate as seen in ORAS5, suggesting that SON upper 50 m POHT changes through the Atlantic Gate are likely determined by more complex factors that are not directly driven by winds and anthropogenic forcing in our model, such as the initial ocean condition, deeper layer oceanic variability, internal oceanic thermohaline variability in the Arctic and heat transport from the lower latitudes where observed winds are not specified (Årthun et al., 2019; Muilwijk et al., 2019; Wang, Wang, et al., 2019; Wang, Wekerle, et al., 2019). The role of anthropogenic forcing in contributing to increasing POHT via the Atlantic sector remains an open question since this attribution appears to be sensitive to approaches used to detect this feature (Årthun et al., 2019; Muilwijk et al., 2018). Importantly, the fact that our nudging simulations did not capture an upward trend in POHT through the Atlantic Gate further supports our main finding: namely, the role of our identified mechanism in expediting Arctic Ocean warming via summertime atmospheric processes.

D. Discussion

Our study suggests that a portion of upper Arctic Ocean warming over the past few decades can be explained by low-frequency atmospheric variability characterized by a trend toward anomalous anticyclonic circulation over the Arctic Ocean and Greenland. This process produces subsidence and adiabatic warming which acts to warm the atmosphere, melt sea ice, and deepen the ocean mixed layer. The resulting open water warms via shortwave radiation absorption and enhanced vertical mixing. Our nudging experiments confirm that adiabatic dynamical forcing associated with winds in the Arctic is able to explain up to 24% of SON upper ocean warming from 1979 to 2018 and up to ~ 60% of upper ocean warming for the period 2000 to 2018, which is mostly confined to the Chukchi, East Siberian, and Laptev Seas before.

We have previously suggested that internal atmospheric forcing is in part forced by sea surface temperature variability in the tropics via a Rossby wave train (Baxter et al., 2019). The capability to replicate both local air-ice-ocean coupling as well as an accurate tropical – Arctic Ocean connection is thus a key model skill. However, simple evaluations conducted in previous studies indicate that some models have trouble replicating both the full strength of the local coupling on interannual time scales and also tropical – Arctic Ocean connections (Bonan & Blanchard-Wrigglesworth, 2020; England et al., 2020). An efficient and well-developed metric, emphasizing a lead-lag connection between JJA atmospheric temperature with SON ocean temperature as we show in Fig. I.1f&g, is thus needed to better evaluate the performance of models in representing this Arctic atmosphere-sea ice-ocean coupling and its possible linkage with remote forcing.

In this study, we primarily focus on the surface layer of the Arctic Ocean and local ocean – air coupling through thermodynamical processes. However, the surface heat balance is also influenced by ocean mixing, the deep ocean circulation and heat transport from sub-Arctic Oceans (Carmack et al., 2015; Oldenburg et al., 2018; I. V. Polyakov, Rippeth, et al., 2020; Tsubouchi et al., 2021). In particular, the barotropic feature of the POHT through the Atlantic Gate (see Methods) requires an integrated view of heat transport throughout the whole depth. Other factors, such as water mass exchanges between the Arctic and Atlantic/Pacific Oceans (Steele et al., 2010), and freshwater storage changes (Jahn & Laiho, 2020) become more important when we shift our focus to ocean lateral heat flux convergence and the deeper layers of the Arctic Ocean. Moreover, the ocean mixing is not only sensitive to surface winds (Sallée et al., 2021) and Ekman convergence and pumping in the surface layer around the central Beaufort Gyre (Steele et al., 2011), but also regulated by brine rejection (Lind et al., 2018). Recently, the "Atlantification" process has been suggested to be associated with weakened stratification and increased vertical mixing, which enhances upward heat fluxes to the surface (I. V. Polyakov et al., 2017; I. V. Polyakov, Rippeth, et al., 2020). This process may influence upper ocean warming and sea ice melt and may not be well-replicated in our simulations. Further studies are needed to better understand the relationship and interaction between the Arctic Ocean and the internal large-scale atmospheric process described here.

II. Atmosphere-Driven Processes in Shaping Long-Term Climate Variability in Greenland and the Broader Subpolar North Atlantic

Abstract

The subpolar North Atlantic (SNA) represents a key region for atmospheric and oceanic heat exchange between the Arctic and subarctic, as well as for the maintenance of the Atlantic Meridional Overturning Circulation. Observational datasets reveal signatures of low-frequency climate variability in the SNA over the past decades: a warming trend in sea surface temperatures and a rise in atmospheric pressure in the troposphere have been observed from the early 1990s to the early 2000s, followed by an apparent pause or even a reversal in these climatic trends. The detailed mechanisms of this multidecadal climate variability remain elusive due to complex interactions between the atmosphere, ocean, and ice, as well as remote forcing of atmospheric teleconnections in and around the region. In particular, CMIP6 climate models, forced by anthropogenic forcing, show diverse skill in simulating this decadal variability, indicating a possible role of internal atmosphere-ocean interactions in regulating the regional impact of anthropogenic forcing over the SNA. Here, we investigate the physical mechanisms underlying these processes by analyzing various model simulations and conducting a new model experiment forced by observed local SNA winds. Results reveal that regional atmospheric circulation, partially driven by remote forcing from the tropical Pacific, dominates the recent multidecadal climate variability in the SNA by modulating local atmosphere-ocean interactions and upper-ocean poleward heat transport around 45°N. This finding highlights the importance of large-scale atmospheric circulation in driving

multidecadal climate variability over Greenland and the larger SNA region in the historical era.

A. Introduction

Anthropogenic greenhouse gas emissions have been consistently identified as the main cause of global surface warming over the land and ocean in the past century based on both observational and modeling evidence (Delworth & Knutson, 2000; Hegerl et al., 1997; Jones et al., 1999; Santer et al., 1996; Tett et al., 1999). Despite this widespread warming trend observed across global oceans in response to the steady increase in atmospheric CO_2 concentrations, sea surface temperature (SST) in the subpolar North Atlantic (SNA) has shown a warming hiatus in the past century (also known as the “warming hole”) (Drijfhout et al., 2012; Hansen et al., 2010; Rahmstorf et al., 2015). Meanwhile, past studies have reported an ongoing slow-down in the Atlantic Meridional Overturning Circulation (AMOC) (Smeed et al., 2018; Boers, 2021), yet observational evidence for long-term AMOC changes is still limited (Wett et al., 2023). Whether the counterintuitive SST cooling in the SNA and concurrent AMOC changes since the early 2000s are of anthropogenic origin (Chemke et al., 2020), a manifestation of internal climate variability, or a combination of both factors remains unclear. It is widely recognized that anthropogenic forcing and internal variability together have shaped the observed climatic variability over the northern high latitudes in the past four decades (Ding et al., 2019; England et al., 2021; Hanna et al., 2018; Z. Li et al., 2022). Yet, a comprehensive understanding of how these processes interact and jointly shape regional climate variability, along with a quantification of their relative roles, is still lacking.

The main cause of the observed recent SNA ocean cooling remains a topic of ongoing debate. Some studies suggest that the anthropogenically forced AMOC slow-down and the resultant weaker ocean heat transport convergence into the North Atlantic can explain the SNA warming hole (Caesar et al., 2018; Chemke et al., 2020b; Drijfhout et al., 2012; Gervais et al., 2018; Liu et al., 2020; Menary & Wood, 2018; Rahmstorf et al., 2015). However, available instrumental measurements of AMOC are not long enough to provide clear evidence of this mechanism (Wett et al., 2023). Alternative suggestions to explain the warming hole pattern include enhanced ocean heat transport out of the North Atlantic into the Arctic Ocean (Keil et al., 2020), import of cold near-surface water masses from the Labrador Sea (Keil et al., 2020), intensified vertical mixing processes (Latif et al., 2022), and reduced net surface solar radiation caused by anthropogenic aerosols (Booth et al., 2012). Recently, observational and modeling studies have proposed that the SNA cooling could be primarily controlled by both local and remote atmospheric processes, such as changes of local surface winds induced by local weather processes or atmospheric teleconnections due to Indian Ocean warming (Josey et al., 2019; Hu & Fedorov, 2020; Keil et al., 2020; He et al., 2022; L. Li et al., 2022). However, the detailed mechanisms behind these atmospheric processes require further investigation.

As key components of the region’s climate system, the surface air temperature and ice sheet mass balance over Greenland, and sea ice surrounding Greenland have also exhibited changes in recent decades (Ballinger et al., 2018; Hanna et al., 2021; Trusel et al., 2018). The melting of the Greenland Ice Sheet (GrIS), primarily mediated by marine-terminating glaciers, leads to increased freshwater discharge into the surrounding oceans, significantly influencing North Atlantic weather patterns (Oltmanns et al., 2020). Most studies highlight the dominant role of subsurface warming in Baffin Bay and the Labrador Sea (Rignot et al., 2012), as well as the intrusion of Atlantic waters (Holland et al., 2008), in driving ice mass loss at the front of glaciers, particularly between the late 1990s and 2007 (Wood et al., 2021). Large-scale atmospheric circulation as a possible driver of ocean warming and thus glacier mass balance changes of the GrIS has also been suggested (Topál et al., 2022). Sea ice in the region also displays complex changes in recent years, characterized by a decrease in extent and thickness, and a delay in ice cover formation (Ballinger et al., 2018; Germe et al., 2011; Nakamura et al., 2015; J. C. Stroeve et al., 2014, 2017). Previous studies suggest that these changes over the past decades are due to local climate conditions (Ballinger et al., 2018; Hanna et al., 2016; McLeod & Mote, 2016) and oceanic heat transport, including warming of Atlantic-origin water in the West Greenland Current (Ballinger et al., 2022; Myers et al., 2009). Hence, a comprehensive understanding of the air-sea ice-ocean interaction in the SNA is needed to explore the underlying mechanisms of climate variability in the region and beyond.

Climate models' historical simulations consistently depict a uniform SST warming globally, but the recent multidecadal SST variability in the North Atlantic is not fully reproduced in our best estimate of the climate response to historical anthropogenic forcing derived from the latest generation of climate models comprising the Coupled Model Intercomparison Phase 6 (CMIP6). This discrepancy is demonstrated by diverse behavior in the response. Given the limitations of current models in replicating the recent observed changes in the SNA, there is a critical need within the climate research community to better understand the driving mechanisms associated with the observed multidecadal atmosphere-ocean coupled variability in the region. To address this need, this study will analyze the available experiments archived in CMIP6 and large ensemble simulations, and additionally conduct a novel experiment by imposing observed North Atlantic winds into a fully-coupled model, specifically the Community Earth System Model 1 (CESM1). Through analyzing the experiment, we aim to better understand the role of atmospheric circulation changes in driving climate variability in the SNA. This approach will also enable us to evaluate the relative roles of atmospheric and oceanic processes in regulating observed low-frequency climate variability in the North Atlantic and gain new insights into possible model biases.

B. Methods

B.1 Reanalysis and observation data

In this study, we use the Ocean Reanalysis System 5 (ORAS5) (Zuo et al., 2019) and the Extended Reconstructed Sea Surface Temperature v5 (ERSSTv5) (B. Huang et al., 2017), developed by the National Oceanic and Atmospheric Administration (NOAA), as well as the Hadley Centre SST dataset (HadSST4) (Kennedy et al., 2019) to investigate the variability of SNA SST and its relationship with atmospheric variables in the SNA over the past decades. ORAS5 is widely used and regarded as a reliable reanalysis product for the high northern latitudes oceans (Carton et al., 2019; Z. Li et al., 2022). SST variability in ORAS5 closely matches ERSSTv5 and HadSST4 in most grids of the tropical and extratropical Northern Hemisphere (NH). Therefore, we have confidence in the reliability of ORAS5 as a data source for conducting SST-related calculations in this study. For atmospheric variables, 1979-2020 monthly wind, air temperature, and shortwave and longwave radiation fields from the ERA5 reanalysis (Hersbach, Bell, Berrisford, Hirahara, Horányi, Muñoz-Sabater, et al., 2020) are utilized to understand atmospheric processes over the past four decades. Monthly sea ice extent is obtained from the National Snow and Ice Data Center (NSIDC) Climate Data Record of Passive Microwave sea ice concentration version-3 (Fetterer et al., 2017).

B.2 Modéle Atmosphérique Régional (MAR)

Monthly mean surface mass balance (SMB) output from the Modele Atmospheric Regional (MAR) simulations is used to characterize GrIS SMB. MAR is a regional climate model (Lang et al., 2015) specifically designed and physically optimized for the polar regions, including the GrIS (Amory et al., 2015), which combines atmospheric modelling (Gallée & Schayes, 1994) with the Soil Ice Snow Vegetation Atmosphere Transfer Scheme (Fettweis et al., 2017) and has been widely used to simulate GrIS surface energy balance and mass balance processes (Fettweis, 2007; Fettweis et al., 2011; Franco et al., 2012; Lang et al., 2015; Topál et al., 2022). In this study, we use the MAR model version 3.11 output, which is forced at its lateral boundaries by 1x1 km^2 spatial resolution ERA5 reanalysis data (e.g., air temperature, specific humidity, wind speed, pressure, SST, and sea ice concentration) at monthly timesteps from 1979 to 2020. In this study, a so-called south GrIS SMB index is calculated as the weighted average of SMB values in the southern GrIS (< 70°N) since this region is more sensitive to SST and ocean circulation changes in the SNA due to its proximity to the area.

B.3 CMIP6 and CESM1 Large Ensemble

We analyze 28 models that participate in CMIP6 (Eyring et al., 2016) (historical + SSP585 scenarios) spanning from 1979 to 2020 to examine ocean temperature variability in the SNA and its coupling with the atmosphere in the models. Only one member (r1i1p1f1) from each model is used.

We also use the Community Earth System Model 40-member Large Ensemble (CESM-LE) (Kay et al., 2015) to consider both internal climate variability and the forced response to anthropogenic forcing within the same model system. The CESM-LE was conducted using the CESM1 (Hurrell et al., 2013) with 40 simulations integrating from 1920 to 2100. All members are forced by CMIP5 historical forcing from 1920 to 2005, and by the Representative Concentration Pathway 8.5 forcing (RCP8.5) from 2006 to 2100 with slight perturbations in the initial atmospheric conditions for each member. Since averaging of all members largely minimizes the internal variability of the model system, it is used here to represent the forced response of the climate system. We also use the CESM1 1800-year pre-industrial control run to alternatively assess internal variability over the SNA in the absence of anthropogenic forcing.

B.4 CAM6 Prescribed SST AMIP Ensemble

To assess the influence of the SST changes in shaping high latitude climate variability, we use the simulations from 10-member Community Atmosphere Model version 6 (CAM6) Prescribed SST Atmospheric Model Intercomparison Project (AMIP) Ensemble (Danabasoglu et al., 2020). CAM6 is the atmospheric model of CESM2, and it was integrated on a nominal 1° grid. In the simulations, prescribed global SST (from ERSSTv5) and sea-ice (from HadISST1) are specified from 1880 to 2021, and all members are initialized from the 11th CESM2 member on January 1st, 1880, with a small change in the initial air temperature field, termed as Global Ocean Global Atmosphere (GOGA hereafter). In the simulations, SSTs are prescribed from the observational data rather than being allowed to interact with the atmosphere as in a coupled atmosphere-ocean model, and all CMIP6 time-varying natural and anthropogenic forcings are specified in these ensembles. The ensemble means of these 10 members are used to explore how observed SST/sea ice boundary forcing along with anthropogenic forcing drives large-scale circulation changes in the NH middle and high latitudes. We also examine similar GOGA simulations using CESM1. The result is not sensitive to our selection, and additionally, the CESM1-GOGA simulations only provide results until 2015, so we mainly focus our discussion on CESM2-simulated GOGA in the following sections.

B.5 Definition of the AMOC index

In this study, we define the AMOC index as the difference between the domain averaged annual-mean SSTs of the subpolar gyre region (sg) and the whole globe (Caesar et al., 2018):

$$I_{AMOC} = SST_{sg} - SST_{global} \tag{1}$$

The sg region is deemed particularly sensitive to a reduction in the AMOC, and thus serves as an essential SST region of reference (Caesar et al., 2018). The sg region covers most of the area in which the AMOC transports heat northwards and releases it to the atmosphere; here, the geographical area is determined by the method of Caesar et al., (2018). The comparison of various SST-based AMOC indices, utilizing different regions, data, and methods (Caesar et al., 2018; Ditlevsen & Ditlevsen, 2023; Rahmstorf et al., 2015), reveals a consistency in their variations on a multidecadal timescale over the past decades. This underscores the viability of creating the AMOC index using SST.

It is important to note that there are alternative methods for measuring AMOC variability. For instance, some studies use altimetry measurements (Willis, 2010), subpolar upper-ocean salinity (X. Chen & Tung, 2018), paleoclimate proxies (R. Zhang, 2017) or accumulated sea-level (McCarthy et al., 2015). These various approaches offer different perspectives on the stability of the AMOC, usually revealing consistent trends over recent decades, thus highlighting the robustness of AMOC calculations for modern-day climate studies. While different definitions of the AMOC index can lead to differences in interannual variations, our primary focus is on the surface ocean and its interaction with the atmosphere in the region. In light of this emphasis, using an SST-based AMOC index is appropriate for our study.

B.6 Poleward ocean heat transport (POHT)

To examine the role of ocean heat transport in the atmosphere-ocean coupling in the SNA, POHT is calculated as the cross-section integral of ocean potential temperature multiplied by meridional ocean velocity, seawater density, and the specific heat capacity for a given depth layer (in W):

$$POHT = C_p \cdot \rho \int_D^0 \int_{west}^{east} V(\theta - \theta_r) dz \cdot dx \tag{2}$$

In this study, we consider the ocean depth, D, of 50 m. V represents the meridional component of ocean velocity, while $\theta - \theta_r$ is the difference between temperature and a reference temperature (θ_r = 0 $°C$ for the North Atlantic region). The specific heat capacity of seawater, C_p, is 4200 $J\ Kg^{-1}C^{-1}$. We assume the density of seawater, ρ, as a constant 1027 $kg\ m^{-3}$ for the SNA Ocean, given that there is minimal fluctuation in actual density values. Calculations are based on a cross-section situated in the middle part of the SNA Ocean's southern boundary (40°W-20°W longitude at 45°N latitude). This cross-section includes the primary pathway favoring northward transport into the SNA Ocean we defined.

B.7 Wind-nudging experiments using CESM1

In this study, we use the fully-coupled model - CESM1 (Hurrell et al., 2013) to conduct a nudging experiment to investigate the contribution of observed wind forcing and atmospheric circulation changes to SNA SST variability. In the experiment, North Atlantic (30°N -90°N, 100°W-40°E) atmospheric winds from the surface to top-of-atmosphere are nudged to the corresponding 6-hourly ERA5 winds to constrain the North Atlantic circulation in the model while keeping all external forcing, e.g., anthropogenic forcing, constant at the level of the year 2000. By doing this, we could replicate the observed North Atlantic atmospheric circulation variability in the model and assess the ocean's response to the observed wind alterations. Since winds are constrained to ERA5 in this run over the North Atlantic, we only need one realization of the simulation to understand its local variability since member-to-member variations originating from atmospheric variability over the North Atlantic are minimized.

B.8 Paleo-reanalysis

To further study circulation-driven climate variability observed in the SNA over centennial time scales, we utilize the Ensemble Kalman Fitting 400 version 2 (EKF400v2; Valler et al., 2022) - a paleoclimatic data-assimilated climate model experiment. EKF400v2 is an atmospheric-only general circulation model simulation, leveraging an expansive observational network that incorporates early instrumental temperature and pressure measurements, documentary sources, and tree-ring dimensions (both width and density) as proxy indicators. For our analysis, we apply Maximum Covariance Analysis (MCA; described in Section 2.9) to the EKF400v2 (geopotential height at 500hPa (Z500)) and ERSSTv5 (SST) from 1854 to 2003. This period is chosen due to the availability of global SST data (SST records beginning in 1854; paleo data extending up to 2003) and the increased reliability of paleo-reanalysis post-1850s as proxy data becomes more abundant.

B.9 Statistical analysis and significance

In this study, we extensively utilize MCA (Bretherton et al., 1992) to examine the dominant co-variation patterns between large-scale atmospheric circulation (e.g., geopotential height at 200hPa (Z200)) and SST in the SNA region, using reanalyses and models' results. MCA uses a singular value decomposition on the temporal covariance matrix of two fields, identifying the most coherent pairs of spatial patterns and determining a linear relationship between two different fields that are most closely coupled. Such insights aid in understanding the mechanisms and processes that drive the interplay between large-scale atmospheric circulation and SST in the SNA. For CESM-LE MCA analysis, we conduct MCA for each member and then average all MCA1 results together to compare with observational and other models' results.

To examine the significance of correlations, we use the effective sample size (N*) as computed in the equation below:

$$N^{*} = N\frac{1-r_1 r_2}{1+r_1 r_2} \qquad (3)$$

Here, N represents the total available time steps, while r_1 and r_2 denote the lag-one autocorrelation coefficients of each variable over the studied period. A confidence level of 95% is used to determine the significance of correlations in this study based on N*.

C. Results

C.1. Subpolar North Atlantic SST changes in observations and climate models

C.1.1 Trends over the period 1979-2020

Annual mean SSTs, derived from various datasets, exhibit similar interannual and decadal variabilities over the subpolar North Atlantic Ocean (red contour in Fig. II.1b, as the region within 45°N-80°N in latitude and 70°W-0° in longitude) during the past four decades (1979-2020) (Fig. II.1a). For the entire period, all datasets show a long-term, basin-wide warming trend surrounding the SNA warming hole to the south of Greenland (Fig. II.1b-d). Among these datasets, ORAS5 shows the strongest warming hole feature in the region, with a cooling rate of up to around -0.3 °C per decade in its center (around 50°N, 38°W) and a warming rate of 0.15-0.3 °C per decade in the surrounding areas. However, this warming hole signal is not due to continuous SST cooling throughout the period, but rather a very recent cooling (-0.53 °C per decade) started around 2006 preceded by a strong warming trend (0.74 °C per decade) since the early 1990s (Fig. II.1a).

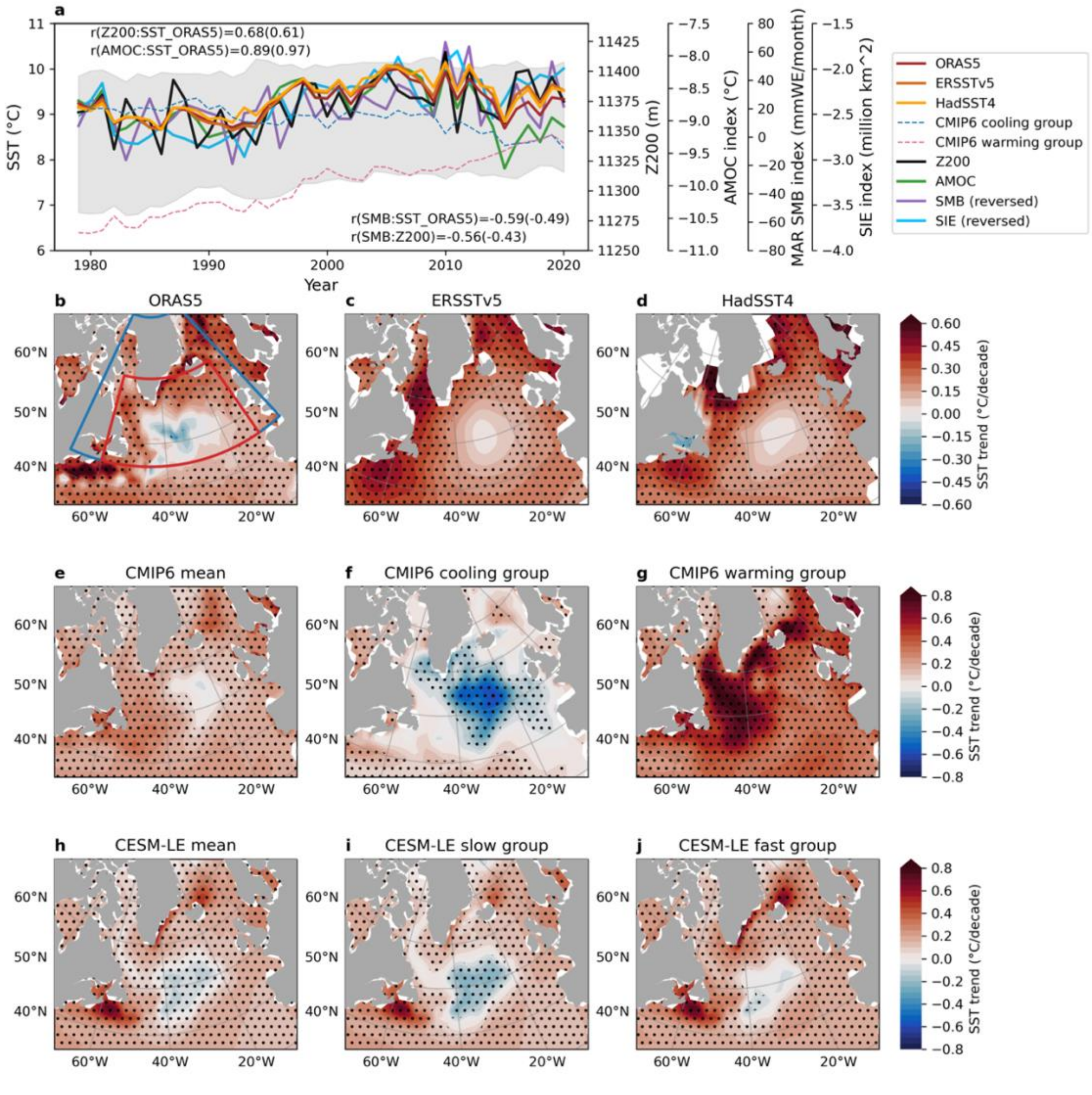

Figure II.1. a. Time series of annual mean SST in the subpolar North Atlantic Ocean (the region circled by the red contour in **b**) from reanalysis and observation data (ORAS5, ERSSTv5, and HadSST4), CMIP6 models (gray) with the cooling group (5 models with the largest decreasing trends, blue) and the warming group (5 models with the largest increasing trends, pink), Z200 in the subpolar North Atlantic (the region circled by the blue contour in **b**) from the ERA5 reanalysis (black), AMOC index using SST data from ORAS5 (green), south

GrIS surface mass balance (SMB) from MAR (purple), and SIE around Greenland in the subpolar North Atlantic (the region circled by the blue contour in **b**) from NSIDC (light blue). **b-j**: Linear trend (1979-2020) of annual mean SST from ORAS5 in **b**, ERSSTv5 in **c**, HadSST4 in **d**, CMIP6 models average in **e**, CMIP6 cooling group in **f**, CMIP6 warming group in **g,** CESM-LE 40 members average in **h**, CESM-LE slow group (6 members with the slowest increasing trends) in **i**, and CESM-LE fast group (6 members with the fastest increasing trends) in **j**. Black stippling in all trend plots indicates statistically significant trends at the 95% confidence level.

To investigate whether the observed trend patterns in the North Atlantic SST can be replicated in the climate system's response to anthropogenic forcing, 28 model historical simulations from CMIP6 and 40 members from CESM-LE are analyzed. Although the 1979-2020 SST trend from the ensemble mean of the 28 CMIP6 models aligns with the observed warming hole pattern (Fig. II.1e), a significant portion of the CMIP6 models generate very weak multi-decadal SST variability in the North Atlantic (Fig. II.1f&g). The SNA SSTs in CMIP6 show a wide range of responses, with some models exhibiting a significant SST increase over the SNA (these models are referred to as the warming group in the following analyses), while some others showing a slight cooling trend (referred to as the cooling group) over the past 42 years (Fig. II.1a). Intriguingly, the models in the cooling group, which are initially warmer, exhibit a trend towards slight cooling, whereas the models in the warming group, starting from a cooler state, show a more pronounced warming trend. This raises questions about the dependence of SNA SST variability in CMIP6 models on their initial or mean states: the initial SST conditions in the models may play a crucial role in determining their response to external forcings, leading to divergent SST trends in the region. This diverse performance across CMIP6 models is overlooked by previous studies, suggesting that the driving mechanisms behind SST changes in the SNA may differ substantially from model to model, and the processes contributing to observed multi-decadal SST changes might not be accurately reflected in most models.

Similarly, in the CESM-LE ensemble, a clear spread in the SST trends over the SNA in the past decade emerges. While each member can generally display the warming hole pattern over the past 42 years (Fig. II.1h), the extent and intensity of this cooling vary significantly among members. Some members exhibit a pronounced cooling patch (Fig. II.1i), while others show a relatively weaker cooling pattern (Fig. II.1j), suggesting an active role of internal low-frequency variability in regulating SST variability in the region.

The atmosphere-ocean coupling over the North Atlantic may be one reason that climate variability over the SNA exhibits strong low-frequency fluctuations in recent decades (He et al., 2022; Hu & Fedorov, 2020; L. Li et al., 2022), which is well demonstrated by a strong and coherent relationship between upper-level geopotential height and SST in the region. The annual mean SST and geopotential height at the tropopause at 200 hPa (Z200), averaged over the SNA (blue contour in Fig. II.1b, as the region within 45°N-65°N in latitude and 60°W-10°W in longitude), are highly correlated (r = 0.68 with trend, r = 0.61 without trend for annual mean values) (Table II.1). These SST and Z200 variabilities are also closely associated with sea ice extent (SIE) around Greenland and SMB changes within the southern Greenland domain in the MAR (Table II.1). The close relationship among all these variables in the region suggests that an integrated perspective is needed to fully understand the interactions between each component in the North Atlantic over the past four decades.

with trend **without trend**	**SST**	**Z200**	**SMB**	**SIE**
SST	1	**0.68**	**-0.53**	**-0.70**
Z200	**0.61**	1	**-0.50**	**-0.57**
SMB	**-0.43**	**-0.39**	1	**0.46**
SIE	**-0.61**	**-0.41**	**0.28**	1

Table II.1. Correlations between annual mean North Atlantic domain average SST, Z200, south GrIS SMB, and SIE around Greenland with trends and without trends respectively. All timeseries are same as those shown in **Fig. 1a**. Correlation coefficients in the upper diagonal part are calculated with trends, and ones in the lower diagonal part are calculated without trends.

C.1.2 Multi-decadal variability consisting of two epochs

To better illustrate decadal climate variability over the SNA in recent decades, we identify two prominent periods that exhibit significant differences in the rates and spatial patterns of SST changes: a 15-yr strong warming (0.74 °C per decade) from 1992 to 2006 and a 15-yr pronounced cooling (-0.53 °C per decade) from 2006 to 2020. In contrast to the long-term 42-year trend, the strong warming/cooling regions during these two epochs are situated poleward, to the south of Greenland (Fig. II.2a&b). During 1992-2006, the large-scale circulation changed towards a pattern with stronger anticyclonic anomalies (higher Z200) above Greenland, inducing easterly wind anomalies coinciding with surface ocean warming in the North Atlantic (Fig. II.2a). Conversely, during 2006-2020, the circulation trend was characterized by relatively stronger cyclonic anomalies (lower Z200) above southwestern Greenland, which favored westerly wind anomalies accompanied by cooling of the ocean surface in the region (Fig. II.2b). Sea ice around Greenland, namely in southern Baffin Bay, Davis Strait, and the northern Labrador Sea , and the southern GrIS SMB also shows synchronous changes with the variations in SST and large-scale circulation, featuring a significant melting during the warming epoch, followed by a decade-long “pause” with weak trends during the recent cooling epoch (Fig. II.2c-f).

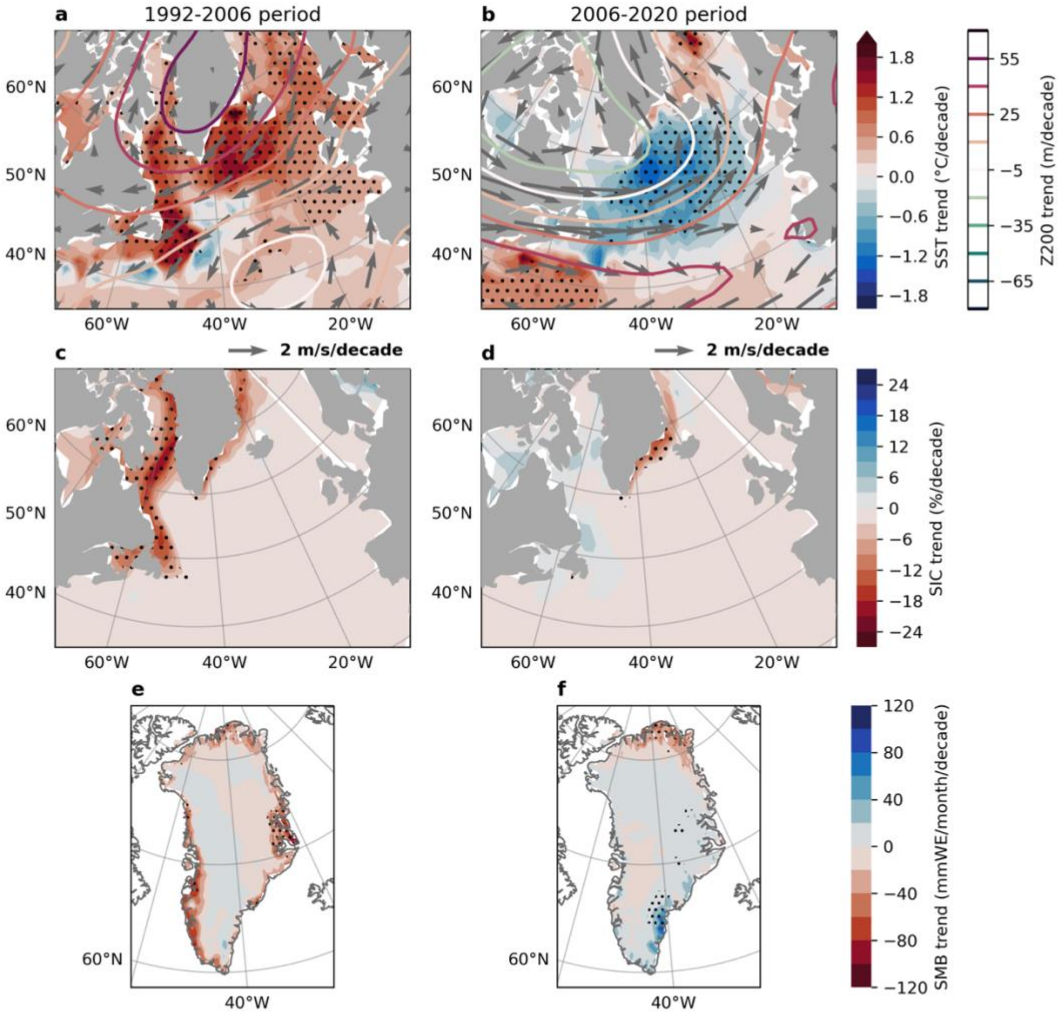

Figure II.2. a-b. Linear trend of annual ORAS5 SST (shading), ERA5 200hPa geopotential height (Z200, contours), and 200hPa horizontal winds (arrows) for the period 1992-2006 in **a**, and for the period 2006-2020 in **b**. **c-d**. The same as **a-b** but for sea ice concentration (SIC) from NSIDC. **e-f**. The same as **a-b** but for GrIS SMB from MAR. Black stippling in all plots indicates statistically significant trends at the 95% confidence level.

The correlation between the SNA domain average SST and the Z200 field is examined to further illustrate the spatial features of significant statistical connections between atmospheric circulation and SST changes in the region. A higher-than-average Z200, centered over southern Greenland, appears to highly correlate with warmer-than-average North Atlantic SST (Fig. II.3a). Importantly, this relationship exhibits a very similar and even stronger pattern when detrended variables are used (Fig. II.3a&d) and closely resembles the linear trend of Z200. This suggests that the impact of atmospheric circulation on North Atlantic SST changes also occurs on interannual time scales, and the local atmosphere-ocean coupling may share similar underlying mechanisms from interannual to interdecadal time scales. Furthermore, similar correlation patterns are also observed when correlating the southern GrIS average SMB and SIE around Greenland in the SNA (not shown) with the Z200 and SST fields (Fig. II.3b-c&e-f). The melting of the south GrIS SMB is highly correlated with a high-pressure trend in Z200 atop Greenland and a warming trend in SST to the south of Greenland, suggesting a strong sensitivity of the local cryosphere to the ocean-atmosphere coupling in the SNA. It has been suggested that these circulation anomalies in the SNA can regulate climate variability over the GrIS through adiabatic and horizontal temperature advection effects (Topál et al., 2022; Topál & Ding, 2023). These similar dynamical impacts may explain why we observe a strong relationship between circulation and both sea ice and SMB over the period.

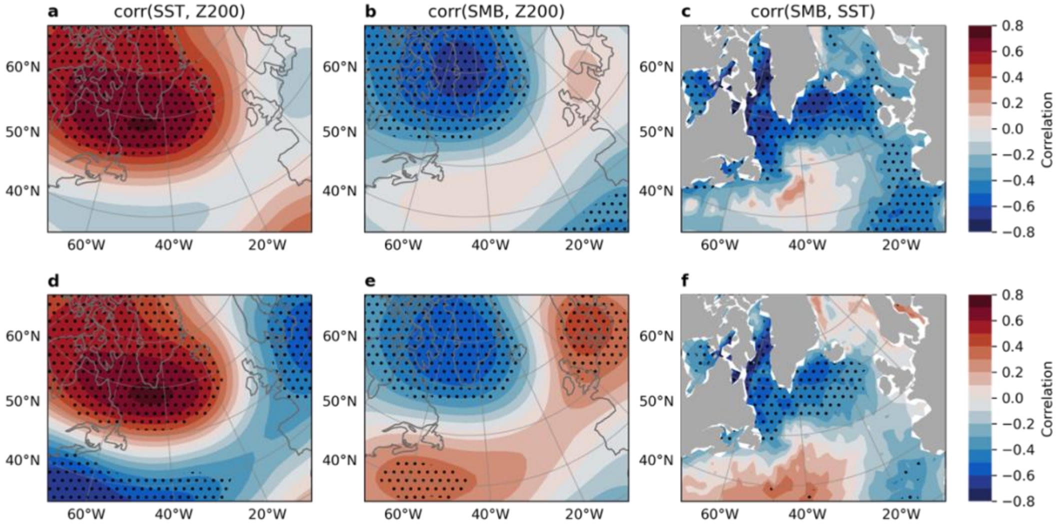

Figure II.3. a. Correlation of the subpolar North Atlantic domain average annual SST with the spatial field of annual Z200 from 1979 to 2020 with trend. b-c. Correlations of the south GrIS domain average annual SMB with the spatial fields of annual Z200 in **b** and SST in **c** from 1979 to 2020 with trend. **d-f**. The same as **a-c** but for correlations without trend. Black stippling in all plots indicates statistically significant correlations at the 95% confidence level.

C.2. Observed and simulated linkage between SST and overlying atmospheric circulation

C.2.1 MCA using observations

In this section, the deseasonalized, detrended monthly Z200 and SST fields in the North Atlantic are analyzed using MCA to investigate their possible connections on interannual time scales and explore how these linkages evolve when a phase lag is introduced between the two fields. By applying MCA and lead-lag analysis to both reanalysis data and numerous model results, we aim to understand the causality between atmospheric circulation and SST, and assess how models replicate the observed connection under different climate configuration settings.

Our analysis reveals that the leading coupled mode of MCA (MCA1), which accounts for approximately 71% of the covariance between Z200 and SST in the region, exhibits simultaneous and in-phase changes in both variables. Specifically, the warming trend pattern of SST in the North Atlantic (Fig. II.4a) is closely linked to a high-pressure anomaly in Z200 located above southern Greenland (Fig. II.4b), which closely resembles the observed correlation results (Fig. II.3a&d) and the trend pattern observed in Z200 (Fig. II.2). Moreover, the MCA1 monthly time series of the Z200 and SST patterns are significantly correlated over the past 42 years period (r = 0.36), exhibiting a similar temporal evolution with the observed variability in the raw fields, especially for SST (Fig. II.4c). In particular, MCA1 SST mode is closely related to the AMOC index generated using ORAS5 SST (r(MCA1 SST:AMOC) = 0.95, r(MCA1 Z200:AMOC) = 0.32). This may indicate that atmospheric processes, featuring single-cell high or low pressure centers in the SNA, have important impacts in determining the AMOC evolution on interannual time scales in recent decades, potentially through affecting surface currents, Ekman transports, and mixing processes between the surface and deeper ocean layers in the region (Cabanes et al., 2008; Roach et al., 2022).

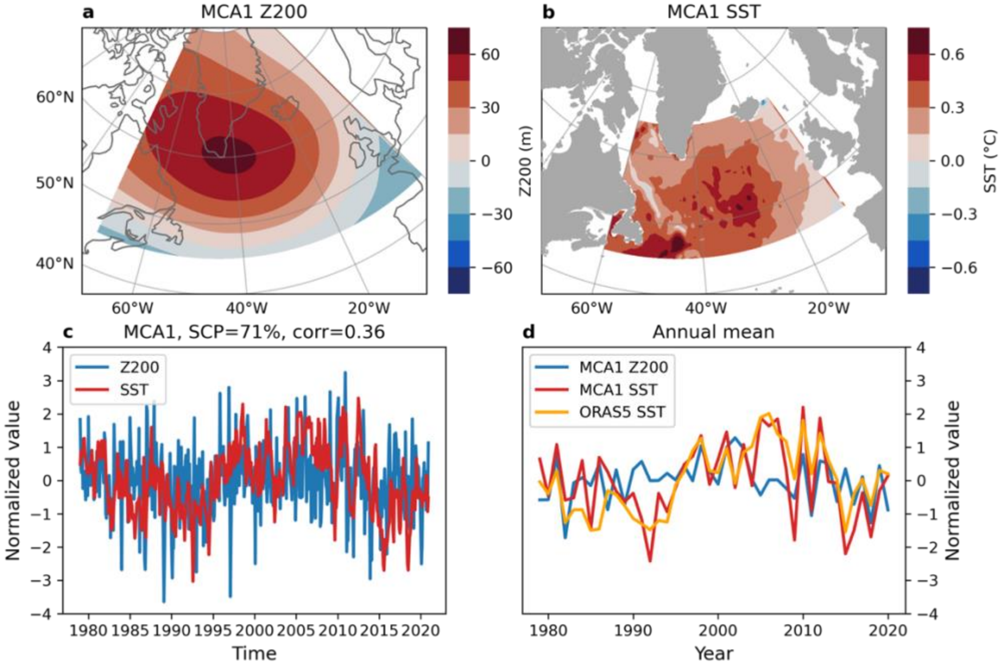

Figure II.4. a-b. The spatial patterns corresponding to the leading mode of the MCA (MCA1) of detrended monthly Z200 in **a**, and SST in **b**. **c**. The normalized time series of the MCA1 monthly Z200 (blue) and SST (red). **d**. The same as **c**, but for annual mean averaged, and showing the normalized values of subpolar North Atlantic domain average SST from ORAS5 (orange). The regions of Z200 and SST that selected for the MCA are consistent with the regions used to calculate indices in Fig. 1a (red/blue contours in Fig. 1b). The squared covariance fraction (SCF) that showed in **c** indicates the leading mode accounts for 71% of the covariance, and the correlation between two normalized monthly time series showing in **c** is 0.36.

To focus on year-to-year variability, we also construct the annual mean variability of the MCA1 modes by averaging monthly time series for each calendar year. However, the annual mean of the MCA1 Z200 time series displays less consistency with SST time series (Fig. II.4d). One possible explanation is that MCA is performed using detrended monthly variables, and Z200 may only be strongly connected with SST during certain months of the year. To explore which months exhibit Z200 and SST connections, we calculate the correlation of MCA1 Z200 and SST time series for each month and find that the two fields are most strongly related in the summer months of June, July, and August (not shown). These results provide clear evidence that the large-scale atmospheric circulation and surface ocean in the SNA are statistically connected on interannual time scales, and this relationship mainly occurs in boreal summer.

The MCA results demonstrate the presence of a simultaneous co-existing coupling pattern between atmospheric circulation and SST in the SNA, yet the causality between these two variables remains uncertain. To further examine their causal relationship, we perform lead-lag correlation analyses extending up to 12 months. Due to the robust nature of the 1-3 month lead-lag correlations (Fig. II.5), we focus on these periods using the MCA1 Z200 index correlated with the observed spatial fields of detrended monthly SST. The upper-ocean warming appears to be preceded by changes in atmospheric circulation as shown by the notable relationship when Z200 leads SST (Fig. II.5a&e-g). This relationship is particularly prominent with a lead time of one month (Fig. II.5e), and it is stronger than the simultaneous (i.e., lag-0 month) correlation (Fig. II.5a). In contrast, the correlations of SST preceding Z200 show some significant spatial patterns but are notably weaker than those when Z200 leads SST. This suggests that SST in the SNA exhibits a significant response to large-scale atmospheric forcing in the month that follows. Considering the strong similarity of SST-Z200 coupling on interannual- to low-frequency time scales, this result implies that a substantial portion of the observed SST warming/cooling trend over the past four decades in the SNA is likely an oceanic response to large-scale atmospheric circulation changes on interdecadal time scales.

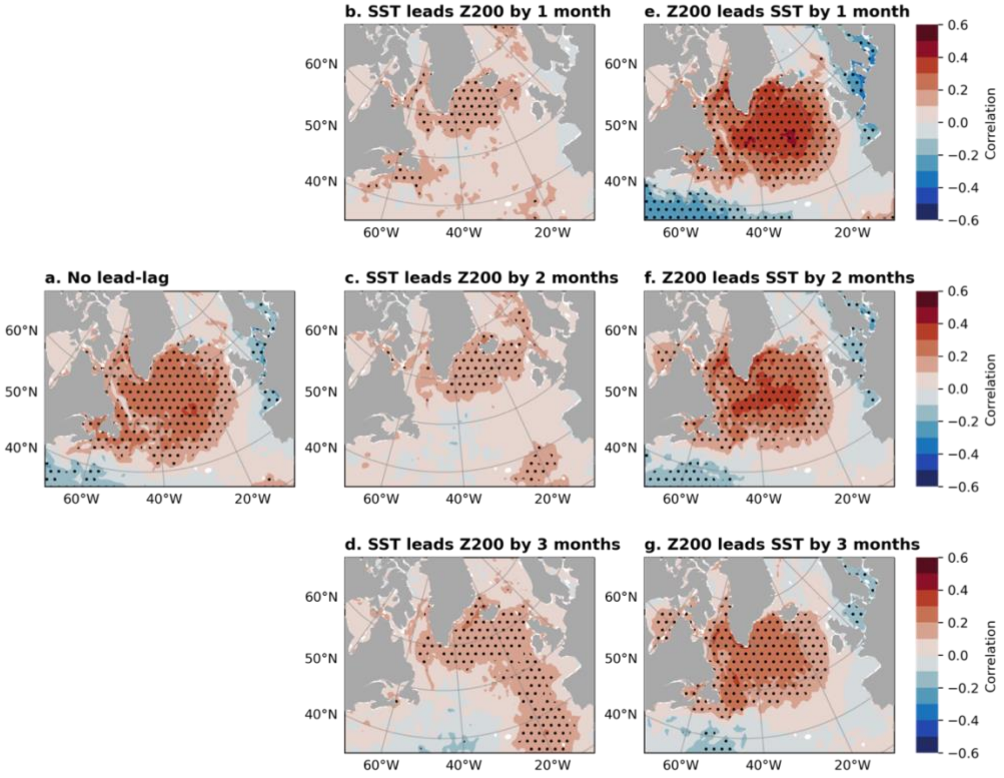

Figure II.5. a. Correlation of monthly Z200 index from MCA1 with the spatial field of monthly detrended SST from ORAS5 from 1979 to 2020. **b-c**. The same as **a**, but for lead-lag correlations (SST leading) up to 3 months. e-g. The same as **b-d**, but for Z200 leading correlations up to 3 months. Black stippling in all plots indicates statistically significant correlations at the 95% confidence level.

C.2.2 MCA in the climate model ensembles

To further investigate the observed coupling between atmospheric circulation and SST in climate models, we conduct MCA analysis on different numerical model results, including GOGA, CESM-LE, and a long (1800 yr) pre-industrial run by CESM1. Comparing each of these with the observed MCA1 result (Fig. II.4) enables us to explore the sensitivity of large-scale atmospheric circulation to SSTs in different climate scenarios.

The MCA1 result using GOGA with prescribed SST fails to replicate the observed Z200 pattern and magnitude as seen in the MCA1 result using ERA5 and ORAS5 datasets (Fig. II.6a&b), displaying a substantially weaker Z200 over southern Greenland (Fig. II.6g&h). This discrepancy implies that imposing observed SST changes alone in CESM1 may not be sufficient to aid the model in fully reproducing observed ocean-atmosphere interactions in the SNA. On the other hand, MCA1 derived from the historical runs of CESM-LE demonstrates a reasonable skill in reproducing a similar coupling as observed, although magnitudes of these patterns are weaker (Fig. II.6j&k). The same analysis using the pre-industrial run, which only reflects internal variability of the model system, yields a coupling pattern more closely aligned with that observed (Fig. II.6m&n). This strong resemblance implies that internal variability plays a key role in contributing to the generation of this ocean-atmosphere interaction captured by the MCA mode (Fig. II.2) regardless of the presence of anthropogenic forcing.

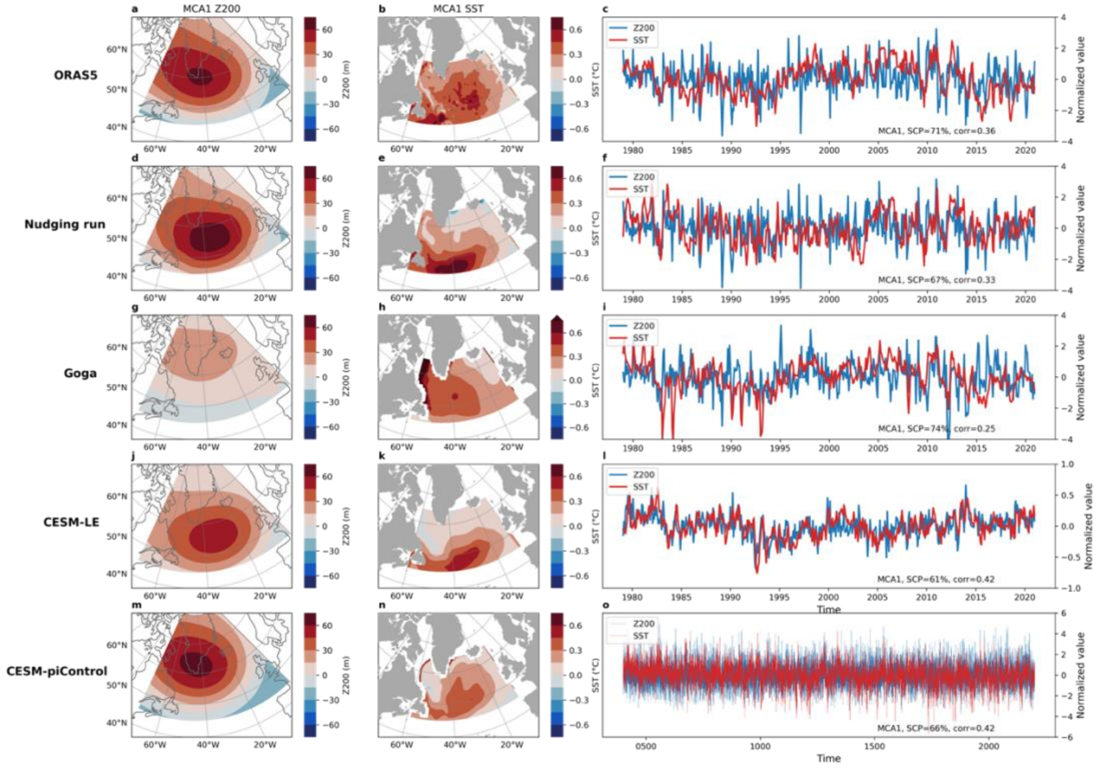

Figure II.6. a-b. The spatial patterns corresponding to the leading mode of the MCA (MCA1) of monthly detrended Z200 in **a**, and SST in **b** from ORAS5. **c**. The normalized time series of the MCA1 monthly Z200 (blue) and SST (red) from ORAS5. These results are same as Fig. 4 but for better comparison with other results here. **d-o**. The same as **a-c**, but from the wind-nudging experiment in **d-f**, CAM6 Prescribed SST AMIP Ensembles mean (GOGA) in **f-i**, CESM-LE (MCA for each member and then average) in **j-l**, and 1800 years CESM1 pre-industrial control run in **m-o**.

We also repeat the lead-lag correlation analysis using the time series from the MCA1 of the CESM-LE (Fig. II.7b&j-o) and the pre-industrial run (Fig. II.7c&p-u), and the results exhibit a remarkable similarity to those seen in the observational counterpart (Fig. II.5). Clearly, the surface ocean and tropospheric circulation over the SNA in these runs demonstrate a robust lead-lag relationship that is stronger than the simultaneous correlations, in which Z200 significantly leads both SST and the AMOC index by one month. This one-month lead of Z200 indicates a clear direction of the causality in the establishment of local atmosphere-ocean interaction over the SNA, whereby atmospheric circulation variability drives ocean changes on interannual time scales.

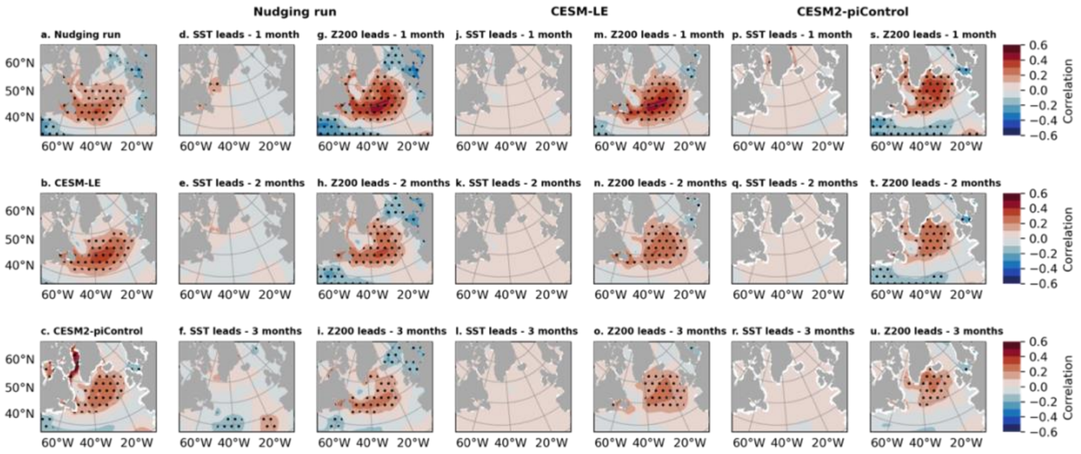

Figure II.7. a-c. Correlation of monthly Z200 index from MCA1 with the spatial field of original monthly detrended SST from 1979 to 2020 from the wind-nudging experiment in **a**, CESM-LE (correlation for each member and then average) in **b**, and CESM pre-industrial control run in **c**. **d-i**. The lead-lag correlations between MCA1 Z200 index and SST field up to 3 months from wind-nudging experiment, with SST leading in **d-f**, and Z200 leading in **g-i**. **j-o**. The same as **d-i**, but for CESM-LE (correlations for each member and then average). **p-u**. The same as **d-i**, but for CESM pre-industrial control run. Black stippling in all plots indicates statistically significant correlations at the 95% confidence level.

C.3. Underlying local mechanism driving the air-sea interactions

C.3.1 The inferred mechanism linking atmospheric changes with SST

To better understand how atmospheric circulation affects SSTs in the SNA, we next investigate the observed changes in surface heat flux and poleward ocean heat transport (POHT) associated with atmospheric circulation and SST in the region, considering that these two processes commonly serve as the key bridging effects in linking the atmosphere with SST in the extratropics. POHT, largely affected by large-scale ocean dynamics at a longer timescale, is also partially driven by winds on relatively shorter, interannual timescales (Lien et al., 2017; Madonna & Sandø, 2022; Orvik & Skagseth, 2003). We focus on the POHT in the upper 50m in this study, as this layer is the most sensitive to changes in heat transport and surface ocean temperature variations in the SNA (Z. Li et al., 2022). While previous studies have emphasized the contribution of AMOC slowdown to the reduction in ocean heat transport in this region (Caesar et al., 2018; Rahmstorf et al., 2015), the impact of atmospheric changes on recent POHT changes in the SNA may not be trivial.

An SNA SST index, derived from the leading mode of MCA analysis, shows a high correlation with the upper 50m POHT entering the SNA at 45°N ($r = 0.51$ without trend) (Fig. II.8a). It is also positively correlated with net downward heat flux (Q_{net}) averaged over the region, albeit with a lower magnitude ($r = 0.33$ without trend) (Fig. II.8a). Importantly, POHT exhibits a patch of significant correlations to the south of Greenland with both SST and Z200 (Fig. II.8b&c), despite the signal of related SST extending into the Denmark Strait (Fig. II.8b). One feasible way to explain these co-variabilities between POHT, SST, and Z200 is that large-scale atmospheric circulation controls SST by driving upper oceanic currents and consequently regulating POHT. The same mechanism may also operate on low-frequency timescales. During the warm period of 1992-2006, strong easterly winds over the SNA could potentially warm the underlying ocean by driving anomalous Ekman flow that transports warm low-latitude water poleward (Fig. II.2a). In contrast, strong westerlies inhibit low-latitude water influx and support the transport of high-latitude waters southward during the cold period after 2010 (Fig. II.2b).

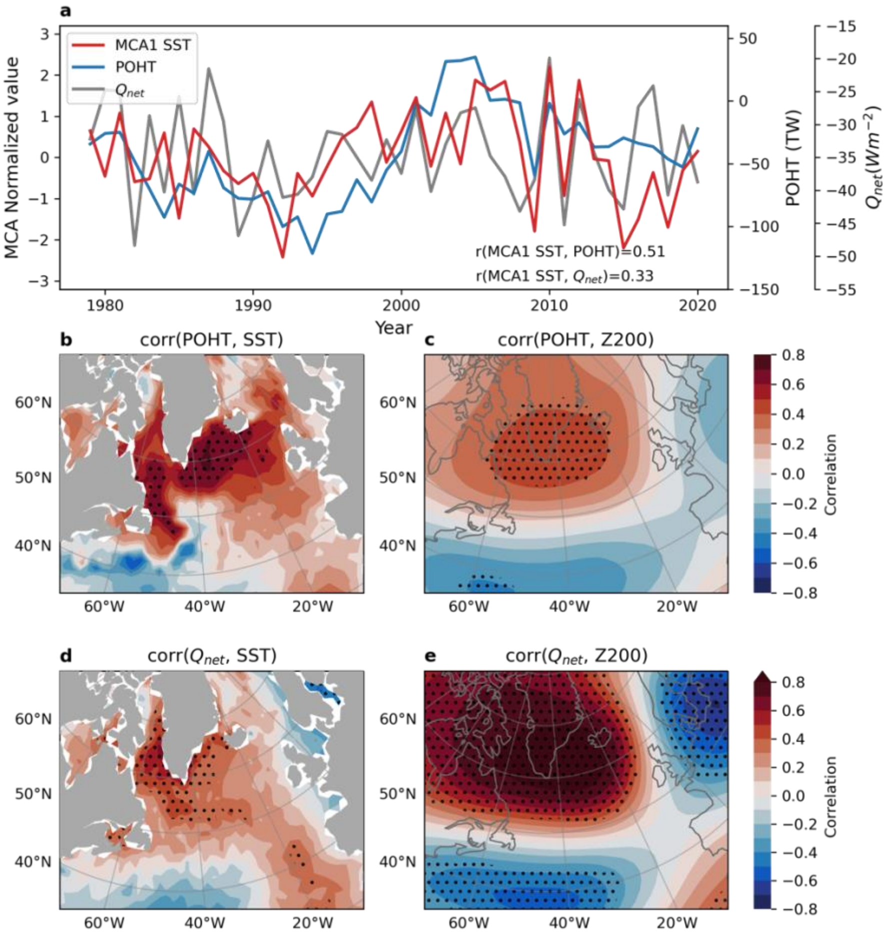

Figure II.8. a. Time series of annual SST derived from the leading mode (MCA1) of the MCA analysis (red), upper 50m annual poleward ocean heat transport (POHT) across the gate along the south boundary of the subpolar North Atlantic (40°W-20°W longitude at 45°N latitude, defined as the red contour in Fig. 1b) from ORAS5 (blue), and the North Atlantic domain average annual net downward heat flux (Q_{net}) from ERA5 from 1979 to 2020 (gary). **b-c**. Correlations of 1979-2020 annual upper 50m POHT from **a** with the spatial fields of SST in **b**, and Z200 in **c**. **d-e**. Correlations of 1979-2020 annual Q_{net} from **a** with the spatial fields of SST in **d**, and Z200 in **e**. All linear trends are removed in calculating the correlations in **b-e**. Black stippling in all plots indicates statistically significant correlations at the 95% confidence level.

Although Q_{net} is also strongly correlated with SST and Z200 over south Greenland (Fig. II.8d&e), the linear trend of Q_{net} is relatively small from 1979 to 2020 (Fig. II.8a), lacking the pronounced increasing trend during 1992-2006 and the subsequent decreasing trend observed from 2006 to 2020. Hence, it appears that Q_{net} is less important than POHT in shaping SST change over the region over decadal time scales and surface fluxes may only act as the secondary process in contributing to the long-term SST changes in the SNA.

C.3.2 Assessing winds-driven SST changes using wind-nudging experiments in CESM1

To assess the role of winds in driving SST changes in the SNA more directly, we conduct a nudging experiment without time-varying anthropogenic forcing. To do so, we nudge the North Atlantic winds of CESM1 to the ERA5 reanalysis from 1979 to 2020 while anthropogenic forcing is set to a constant value at the level of the year 2000 (CO_2 = 367 ppm), which is near the climatological mean value of CO_2 concentration over our 42-yr study period. The details of experimental set-up can be found in Section 2.7. Comparing the nudging experiment with the historical simulations of the same model (CESM-LE) and the observational evidence (ORAS5) will help us study the relative roles of wind-driven and anthropogenic forcing in recent SST changes in the SNA.

The simulated SNA domain average SST shows a highly correlated temporal variation with ORAS5 SST (r = 0.14 with trend, r = 0.50 without trend) from 1979 to 2020 on both interdecadal and interannual time scales (Fig. II.9a). The weak correlation (with trend) using the raw data may be due to a warm initial bias in our simulation which is closely related to the warmer initial oceanic condition over the North Atlantic. The correlation is much improved when the focus is directed on the recent 30 years from 1990 to 2020 (r = 0.65 with trend, r = 0.67 without trend). Since a more realistic oceanic initial condition over the region requires a long spin-up time and the nudging simulation is computationally expensive, our following analysis skips the first decade and only focuses on the last 30 years of our 42-year simulation.

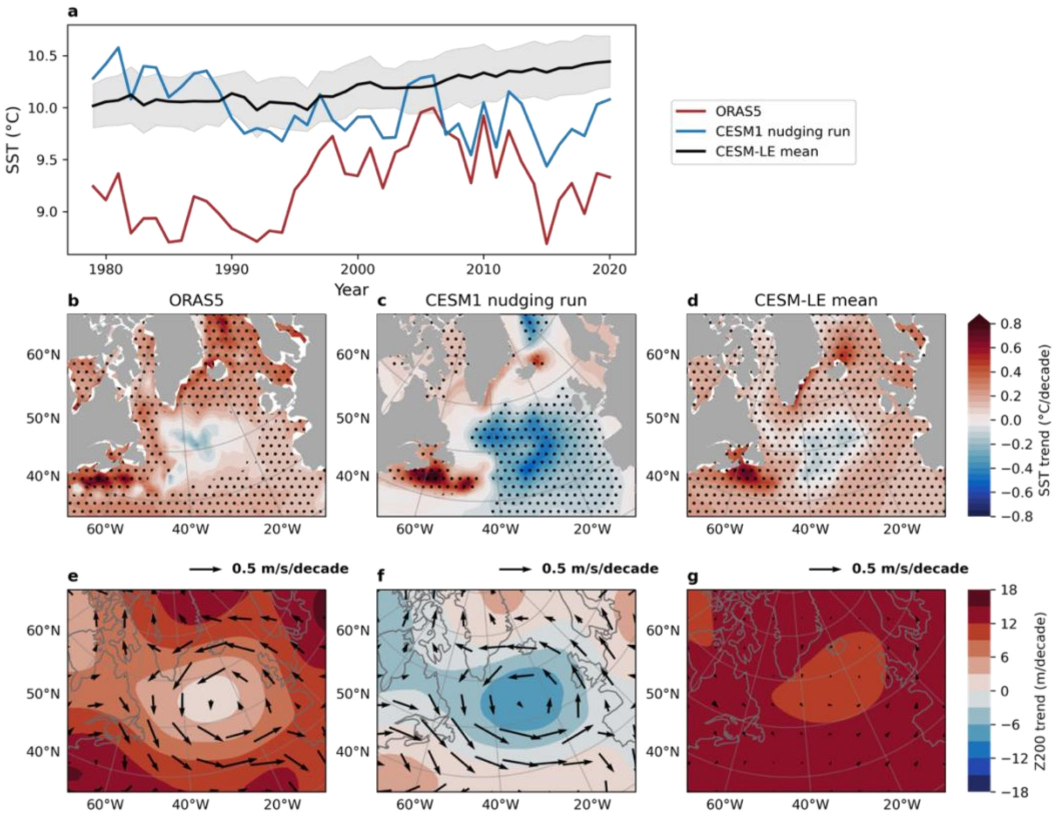

Figure II.9. a. Time series of annual subpolar North Atlantic domain average SST from ORAS5 (red), the wind-nudging experiment (blue), and CESM-LE 40 members average (black, the spread in CESM-LE in grey shading). **b-d**. Linear trend of SST from ORAS5 in **b**, the wind-nudging experiment in **c**, and CESM-LE 40 members average in **d** from 1979 to 2020. **e-g**. Linear trend of Z200 (shading) and horizontal winds at 200 hPa (vectors) from ORAS5 in **e**, the wind-nudging experiment in **f**, and CESM-LE 40 members average in **g** from 1979 to 2020. Black stippling in all plots indicates statistically significant trends at the 95% confidence level.

As for the spatial trend patterns, constraining observed winds in the model results in a stronger-than-observed SST cooling in the SNA (Fig. II.9b&c), which may also be due to the relative warm starting point in 1979 in the nudging experiment (Fig. II.9a) and a stronger low-pressure trend in the region compared with the observations during 1979-2020 (Fig. II.9e&f). This nudging run can be compared with the response of CESM1 to anthropogenic forcing in CESM-LE, providing insights on how the same model separately responds to anthropogenic forcing and observed winds during the same period. The forced response of the SST in the ensemble average of the CESM-LE shows a similar pattern to the observed one, although the wind trend in the CESM-LE mean is very weak, and the geopotential height field is nearly uniform (Fig. II.9d&g). This suggests that the observed wind changes are largely due to internal variability of the climate system and that the cooling SNA SST signal seen in CESM-LE is not due to wind changes considering that the observed wind trend pattern is not created by the model's forced response.

Although the cold patch in the subpolar gyre region is present in CESM-LE, its relationship with POHT differs substantially from that in ORAS5 with an increasing POHT trend in the model, suggesting an influx of oceanic heat transport to the SNA (Fig. II.10). On the contrary, imposing observed regional winds in our experiment enables a simulation that strongly resembles the annual POHT interannual variabilities seen in the ORAS5 reanalysis (Fig. II.10; 1979-2020 period: r = 0.30 with trend, r = 0.65 without trend; 1990-2020 period: r = 0.42 with trend, r = 0.65 without trend). As for interdecadal time scales, the simulated POHT captures the counterpart in ORAS5 with the increasing trend from 1992 to 2006 followed by the strong, decreasing trend after 2006 (Fig. II.10). This suggests that the observed circulation pattern is a necessary forcing factor to make the model accurately capture all key physical elements associated with the local coupling in the real world. Although CESM-LE, forced by anthropogenic forcing, can reproduce the SNA SST cooling component of observed changes, the underlying mechanism contributing to this cooling in the model is different from that in reality.

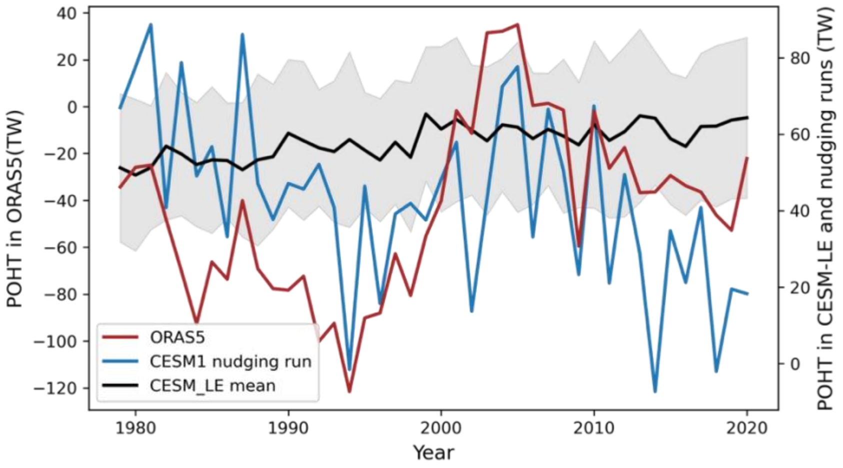

Figure II.10. Time series of upper 50m annual poleward ocean heat transport (POHT) across the gate along the south boundary of the subpolar North Atlantic (40°W-20°W longitude at 45°N latitude, defined as the red contour in Fig. 1b) from ORAS5 (red), the wind-nudging experiment (blue), and CESM-LE 40 members average (black, the spread in CESM-LE in grey shading) from 1979 to 2020.

As those MCA performed on observations and models in *Section C.2.2*, the MCA1 results based on the wind-nudging experiment (Fig. II.6d-f) also bear a strong resemblance to those derived from the observation (i.e., ERA5&ORAS5; Fig. II.6a-c). This similarity signifies a governing role of atmospheric circulation (as indicated by Z200) on SST to the south of Greenland, although the SST response from the wind-nudging experiment's MCA1 is located slightly southward compared to the observed pattern (Fig. II.6b&e). The MCA1 coupled modes from the observation and the wind-nudging experiment account for the majority of the covariability (71% for the observation and 67% for the wind-nudging experiment) between large-scale circulation and SST. These MCA results along with the comparison of the nudging run with CESM-LE collectively suggest that large-scale winds play a critical role in driving POHT entering the SNA and therefore act as the key mechanism bridging the atmosphere and ocean in the region.

C.4. Remote forcing of the SNA air-sea interaction

C.4.1 The teleconnection pattern in past decades

The wind-nudging experiment highlights the impacts of large-scale winds on SST changes in the SNA since 1979, mainly through modulating the POHT into the region. To better understand the origin of this large-scale wind variability, we expand our focus to a global scale picture of the large-scale circulation pattern. Previous studies have revealed a robust atmospheric “Pacific-Arctic” teleconnection (referred to as the PARC in Baxter et al., 2019) emanating from SST changes in the east-central tropical Pacific Ocean (ETPO) via a Rossby wave train propagating into the Arctic (Baxter et al., 2019a; Ding et al., 2014). It is reasonable to expect that a similar teleconnection exists and the observed winds and related atmospheric processes over the North Atlantic are also likely influenced by remote tropical forcing, rather than being solely driven by local SST changes.

Analyzing the annual mean SST trends on a global scale shows an out-of-phase pattern between SST trends in the ETPO and SNA over the recent four decades, with the SNA reveals a cooling SST trend, while the ETPO displays a warming pattern (Fig. II.11a). This contrast has become particularly pronounced in the recent 15 years from 2006 to 2020 (Fig. II.11c). Concurrently, Z200 trend shows a similar opposite-sign dipole pattern between the North Pacific and the broader Greenland region (Fig. II.11d-f). Regressing MCA1 Z200 annual mean time series on the raw SST field exhibits a hemispheric teleconnection bridging atmospheric circulation variability over the North Atlantic with opposite-sign changes of SST in the ETPO and positive SST anomalies in the tropical Atlantic (Fig. II.12a). Similarly, regressing MCA1 SST time series on the raw Z200 field reveals a similar teleconnection pattern, though with weaker signals over the ETPO (Fig. II.12d). This teleconnection resembles the PARC teleconnection, confirming a possible role of tropical remote effects in forcing the mid-tropospheric high pressure pattern over Greenland, which further drive the changes of SST over the SNA. Importantly, the same calculation derived from the wind-nudging experiment closely resembles the spatial patterns seen in reanalysis (Fig. II.12b&e), while CESM-LE fails to capture the remote signals over the ETPO (Fig. II.12c&f). These results suggest that a substantial portion of the observed local circulation-SST coupling in the North Atlantic is likely driven by remote tropical forcing through the PARC over the past decades, as suggested by several previous studies (Baxter et al., 2019; Bevis et al., 2019; Ding et al., 2014; Meehl et al., 2018).

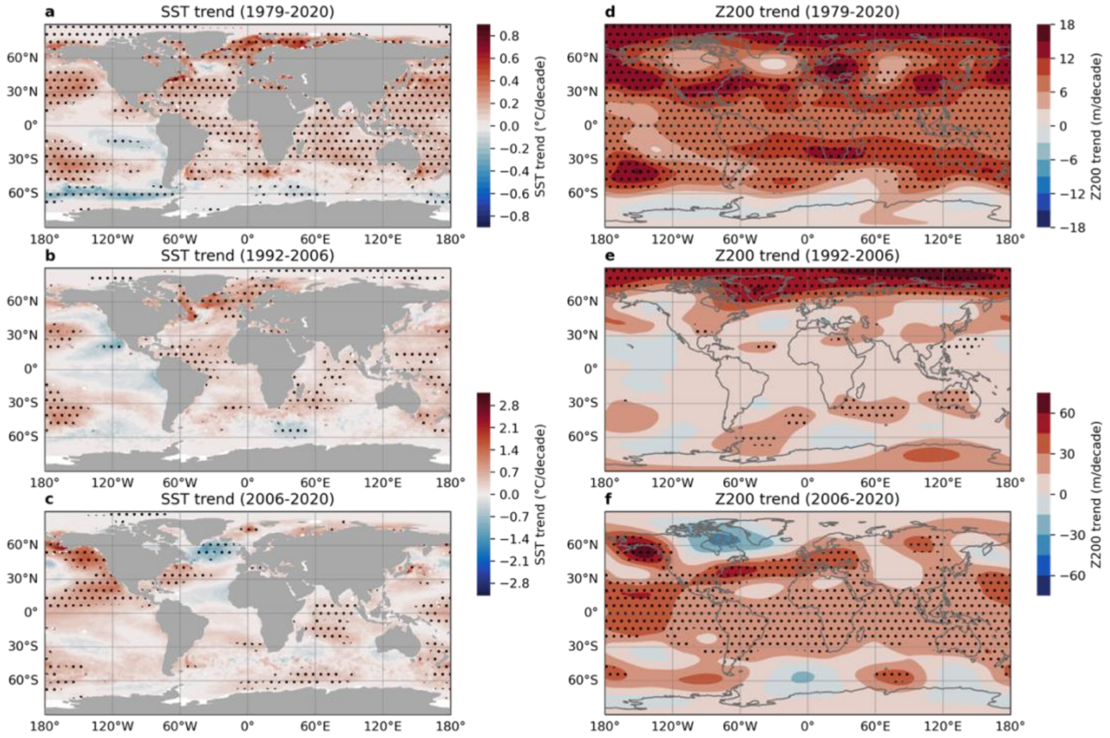

Figure II.11. a-c. Linear trends of annual SST from ORAS5 for the period 1979-2020 in **a**, for the period 1992-2006 in **b**, and for the period 2006-2020 in **c**. **d-f**. The same as **a-c**, but for annual Z200. Black stippling in all plots indicates statistically significant trends at the 95% confidence level.

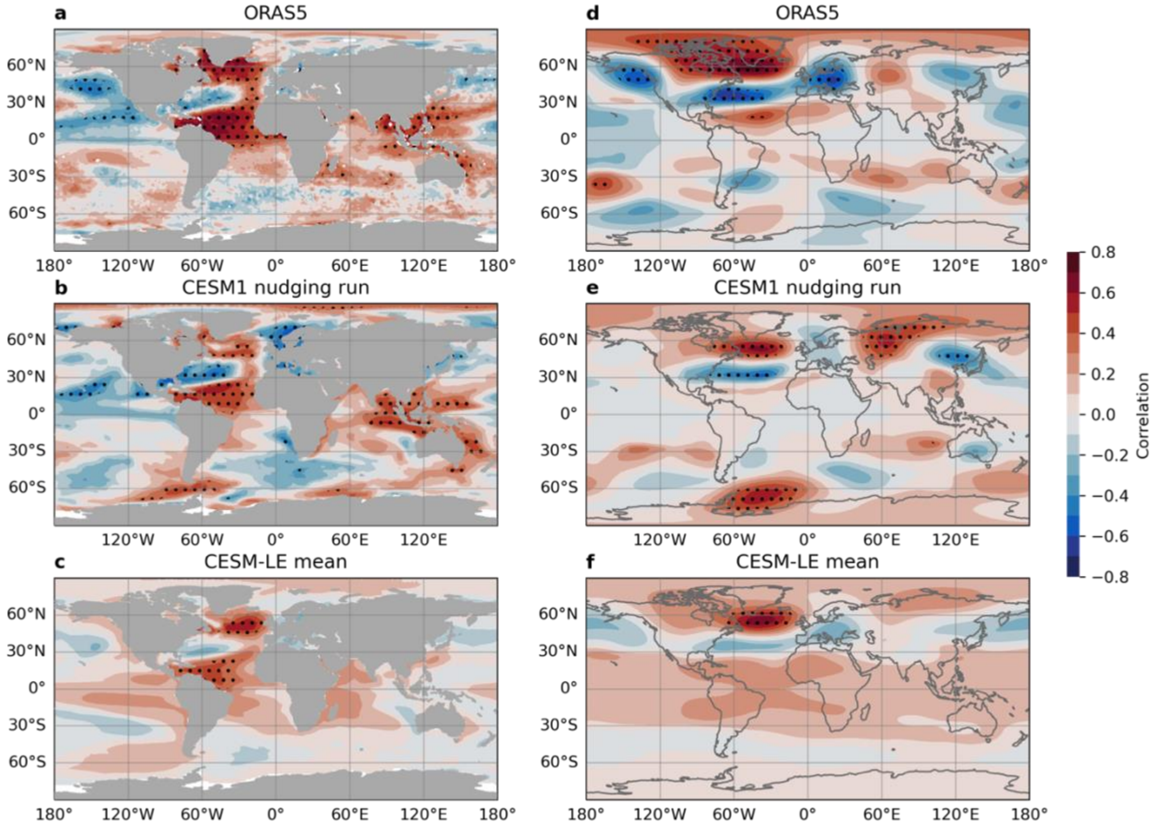

Figure II.12. a-c. Correlations of annual mean MCA1 Z200 index with SST field from ORAS5 in **a,** the wind-nudging experiment in **b**, and CESM-LE 40 members average in **c**. **d-f**. Correlations of annual mean MCA1 SST index with Z200 field from ERA5 in **d**, wind-nudging experiment in **e**, and CESM-LE 40 members average in **f**. All linear trends are removed in calculating the correlations. Black stippling in all plots indicates statistically significant correlations at the 95% confidence level.

C.4.2 Teleconnections to the tropical Pacific over the past 150 years

One limitation of diagnostic analyses and wind-nudging simulations previously discussed is that they only cover a 42-yr period which is not sufficient long to fully reflect internal long frequency variability and possible imprints of anthropogenic forcing in the region. To address this concern, we extend our analysis by performing MCA on the EKF400v2 paleo-reanalysis data. It aims to examine the atmospheric circulation pattern that is closely associated with changes of SST in the SNA and to assess whether this large-scale mechanism is stable over multiple-decadal time scales in the past two centuries, specifically from 1854 to 2003. This is the period in which ERSSTv5 records are available and the proxy data (e.g., corals, tree rings, ice cores) are more abundant.

Having repeated the same MCA between deseasonalized, detrended monthly Z500 (the only available level in the EKF400v2) and SST in the region, as in *Section C.2,* the leading internal Z500-SST coupled modes (Fig. II.13a&b), derived from EKF400v2 and ERSSTv5 datasets, feature strikingly similar spatial patterns to their observed counterparts (Fig. II.4a&b). These modes explain approximately 57% of the covariance and dominate the linkage of the two fields, implying that the observed large-scale winds and SST coupling in the SNA is robust over the past 150 years, predominantly arising from internal variability of the climate system. To further examine whether these modes are connected with remote SST and Z500 on a global scale, we regress the MCA1 Z500 and SST annual mean time series on the raw SST and Z500 fields, respectively (Fig. II.13d&e). The results depict spatial teleconnection patterns that largely resemble the observed patterns since 1979 (Fig. II.12a&d), highlighting the linkage between atmospheric circulation variability over the SNA and the concurrent in-phase changes in SST in both the SNA and tropical Atlantic. In particular, its related Z500 signal exhibits a clear feature of the cold-SST anomaly-driven Gill pattern response in the Eastern tropical Pacific (Fig. II.13e; Gill, 1980), indicating that over interdecadal time scales, the local air-sea interactions in the SNA are also very likely driven by remote tropical forcing through atmospheric teleconnections. The SST and Z500 signals over the ETPO (Fig. II.13d&e) also show some similarities to patterns observed in recent decades (Fig. II.12a&d), which suggests that the PARC mode represents a stable low-frequency teleconnection mode linking the SNA and the tropical Pacific over the past 150 years. Considering the robustness of this connection, we believe that recent interdecadal variability in the SNA region may be partially driven by the PARC, which results from internal variability originating in the tropical Pacific.

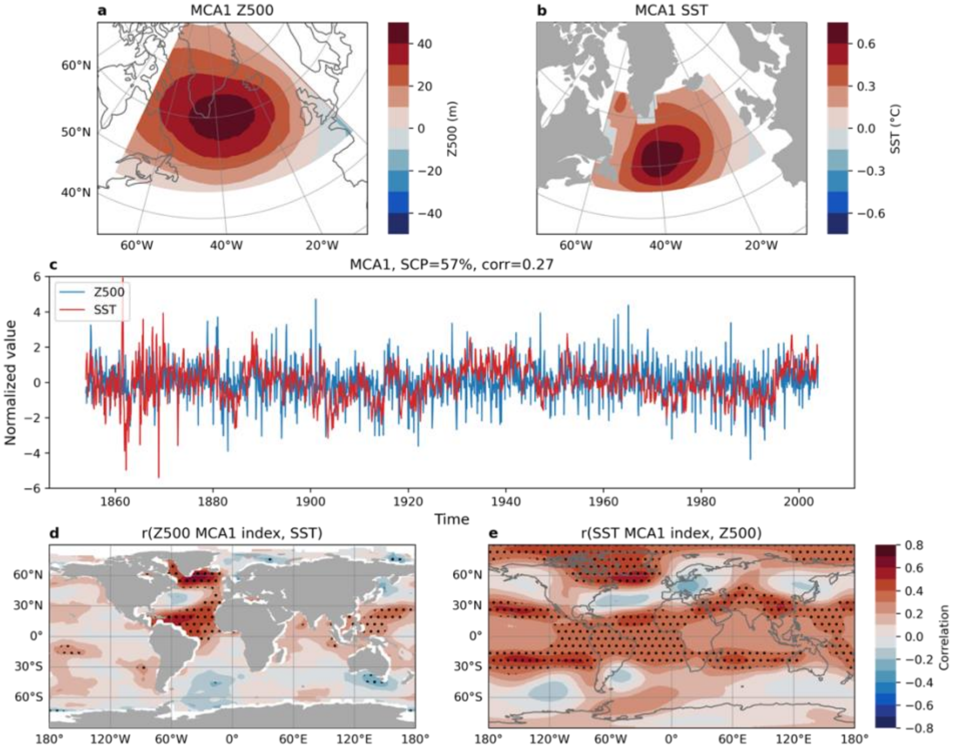

Figure II.13. a-b. The spatial patterns corresponding to the leading mode of the MCA of detrended monthly Z500 from EKF400v2 in **a**, and SST from ERSSTv5 in **b**. **c**. The normalized time series of the MCA1 monthly Z500 (blue) and SST (red). **d**. Correlation of annual mean MCA1 Z500 index with SST field from ERSSTv5 from 1854 to 2003. **e**. Correlation of annual mean MCA1 SST index with Z500 field from EKF400v2 from 1854 to 2003. All linear trends are removed in calculating the correlations. Black stippling in all plots indicates statistically significant correlations or trends at the 95% confidence level.

D. Discussion

In this study, by performing various statistical and diagnostic analyses on reanalysis data and existing model results, and conducting a novel wind-nudging experiment, we illustrate several key findings:

1. Large-scale atmospheric circulation explains a substantial portion of the observed SST, upper POHT, and AMOC variabilities in the SNA through a wind-driven process operating on both interannual and interdecadal time scales.

2. The anticyclonic high-pressure/cyclonic low-pressure system, accompanied by stronger easterly/westerly winds in the region, could contribute to warming/cooling of the underlying ocean, sea ice melt/expansion around Greenland in the SNA, and GrIS ice mass loss/growth through driving anomalous Ekman flow and local surface heat flux exchange.

3. This atmospheric process is partially driven by forcing originating from the tropical Pacific through an atmospheric teleconnection.

Our findings underscore the significance of internally-driven atmospheric processes in strengthening the high latitude atmosphere-ocean interaction and related ocean heat transport and AMOC that shapes multidecadal climate variability in the North Atlantic over interdecadal timescales.

These atmosphere-ocean coupling mechanisms over the SNA identified in the observations and our nudging experiments are neither captured in the CESM-LE nor individual member runs, raising a concern about models' skill in simulating multidecadal SST variability over the North Atlantic. Given that the identified mechanism is critical in influencing local and remote climate, our study highlights the need for a more thorough understanding of the observed intricate interplay between atmospheric processes, upper ocean, and cryosphere, and related mechanisms shaping long-term regional climate variability in the SNA. Moreover, diverse performance of CMIP6 models in replicating observed SST changes in this region may also indicate that more efforts should be devoted to assessing the source of individual model's biases in simulating the key physical processes related to this observed atmosphere-ocean coupling (Topál et al., 2022).

This study primarily focuses on SST changes in the subpolar gyre and their role in the atmosphere-upper ocean-ice coupling. However, we recognize the importance of subsurface ocean waters in impacting the mass balance of Greenland glaciers as these mediate a large proportion of the total mass balance near the end of the 1990s. Previous studies have highlighted the crucial role of enhanced intrusions of subsurface warm Atlantic Waters in the retreat of Greenland glaciers (Holland et al., 2008; Wood et al., 2021) and loss of northern Baffin Bay ice cover (Ballinger et al., 2022), but the impact of large-scale winds on the transport of these deep waters around south Greenland is not studied in this work. Therefore, it is imperative to conduct further studies to better understand the integrated effect of atmospheric circulation and ocean transport and how state-of-the-art climate models need to be improved to capture observed variability and underlying mechanisms behind the region's atmosphere-ocean-ice coupling.

Studies have recently suggested that the AMOC is susceptible to global warming forcing, and it is expected to slow-down or potentially collapse around mid-century according its recent changes (Ditlevsen & Ditlevsen, 2023; Weijer et al., 2020). Our findings suggest that internal atmospheric circulation forcing may, in part, imprint some signals on recent AMOC variability. These new results indicate that the recent changes in the AMOC could be a result of both anthropogenic impacts and natural climate variability, although we note the limitations of using SST as a proxy for AMOC changes, especially considering the limited observational evidence of long-term AMOC. Thus, it is still premature to argue that the recent variability of the AMOC signals a potential collapse in the next decades. In particular, the extent to which the recent observed AMOC changes were driven by internal climate variability versus anthropogenic forcing remains unclear. A better quantification of their relative forcing over the historical era is the first step needed to aid us in better projecting the future state of the AMOC. Our study makes some contribution to the ongoing debate about this topic and provides a new perspective to study the future change of the AMOC.

The existence of cross-basin teleconnection from the tropical Pacific to the North Atlantic is also essential to understanding regional air-sea interactions in the SNA. Nevertheless, we acknowledge that the skill of current mode in simulating these teleconnections is inadequate. Specifically, recent studies have raised concerns regarding the accuracy of climate models in simulating the PARC and resultant limitations of models in simulating Arctic sea ice, the Greenland ice sheet (Hofer et al., 2020; Zelinka et al., 2020), and surface temperature over some parts of the Arctic (Lewis, 2022; Scafetta, 2022). Such known biases may lead to a possible oversensitivity of some models to anthropogenic forcing (J. Zhu et al., 2020). Therefore, efforts should be made to improve the representation of the PARC teleconnection and its interactions with other climate components. While our study provides important insights into the mechanisms underlying long-term climate variability observed in the SNA, further research is necessary to determine how these changes interact with the Arctic climate and the lower-latitude climate system beyond the SNA.

III. A Global Poleward Shift of Atmospheric Rivers

Abstract

Atmospheric rivers (ARs), energized by the baroclinic instability of the mid-latitude mean flow, act as a key agent in transporting poleward moisture and shaping the distribution of extratropical precipitation. While climate models forced by historical anthropogenic forcing suggest an increase in AR activity in the extratropics over the past four decades, this scenario contrasts with observed AR changes during the same period. These observed changes are characterized by a ~6-10º poleward shift during boreal winter in both hemispheres, featuring a rise in AR activity along 50ºN and 50ºS, and a decrease along 30ºN and 30ºS. Here, through a diagnostic analysis of reanalysis data and large ensemble simulations, we demonstrate that low-frequency sea surface temperature variability in the tropical eastern Pacific, exhibiting a cooling tendency since 2000, may play a key role in driving this global AR shift in the extratropics. This shift predominantly occurs over mid-latitude oceans on both sides of the tropics, where strengthening subtropical high pressures maintained by a tropical-driven eddy-mean flow feedback contribute to the observed AR changes. Our findings highlight the sensitivity of ARs to large-scale circulation changes with both internal and external origins, and imply the importance of considering both anthropogenic and natural influences when projecting future AR activity and its associated impacts.

A. Introduction

Accelerating global warming in recent decades has contributed to a pronounced increase in the frequency and severity of extreme weather events globally, including heat waves (Baldwin et al., 2019; Meehl & Tebaldi, 2004; Tripathy et al., 2023), flash droughts (Christian et al., 2021; Yuan et al., 2023), extreme precipitation (Myhre et al., 2019; O'Gorman, 2015; Papalexiou & Montanari, 2019; Tabari, 2020), floods (J. Chen et al., 2023; Musselman et al., 2018), and winter storms (Bengtsson et al., 2009; Eichler et al., 2013; Haarsma et al., 2013). More occurrences of such extremes regulate the hydrological cycle and result in an intensification of hydroclimate extremes and agricultural and ecosystem disasters (Giorgi et al., 2011, 2014; Lesk et al., 2016; Madakumbura et al., 2019). These changes pose diverse threats to human society and call for a closer examination of the underlying mechanisms driving these shifts in extreme precipitation and hydroclimatic patterns.

Anthropogenic forcing is widely recognized to induce a distinct poleward shift of extreme weathers, such as midlatitude/extratropical storms (Bengtsson et al., 2006; Chemke, 2022; Lehmann et al., 2014; Priestley & Catto, 2022; Tamarin & Kaspi, 2017; Tamarin-Brodsky & Kaspi, 2017; Wu et al., 2011; Yin, 2005) and tropical cyclone (Anjana & Kumar, 2023; Sharmila & Walsh, 2018; Studholme et al., 2022; Studholme & Gulev, 2018), particularly in the Southern Hemisphere (SH). Observational and modeling analyses have largely attributed this shift to various mechanisms induced by global warming, including warmer sea surface temperature (SST) (Caballero & Langen, 2005; Graff & LaCasce, 2012; Kodama & Iwasaki, 2009; Lu et al., 2010), and increased atmospheric water vapor (Tamarin & Kaspi, 2016; Tamarin-Brodsky & Kaspi, 2017) on a global scale; increased meridional temperature gradients (Brayshaw et al., 2008; Mbengue & Schneider, 2017; Yin, 2005), enhanced subtropical static stability (Lu et al., 2007, 2010; Staten et al., 2018), and stronger upper-level winds (Tamarin-Brodsky & Kaspi, 2017) over the subtropics; higher tropopause height (Lorenz & DeWeaver, 2007; Lu et al., 2007; Staten et al., 2018) and intensified troposphere heating (Butler et al., 2010) in the tropics. All these mechanisms may reflect various aspects of a similar pattern change that favors a poleward shift of the extratropical jets and related extratropical storms. This shift is also viewed as a key signature of the expansion and weakening of the Hadley circulation (HC) in many studies focusing on hydroclimate response to global warming in the past and future (Anjana & Kumar, 2023; Sharmila & Walsh, 2018; Staten et al., 2018; Studholme et al., 2022; Studholme & Gulev, 2018). However, the dominant underlying mechanism determining long-term changes of midlatitude/extratropical storms over the past decades is still under debate, as observed variability over the past decades was also strongly subject to tropical internal variability, such as the El Niño-Southern Oscillation (ENSO) and the Pacific Decadal Oscillation (PDO) (G. Chen & Held, 2007; Lu et al., 2008; Staten et al., 2018), which are able to significantly regulate the location and strength of midlatitude jets and width of the HC. These independent or interconnected dynamics, originating from both anthropogenic and internal forcing, complicate attribution analyses and emphasize the further need for a better understanding of the causal relationship between different climate drives and responses in extreme weather events sensitive to extratropical storms.

Atmospheric rivers (ARs), belonging to the most extreme weather phenomena associated with the compound junction of strong extratropical storms and large-scale moisture transport, refer to narrow corridors of concentrated moisture in the atmosphere. ARs have significant impacts on extratropical weather extremes (Lamjiri et al., 2017; Ma, Norris, et al., 2020; McGowan et al., 2021; Waliser & Guan, 2017), mid-latitudes poleward moisture transport (Y. Zhu & Newell, 1998), polar moistening (Mattingly et al., 2023; Nash et al., 2018), and various aspects of the extratropical hydrological cycle (Dettinger et al., 2011; Lavers & Villarini, 2015; Viale et al., 2018). Mirroring the observed poleward shift in storm tracks documented by previous studies (Anjana & Kumar, 2023; Chemke, 2022; Chemke et al., 2022; Priestley & Catto, 2022; Studholme et al., 2022; Tamarin-Brodsky & Kaspi, 2017; X. Zhang et al., 2023), a similar and concurrent poleward shift in ARs has been also increasingly discussed (Gao et al., 2016; Ma, Chen, et al., 2020). Previous research on recent changes in ARs predominantly focus on regional variability, such as in the North Atlantic (Gao et al., 2016) and the SH (Ma, Chen, et al., 2020), with these studies primarily attributing these regional shifts to the aforementioned poleward movement of the westerly jet induced by global warming and additional force due to ozone depletion in the SH.

However, a global view of recent AR changes is still lacking, which represents a significant research gap in the community. Given that large-scale circulation changes over the past decades across different regions may be interconnected and share common underlying mechanisms, a comprehensive understanding of ARs' responses to these circulation changes from a global perspective is thus crucial both in the recent past and a future warmer climate. This is particularly important when considering both anthropogenically and naturally-driven factors that usually influence weather activity on a broader spatial scale. This new global perspective is highly needed and essential for accurately predicting ARs and their associated hydrological extremes in the next decades to come. Especially, it has been well discussed that ARs will occur more frequently with higher intensity and heavier precipitation in a warming climate due to increased availability of water vapor and stronger static stability in the atmosphere (Espinoza et al., 2018; Gao et al., 2016; Hagos et al., 2016; Shields et al., 2023; Shields & Kiehl, 2016; L. Zhang et al., 2024). Nevertheless, whether these existing theories, that emphasize enhanced moisture concentration and static stability in the atmosphere, as well as a poleward shift in the westerly jet and storms, can confidently explain all key features of the observed global AR changes and further aid us in projecting ARs in the future still remains an open question, as the complexity of AR dynamics is yet to be fully understood.

In this study, we examine recent global-scale changes in ARs and their roles in shaping climate-weather interactions around mid-latitudes. We aim to understand the underlying mechanisms behind these observed AR changes and identify the potential factors contributing to the performance of climate models in replicating these AR features under different configurations. The overarching goal is to tease apart the relative roles of anthropogenic and natural forcing in shaping the observed changes of ARs over the past decades, and to understand how this knowledge can aid us in improving future global-scale projections of ARs.

B. Methods

B.1 Reanalysis and observation data

The ERA5 reanalysis (Hersbach, Bell, Berrisford, Hirahara, Horányi, Muñoz-Sabater, et al., 2020) is used in this study for atmospheric variables, including geopotential height, horizontal winds (meridional and zonal velocities), omega (vertical velocity), air temperature, and total precipitation spanning the historical period from 1979 to 2022 during the boreal winter (DJF). 6-hourly variables are used for the AR detection algorithm, otherwise monthly variables are used for other analyses. SSTs are obtained from the NOAA Extended Reconstructed Sea Surface Temperature, version 5 (ERSSTv5) (B. Huang et al., 2017) covering the same period and seasons. Monthly means of the vertical integral (from the surface to the top of the atmosphere) of northward water vapor flux (Mayer et al., 2022) are derived from 1-hourly ERA5 reanalysis. Winds used for computation of water vapor flux are mass-adjusted based on the diagnosed imbalance between divergence of vertically integrated dry mass flux and tendency of dry air mass (Mayer et al., 2022).

B.2 Model experiments

We analyze the same variables as those in the reanalysis using the CESM2-LE (Rodgers et al., 2021) 40 members for both historical (1979-2022) and future simulations extending to 2100. These simulations are forced by Coupled Model Intercomparison Project Phase 6 (CMIP6) historical forcing from 1850 to 2014, followed by the Shared Socioeconomic Pathway (SSP) 3-7.0 emissions scenario from 2015 to 2100, with different oceanic and atmospheric initial states for each member. The difference between each member can be used to assess the AR responses to atmospheric or oceanic internal variabilities. In addition, these 40 members are forced by the smoothed CMIP6 biomass burning aerosol forcing.

We also use the pacemaker experiments from CESM2, referred to as PAC. In the PAC simulations, the time-evolving SST anomalies in the eastern tropical Pacific (15ºS to 15ºN, key region of ENSO) are nudged to the ERSSTv5 during 1880 to 2019, with a 5º latitude buffer region to both hemispheres, and the rest of the model’s coupled climate system is set to freely evolve. In this way, the observed SST variability is imposed in the PAC simulations. Time-varying external, natural, and anthropogenic forcings are specified in these ensembles as CESM2-LE. Since these two sets of experiments, CESM2-LE and PAC, share the same model physics/configurations and external forcings, and the ensemble mean of CESM2-LE represents the model’s forced response to anthropogenic forcing, the comparison of the ensemble means of PAC and CESM2-LE can shed light on the role of eastern tropical Pacific SST variability.

Note that the PAC simulations provide only 850 hPa single-layer winds and specific humidity, so we cannot calculate integrated water vapor transport (IVT) across 300-1000 hPa as the AR detection algorithm (Guan & Waliser, 2019) ideally requires. As remedial approach, we use water vapor transport at the single level of 850 hPa (VT850) to approximate the realistic IVT by rescale VT850 to IVT. Given that water vapor transport is strongest at 850 hPa, we believe that this scaling based on VT850 can be used to largely represent changes of 6-hourly IVT. To validate this approach, we calculate the long-term trends of DJF AR frequency in ERA5 using IVT and rescaled VT850 and find no significant differences in their year to year variability (figure not shown) and trends (see Supplementary Fig. III.1).

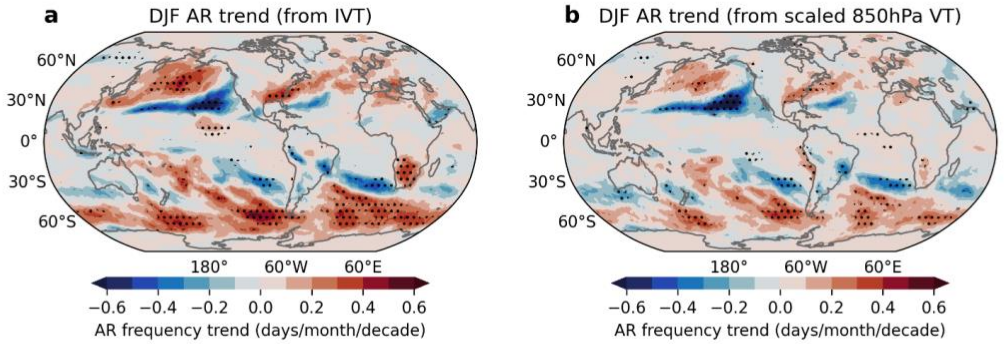

a DJF AR trend (from IVT)

b DJF AR trend (from scaled 850hPa VT)

Supplementary Fig. III.1. Comparison of AR frequency trends using IVT and scaled 850 hPa VT. a&b. The linear trends of DJF AR frequency from ERA5 for the historical period 1979-2022 based on 300-1000 hPa integrated water vapor transport (**a**) and scaled 850hPa single-layer water vapor transport (**b**) in the AR detection algorithm. Black stippling in all plots indicates statistically significant trends at the 95% confidence level.

B.3 AR detection algorithm

An IVT-based detection algorithm developed by Guan and Waliser (Guan & Waliser, 2019) is employed to identify AR on a global scale based on 6-hourly IVT, derived from 6-hourly wind and specific humidity integrated from 1000 to 300 hPa, as $IVT = \frac{1}{g}\int_{1000}^{300} \boldsymbol{u} q dp$, where g is the gravitational acceleration, u is the horizontal winds, and q is the specific humidity.

This AR detection algorithm, recommended by the Atmospheric River Tracking Method Intercomparison Project (ARTMIP) (Shields et al., 2019), has been widely used in the field and considered a reliable algorithm for detecting ARs on a global scale. The algorithm involves multiple criteria to ensure that the identified ARs are long, narrow, and characterized by concentrated moisture transport: 1) intensity threshold: a monthly-dependent 85th percentile of IVT magnitude or 100 kg m-1 s-1, whichever is larger, is used as the intensity threshold at each grid to ensure that the selected AR events are significant; 2) length: the length needs to be longer than 2000 km; 3) length-to-width ratio: the length-to-width is greater than 2; Other criteria, such as the meridional component of mean IVT, the mean transport direction, and coherence, are also applied in the detection algorithm and can be found in this ref. (Guan & Waliser, 2019). In this study, the monthly AR frequency is calculated by integrating the daily occurrences of ARs within each month, expressed as the number of AR days per month.

B.4 Budget of the eddy momentum flux

Considering the zonal mean wind equation and following the approach (Hartmann, 2007):

$$\frac{\partial \bar{u}}{\partial t} = f\bar{v} - \frac{\partial}{\partial y}(\overline{u'v'}) - \alpha\bar{u} \qquad (1)$$

where $f\bar{v}$ indicates the Coriolis term which describes a westerly acceleration caused by the poleward motion, $-\frac{\partial}{\partial y}(u'v')$ is the eddy flux divergence term, representing the meridional divergence of the eddy momentum flux and quantifying how the covariance between the poleward and eastward eddy velocities contributes to the redistribution of momentum in the atmosphere, and $-\alpha\bar{u}$ is the frictional drag term with a drag coefficient α. The eddy meridional flux of zonal momentum $(u'v')$ is calculated following the equation:

$u'v' = (u - u_z)(v - v_z)$, where u and v are daily zonal and meridional winds at each grid point, and u_z and v_z are zonal averages of daily zonal and meridional winds. In this study, we calculate DJF average eddy momentum flux using daily zonal and meridional winds from ERA5 at various vertical levels.

B.5 Fingerprint pattern matching analysis

To examine the role of internal variability beyond anthropogenic effects on AR activity, 40 simulations from CESM2-LE are used in this study. Given that these members share the same CESM2 model physics and are subjected to the same external and anthropogenic forcing, the spread among 40 members – stemming from slightly different oceanic and atmospheric initial conditions – allows us to assess the impact of non-anthropogenic forcing on AR changes.

To disentangle the relative contributions of internal variability versus anthropogenic forcing in deriving AR activity in the model, we analyze the spatial correlation between the observed 44-year long-term trends in DJF AR frequency and those of each CESM2-LE member, as a criterion to identify two distinct groups within the ensemble: one consists of 6 members with high correlation coefficients (>85th percentile of ascending sorted spatial corrections), indicating a strong agreement with observed trends; another consists of 6 members (<15th percentile) with low correction coefficients, suggesting a poor agreement. This classification is based on a selection criterion of one standard deviation within 40-member ensemble, with 6 members assigned to each group.

The key to our investigation lies in comparing the trends in Z200 and SST between these two groups. By examining differences in these trends, we aim to discern clear patterns that could indicate the underlying mechanisms driving the disparities in the long-term AR changes between the groups. Specifically, if the differences between the high-correlation and low-correlation groups reveal well-structured spatial patterns in Z200 or SST trends, it suggests that these variables play an important role in modulating AR activity. Such insights are crucial for understanding the complex interplay between external forcing and internal variability in shaping the long-term AR changes.

B.6 Statistics analysis

The MCA (Bretherton et al., 1992), a powerful statistical method based on singular value decomposition, is employed extensively in this study to detect dominant covarying patterns between large-scale atmospheric circulation and AR frequency. MCA can isolate pairs of spatial patterns and their corresponding time series by conducting a singular vector decomposition on the temporal covariance matrix of two different fields. This process identifies linear functions of the two variables that exhibit the most pronounced relationship. A key metric in this analysis is the squared covariance fraction (SCF), which quantifies the proportion of squared covariance explained by each mode to the total covariance between the two fields. This measure is used to identify the leading and subsequent modes and their significance in overall variability.

In this study, MCA is applied to DJF Z200 and AR frequency on a global scale for the historical period 1979 to 2022. The derived time series from MCA is then correlated with SST to illustrate its relationship with SST. Through these analyses, we aim to understand the coupling between large-scale atmospheric circulation and AR changes, and their relationships with SST, which can provide supports to explain the underlying complex mechanisms modulating AR activity.

We use the effective sample size ($N^* = N\,\frac{1-r_1r_2}{1+r_1r_2}$, N: the total available time steps; r_1&r_2: the lag-one autocorrelation coefficients of each variable) to determine the significance of correlations with the confidence level of 95%, as black stippling in most of our figures when the significance of results need to be considered.

C. Results

C.1 Observed and simulated poleward shift of ARs

In the past few decades, the long-term trends of AR frequency have exhibited a clear well-organized global pattern in boreal winter, while showing more complex regional variability in other seasons (Supplementary Fig. III.2). Thus, this study mainly focuses on understanding the global long-term changes and underlying mechanisms of ARs in December-January-February (DJF). We also find that the mechanism driving the global AR frequency trend pattern in DJF may also exert similar impacts in March-April-May (MAM), which is briefly discussed in the last section. Notably, the annual mean trend of AR frequency also resembles the trends observed in DJF and MAM to some extent, indicating the dominance of these two seasons in shaping annual mean variability.

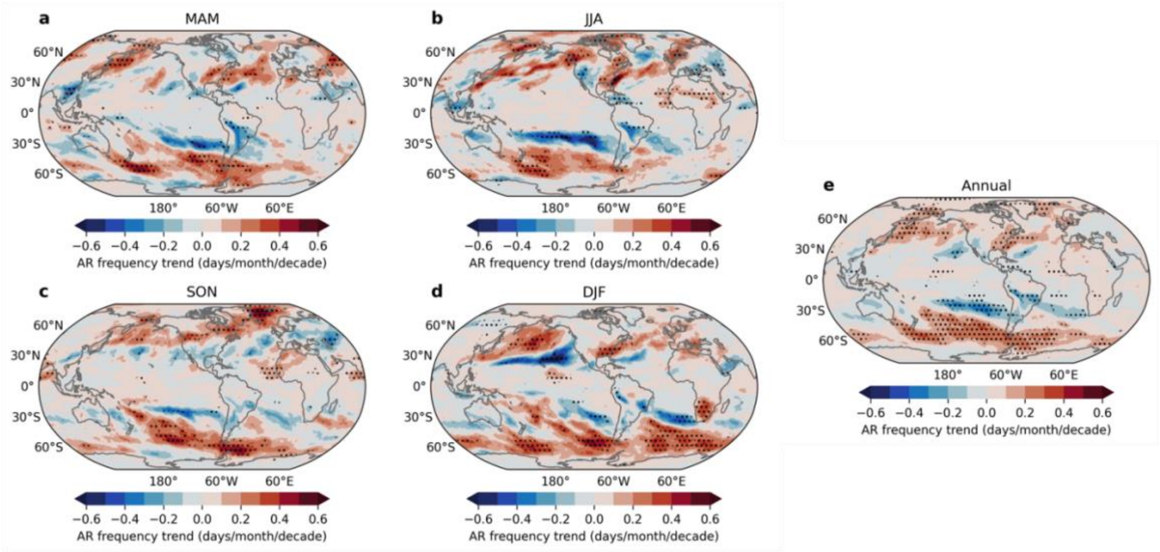

Supplementary Fig. III.2. Observed seasonal and annual trends of AR frequency. a-d. The linear trends of AR frequency from ERA5 for the historical period 1979-2022 across different seasons: boreal Spring (March-April-May, MAM, **a**), Summer (June-July-August, JJA, **b**), Fall (September-October-November, SON, **c**), Winter (December-January-February, DJF, **d**), and the annual mean (**e**). Black stippling in all plots indicates statistically significant trends at the 95% confidence level.

An increase in DJF AR frequency is particularly significant along the 50-60º latitudes in both hemispheres (up to 0.59 days/month/decade), including the North Atlantic and Pacific Oceans, as well as the entire Southern Ocean (Fig. III.1a&b). In contrast, the subtropics along the 30º latitudes of both hemispheres, especially in the Pacific Ocean, have experienced a decrease in DJF AR frequency. The larger increase in AR frequency occurs on the poleward flank of its climatological peak region, while the strong decrease is observed within this peak region (Fig. III.1b). This dipole pattern suggests a global-scale poleward shift of active DJF AR frequency regimes by approximately 10º over recent four decades. Correspondingly, positive trends in AR frequency over the extratropics have led to similar trends in total precipitation and northward moisture transport during the same period (Supplementary Fig. III.3). This is particularly evident over the North and South Pacific Oceans, where the strong increase in AR frequency causes heightened precipitation and transports more moisture poleward in the regions, potentially extending into the Arctic region through the Bering Sea (around 180ºE). Concurrently, DJF geopotential height at the tropopause at 200 hPa (Z200) rises mostly along the subtropics in both hemispheres, with successive isolated barotropic high-pressure centers emerging over the North Pacific (Fig. III.1d). The polar regions also display a contrasting polarity, with a rise in the Arctic and a decrease in the Antarctic (Fig. III.1d), possibly due to Arctic Amplification and the ozone depleting effect in their respective regions. DJF SST trends exhibit significant warming almost everywhere, except for slight cooling of around -0.2ºC per decade in the eastern Pacific and Southern Oceans (Fig. III.1f).

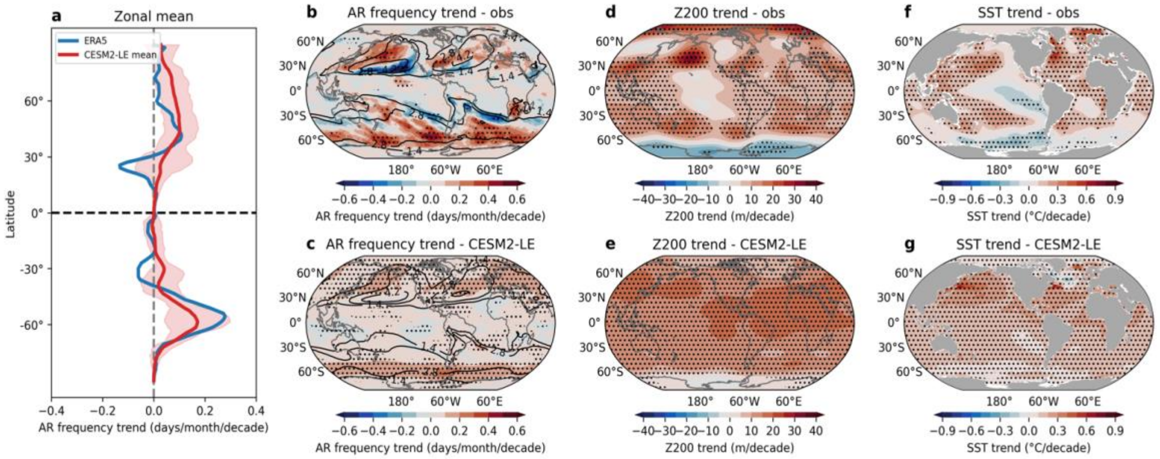

Fig. III.1. Observed and simulated historical trend patterns of AR frequency, Z200, and SST. a. The zonal mean of DJF AR frequency trends from ERA5 (blue line) and CESM2-LE ensemble mean (red line) for the historical period 1979-2022. The red shading in **a** indicates the 5th and 95th percentile of the CESM2-LE members. **b&c**. The linear trends of DJF AR frequency from ERA5 (**b**) and CESM2-LE ensemble mean (**c**) for the historical period 1979-2022. **d&e**. Same as **b&c** but for DJF Z200 from ERA5 (**d**) and CESM2-LE ensemble mean (**e**). **f&g**. Same as **b&c** but for DJF SST from ERSSTv5 (**f**) and CESM2-LE ensemble mean (**g**). Black stippling in all plots indicates statistically significant trends at the 95% confidence level.

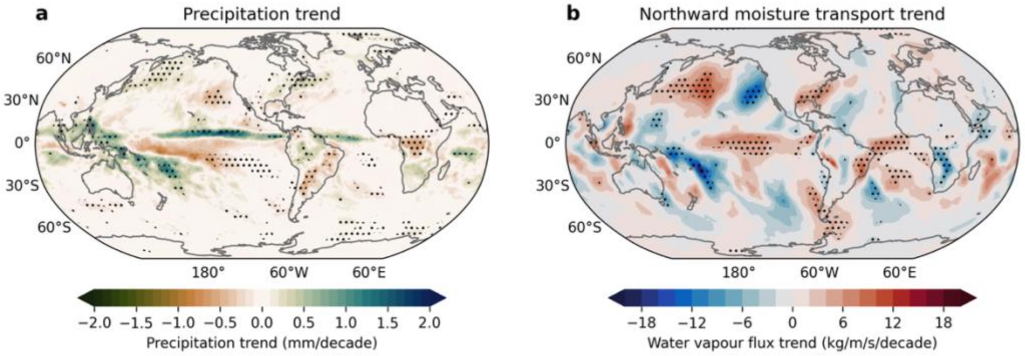

Supplementary Fig. III.3. Historical trends of precipitation and northward moisture transport in ERA5. a&b. The linear trends of DJF total precipitation (**a**) and northward moisture transport (**b**) from ERA5 for the historical period 1979-2022. Black stippling in all plots indicates statistically significant trends at the 95% confidence level.

Compared to observed AR activity in ERA5 (Fig. III.1b), the Community Earth System Model v2 Large Ensemble (CESM2-LE) shows a more moderate increasing trend (up to 0.24 days/month/decade) in AR frequency at high latitudes in both hemispheres (Fig. III.1c). While the ensemble mean from CESM2-LE, representing forced trends driven by anthropogenic forcing, fails to capture the significant negative trend signals observed in the subtropics along 30ºN and 30ºS, some individual ensemble members do better in reflecting this change (Fig. III.1a&c). This discrepancy between the observation and simulation is also evident in the area-weighted global average DJF AR frequency, where CESM2-LE favors an overall increasing trend, while ERA5 shows significant interdecadal variability with a decreasing trend from 1979 to 2013, followed by an abrupt increase in recent 10 years (Supplementary Fig. III.4a). ERA5 indicates a decreasing trend in tropical average AR frequency, while CESM2-LE shows no trend; yet both exhibit an increasing trend in extratropical AR frequency (Supplementary Fig. III.4b&c).

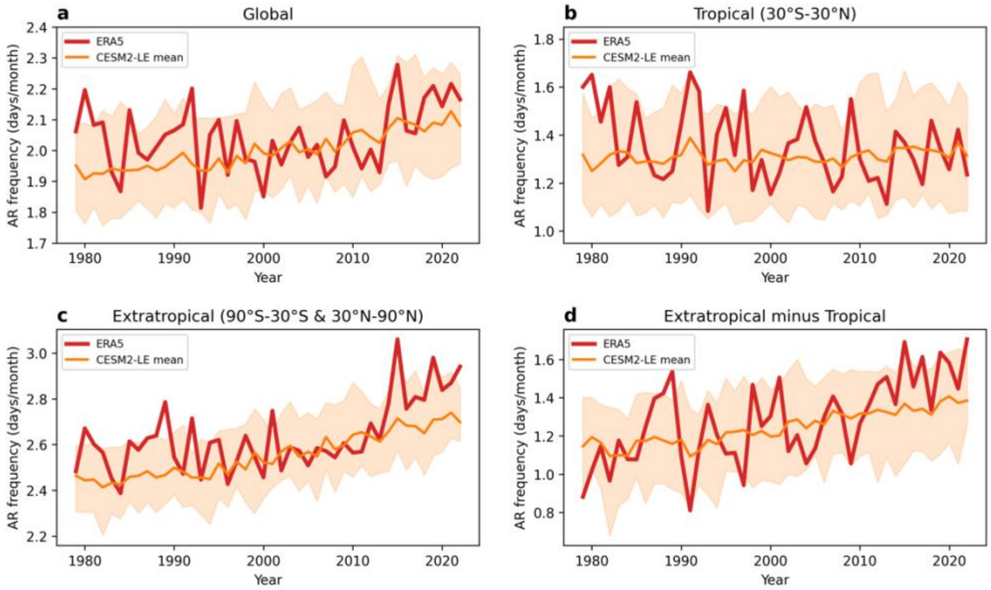

Supplementary Fig. III.4. **Temporal trends of AR frequency in different regions in ERA5 and CESM2-LE**. **a-c**. The weighted average of DJF AR frequency from ERA5 (red line) and CESM2-LE (orange line) in the global (**a**), tropical (30°S-30°N, **b**), and extratropical (90°S-30°S & 30°N-90°N, **c**) regions for the historical period 1979-2022. **d**. The difference between time series of DJF AR frequency weighted average over the extratropical and tropical regions. The orange shadings in the subplots indicate the 5th and 95th percentile of the CESM2-LE members.

Moreover, the observed latitude of maximum zonally averaged AR frequency shifts poleward by about 6º in the Northern Hemisphere (NH) (last 5 years mean: 33º - first 5 years: 27º) and about 10º in the SH (last 5 years mean: -51º - first 5 years: -40.5º) over the past four decades, while CESM2-LE mean shows nearly no shift in the NH and about 4º in the SH (last 5 years mean: -48º - first 5 years: -44º) (Supplementary Fig. III.5a&c). This shift in ERA5 also features an apparent poleward movement of the core AR frequency region (>4.2 days/month; defined as the 85th percentile of maximum DJF AR frequency of a 44-year mean in ERA5) in recent decades in the SH and North Pacific, and a significant expansion of this core region in recent years, nearly doubling the core domain compared to the 1980s (Supplementary Fig. III.5b&d). In contrast, CESM2-LE shows a contrasting pattern with only a slight expansion of the core AR region in the North Atlantic and Southern Oceans and no apparent poleward shift. Overall, the forced response in the model features a rise of ARs in the high latitudes without a decrease in the lower latitudes, differing from the observed poleward shift characterized by an out-of-phase change between 30ºN and 50ºN (or 30ºS and 50ºS). The differences between the observation and CESM2-LE, along with the spread among model members, suggest that additional factors beyond global warming play an important role in driving the observed global poleward shift of ARs.

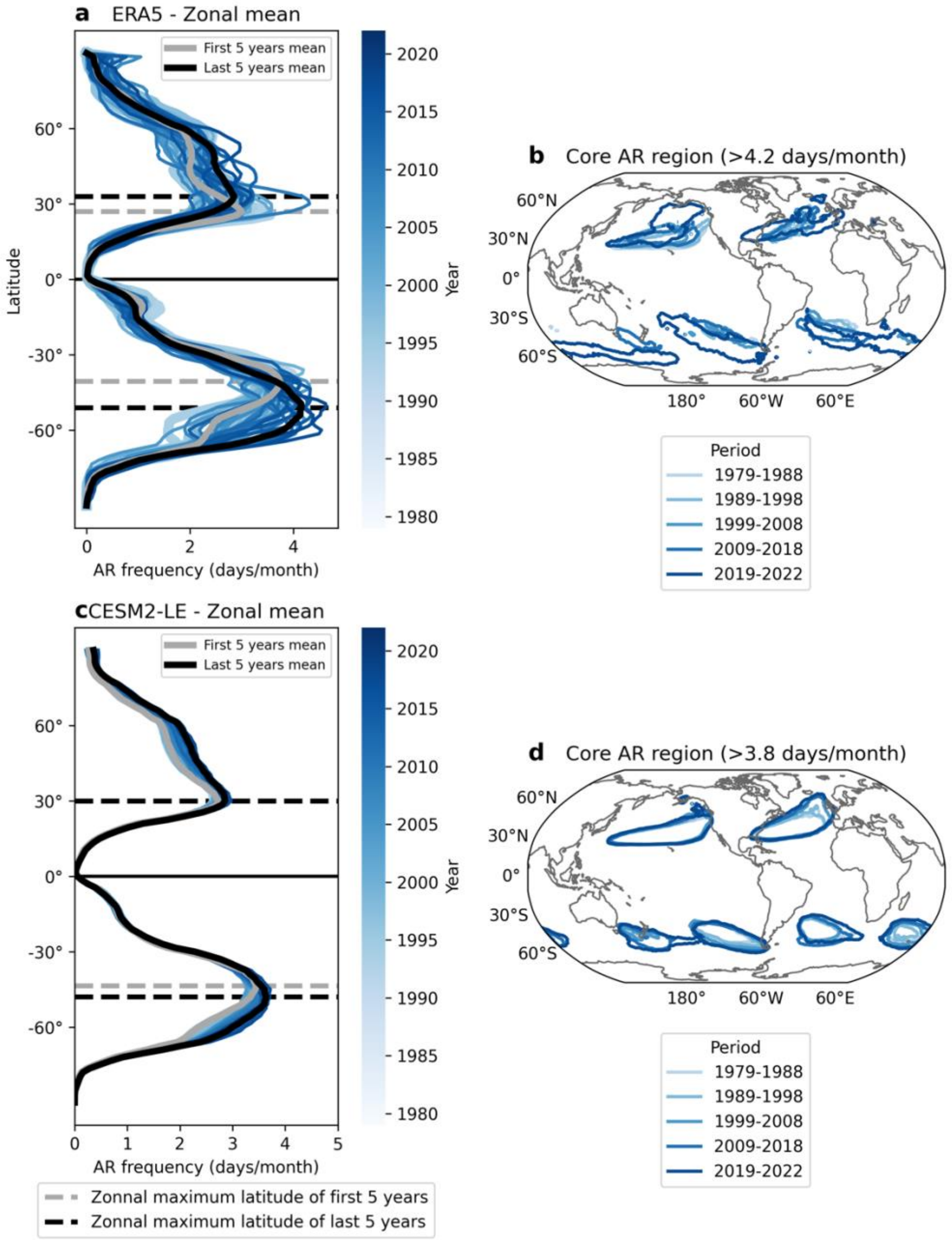

Supplementary Fig. III.5. **Poleward shift of AR frequency zonal mean and core region in ERA5 and CESM2-LE**. **a&c**. The zonal mean of DJF AR frequency from ERA5 (**a**) and CESM2-LE ensemble mean (**c**) each year from 1979 to 2022 with lines from light blue to dark blue. The gray and black bolded curves in the subplots are zonal mean of the DJF AR frequency of the first five years 1979-1983 mean and the last five years 2018-2022 mean, respectively. The gray and black horizonal dashed lines indicate the zonal maximum latitudes of the first five years 1979-1983 mean and the last five years 2018-2022 mean, respectively. **b&d**. The core region of DJF AR frequency from ERA5 (**b**, >4.2 days/month - the threshold defined as the 85th percentile of maximum DJF AR frequency of 44-year mean) and CESM2-LE ensemble mean (**d**, >3.8 days/month – the threshold adjusted due to lower mean state of AR frequency in CESM2-LE) from 1979 to 2022 with 10-year intervals of contours.

Similarly, the comparison of Z200 between ERA5 and CESM2-LE reveals distinct patterns: CESM2-LE ensemble mean shows a rather uniform global increase (Fig. III.1e), while ERA5 displays spatial heterogeneities with stronger increasing trends in the subtropics, weaker trends in the tropics, and decreasing trends in the tropical Pacific (Fig. III.1d). This observed large-scale circulation trend in ERA5 features a clear cold SST anomaly-driven Gill pattern response in the tropical Pacific and an apparent wavy structure in the extratropics (Fig. III.1d&f). However, CESM2-LE does not replicate this negative diabatic heating-driven response in the tropics and the wavy structure of large-scale circulation outside the tropics (Fig. III.1e&g). The pattern of AR frequency trend in ERA5 shows a striking similarity to the observed changes in large-scale circulation and SST, indicating the importance of circulation variability in modulating global decadal variability of ARs, potentially due to the impact of anomalous diabatic heating related to tropical Pacific SST cooling anomalies. These indicate that more attention should be devoted to better understand the relationship between large-scale circulation and ARs, which is key to identifying why models may fall short in accurately replicating observed AR frequency trends (Fig. III.1b).

C.2 Statistical relationship between atmospheric circulation and AR frequency

To statistically investigate the coherent patterns between large-scale atmospheric circulation and ARs, we apply the maximum covariance analysis (MCA) method to detrended Z200 and AR frequency from 1979 to 2022 during boreal winter (see Methods). The first MCA mode (MCA1) accounts for 43% of the covariance fraction and is shown in Figure III.2a-c. The spatial pattern of AR frequency in MCA1 predominantly shows positive signals in the extratropics, particularly over the North Pacific, and a tilted positive band extending from the tropics to the subtropics in the Southern Ocean (Fig. III.2a). This pattern largely resembles the observed DJF AR frequency trend (Fig. III.1b), although it lacks some positive signals in the Southern Ocean. The MCA1 Z200 pattern displays a tropical-driven Pacific-North American (PNA) and Pacific-South America (PSA) global teleconnection pattern, with a Gill response over the eastern tropical Pacific (Fig. III.2b). This Z200-AR mode is highly correlated to DJF SST, marked by negative signals in the eastern Pacific Ocean and positive signals in the subtropics on both sides of the Pacific Ocean (Supplementary Fig. III.6a). This correlation pattern aligns with the observed long-term trend of DJF SST, especially in the Pacific Ocean (Fig. III.1f), suggesting that the long-term trends in Z200, SST, and AR are closely interconnected, and their connections may stem from the tropical-driven teleconnection reflected by MCA1.

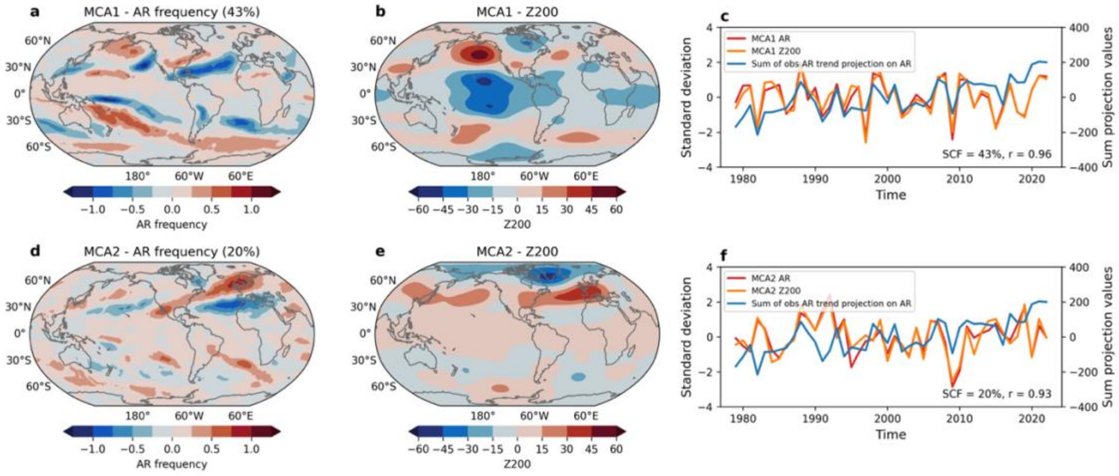

Fig. III.2. Observed statistical relationship between detrended Z200 and AR frequency using MCA. **a-c**, Results of the leading MCA mode (MCA1) of detrended global DJF AR frequency and Z200 from ERA5 for the historical period 1979-2022, with spatial patterns of AR frequency (**a**) and Z200 (**b**), and their corresponding standardized time series (**c**). The time series of the sum of raw AR frequency projection on long-term AR frequency trend from ERA5 is also shown in **c**. **d-f**, Same as **a-c** but for results of the second MCA mode (MCA2) of two variables. 'SCF' in **c** and **f** indicates the squared covariance fraction of the MCA mode, and 'r' in **c** and **f** indicates the correlation coefficient between the MCA mode time series. The linear trends of DJF AR frequency and Z200 are removed (detrended) for the MCA.

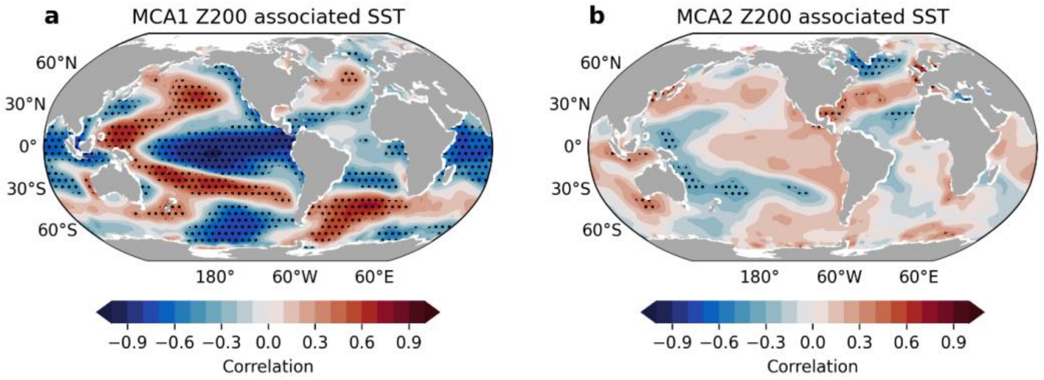

Supplementary Fig. III.6. **MCA Z200 time series associated SST patterns. a&b.** The correlation of spatial DJF SST with MCA1 Z200 time series (**a**) and MCA2 Z200 time series (**b**). All linear trends are removed in calculating correlations. Black stippling in all plots indicates statistically significant correlations at the 95% confidence level.

The second MCA mode (MCA2) explains 20% of the covariance and its spatial patterns feature a coupling of the two fields in and around the Arctic. The AR frequency pattern in MCA2 is characterized by positive signals in the North Atlantic and North Pacific, and negative signals along 30ºN (Fig. III.2d). This pattern contributes to the observed increasing trend in AR frequency in the North Atlantic and North Pacific, that is less captured in the MCA1 results. MCA2 Z200 is dominated by a prominent Arctic Oscillation variability, with negative signals above Greenland and positive signals in the NH subtropics (Fig. III.2e), and is highly related to cooling SST in the subpolar North Atlantic (Supplementary Fig. III.6b). When this mode is in its positive phase, a strong mid-latitude jet stream with high pressures steers ARs northward, while in its negative phase, a weaker and more meandering jet dips farther south, causing ARs to shift equatorward.

Moreover, the MCA over the past 44 years using raw data shows results similar to those of the detrended MCA (Supplementary Fig. III.7). These suggest that the Z200-AR connection is robust on both interannual and interdecadal timescales over the past decades and the observed long-term changes of Z200 and AR frequency may reflect a low frequency variation of the interannual AR-Z200 connection, as shown in Fig. III.2a&b.

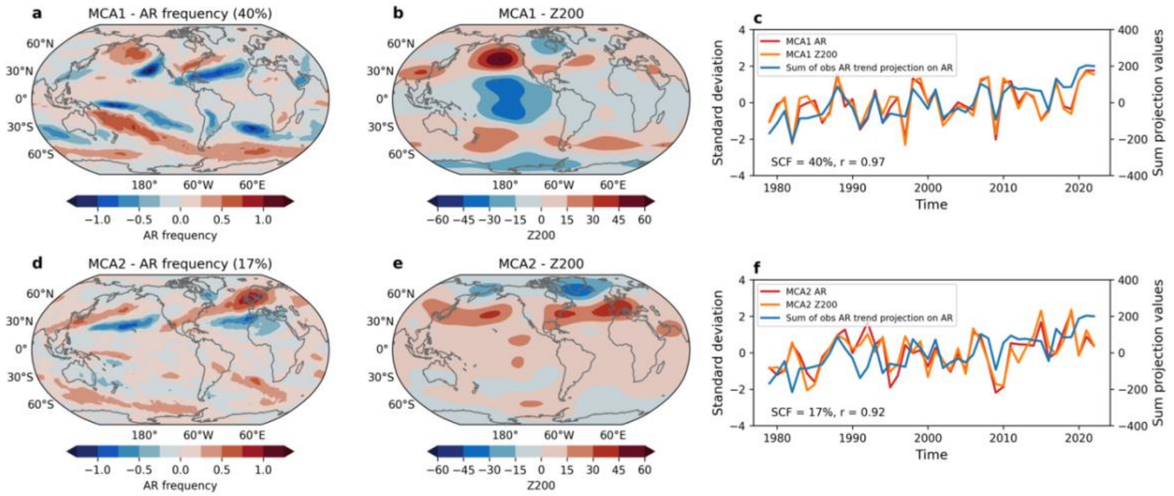

Supplementary Fig. III.7. **Observed statistical relationship between Z200 and AR frequency using MCA (raw, with trend). a-c**, Results of the leading MCA mode (MCA1) of global AR frequency and Z200 from ERA5 for the historical period 1979-2022 during boreal winter (raw, with trend), with spatial patterns of AR frequency (**a**) and Z200 (**b**), and their corresponding standardized time series (**c**). The time series of the sum of raw AR frequency projection on long-term AR frequency trend from ERA5 is also shown in **c**. **d-f**, Same as **a-c** but for results of the second MCA mode (MCA2) of two variables. 'SCF' in **c** and **f** indicates the squared covariance fraction of the MCA mode, and 'r' in **c** and **f** indicates the correlation coefficient between the MCA mode time series.

To further quantify which MCA AR patterns mostly capture the observed long-term trends of ARs, we project the DJF AR frequency anomalies for each year onto the spatial pattern of long-term DJF AR frequency trend. Through this calculation, a 44-year time series can be obtained by globally summing the projected spatial values in each DJF. By design, this time series (the blue curve in Fig. III.2c&f) displays a clear upward trend over the period, indicating a gradual enhancement of the AR trend signal over time. The correlations of this projected time series with MCA1&2 AR time series inform us which MCA mode is more critical in explaining the raw AR variability on a global scale. This newly constructed time series exhibits a significant correlation with the detrended MCA1 AR time series (Fig. III.2c), with a correlation coefficient of 0.73 (detrended) on interannual timescales. This indicates that the majority of the observed long-term changes in ARs can be well explained by the MCA1 AR-Z200 coupling mode. Although the time series of MCA2 AR shows a weaker association (r=0.17, detrended) with the observed AR trend projection time series (Fig. III.2f), this mode still accounts for some aspects of AR changes in the North Atlantic and North Pacific. If we redo this calculation by focusing on the NH, MCA2 appears to be important in capturing the observed AR trends in the NH (r=0.48, detrended).

C.3 Eddy-mean flow contribution to ARs poleward shift

The underlying reason for a circumglobal height rise along the NH and SH subtropics in tandem with tropical SST cooling in the eastern tropical Pacific over the past four decades remains to be fully explored (Fig. III.1d&f). Given the significant role of eddy-mean flow feedback in regulating zonal mean flow variability (Hartmann, 2007; Seager et al., 2014), we place more attention on its role in maintaining the long-term Z200 trend in this section.

To better illustrate this idea, we calculate the past 44-year long-term trends of DJF northward eddy momentum flux and its meridional convergence/divergence (see Methods). It is clearly seen that the significant trend of northward eddy momentum flux aligns well with the height rise over both subtropics, which also shifts slightly poleward to the maximum action center of the climatological eddy momentum fluxes (Fig. III.3a&d). The strengthened divergence and convergence of eddy momentum flux appear around 25ºN and 45ºN, respectively, which favor enhanced zonal mean southerly and northly winds over the same regions (Fig. III.3b). These winds converge over ~35ºN and consequently induce a sinking motion and adiabatic warming from the surface to ~300 hPa (Fig. III.3b&c). Thus, the entire air column around 30-40ºN is adiabatically warmed and experiences a rise in the height field with the maximum rise at ~300 hPa. A similar pattern occurs over the SH subtropics around 40-50ºS, but with slightly weaker intensity.

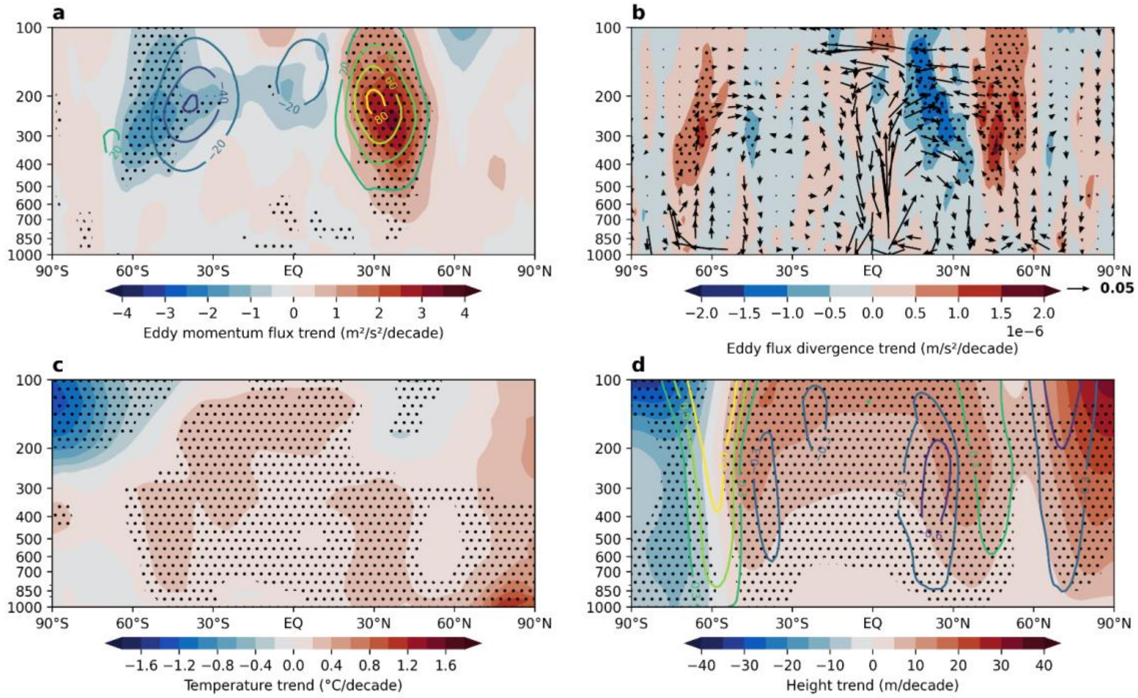

Fig. III.3. Observed trends in zonal average eddy momentum flux, circulation, temperature, and winds. **a**. The linear trend (shading) and 44-year mean (contour) of DJF zonal average eddy meridional flux of zonal momentum. **b**. The linear trends of DJF zonal average eddy meridional flux convergence/divergence of zonal momentum (shading) and the composite of vertical velocity (ω·-50; Pa/s) and meridional velocity (m/s) (vectors). **c**. The liner trend of DJF zonal average air temperature. **d**. The linear trends of DJF zonal average geopotential height (shading) and zonal winds (contour). All calculations are based on the historical period 1979-2022 from ERA5. Black stippling in all plots indicates statistically significant trends at the 95% confidence level.

This is consistent with the well-established mechanism explaining the tandem changes of tropical SST forcing and height rise in the extratropics (Diaz et al., 2001; Ding & Wang, 2005; Mo & Livezey, 1986; Trenberth et al., 1998; Yang et al., 2022). This line of thought studies suggests that eastern tropical Pacific SST cooling, similar to the La Niña conditions or the negative phase of the PDO, favors an expansion of the tropical belt due to stronger tropical waves arising from a stronger Walker circulation over the tropical western Pacific. This effect alters the features of subtropical storms and diverts them from their usual action zones due to various mechanisms (Lu et al., 2008; Seager et al., 2003).The shift in storm tracks modifies the zonal mean eddy momentum flux as shown in Figure 3 and induces high-pressure anomalies along both subtropics.

These high-pressure anomalies, with anticyclonic wind anomalies, particularly over the extratropical oceans, result in a shift pattern of AR activity with an increase of AR frequency on the northern side of the subtropics and a decrease on the tropical flank. Although ENSO-related wave trains on both hemispheres (PNA and PSA) may imprint some zonal mean signals along the subtropics, the main component of the zonal mean pattern is believed to be driven by aforementioned eddy mean-flow feedback, which plays a key role in linking tropical forcing to the poleward shift of ARs.

C.4 Fingerprint analysis detecting roles of circulation and SST in regulating ARs

Considering the inferred role of tropical SST forcing in driving ARs activity via the eddy-mean flow feedback, we expect that simulations with observed tropical forcing imposed should more accurately replicate observed AR trends than those without such tropical forcing added. To test this hypothesis, we use 40 ensemble members from CESM2-LE, which provide 6-hourly data for AR detection (see Methods). These members are differentiated by their initial conditions, allowing us to access the different AR behaviors among members and the extent to which they are impacted by the aforementioned tropical forcing.

Although the ensemble mean of CESM2-LE does not fully capture the observed poleward shift of ARs, certain individual members exhibit patterns that resemble the observed trends to some level (Supplementary Fig. III.8). The difference among these members suggests that internal variability can partially contribute to the observed poleward shift of ARs over the past decades. To better reveal the role of internal variability (or tropical forcing) in the observed changes of ARs, we employ a fingerprint pattern matching analysis using the 40 members of CESM2-LE. We identify two groups performing very differently in simulating the observed long-term trends of DJF AR frequency over the same period: a ‘top group’ comprising six members that show the highest spatial correlation with the observed DJF AR frequency trend (see Methods, beyond the 85th percentile of the ascending sorted spatial correlation), and a ‘bottom group’ comprising six members with the most negative spatial correlation (or near zero, below the 15th percentile).

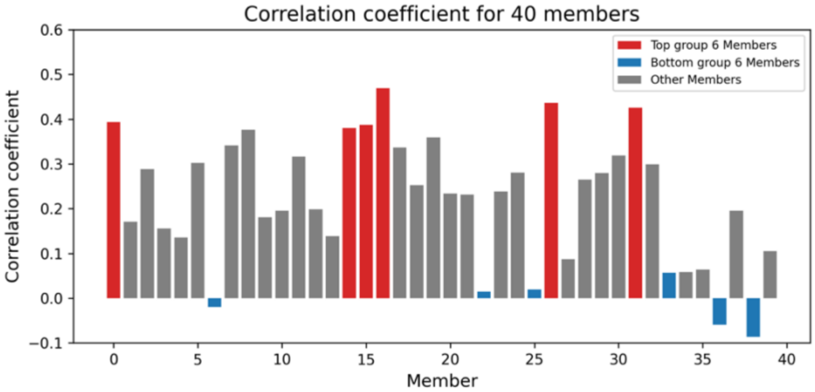

Supplementary Fig. III.8. Comparison of AR frequency trend patterns between the observation and CESM2-LE members. Spatial correlations between DJF AR frequency trends from ERA5 and CESM2-LE 40 members (each) for the historical period 1979-2022.

By design, the DJF AR frequency trend in the top group ensemble features a similar pattern to the observed changes, although it lacks significant trends of AR in the SH subtropics (Fig. III.4a), indicating that when member-to-member diversity is considered, some members can still capture the poleward shift of ARs. In contrast, the bottom group shows sporadic positive trends in the subtropics rather than the observed well-organized positive-negative contrasting pattern (Fig. III.4b). The differences in Z200 and SST trends between these two composites (hereafter ‘top-minus-bottom’) are shown in Figure III.4c&d. Since both groups are subject to anthropogenic forcing, their differences minimize the impact of global warming and mainly represent the influence of internal variability. The most prominent feature in the top-minus-bottom Z200 composite is an isolated high pressure in the North Pacific, with a high pressure band in the Southern Ocean and lower pressure in the tropical

Pacific (Fig. III.4c). This pattern bears a resemblance to the observed DJF Z200 trends (Fig. III.1d), including the contrasting trends between the two polar regions. Similarly, the top-minus-bottom SST composite (Fig. III.4d) favors a similar cooling pattern in the tropical Pacific as observed (Fig. III.1f), and is consistent with the MCA results (Fig. III.2). These results suggest that in the model's world, the observed AR trends are better simulated by certain members that also better replicate observed large-scale circulation and tropical SST variability. This indicates a strong physical constraint of tropical-drive large-scale circulation in shaping the long-term trend of global ARs, independent of anthropogenic forcing.

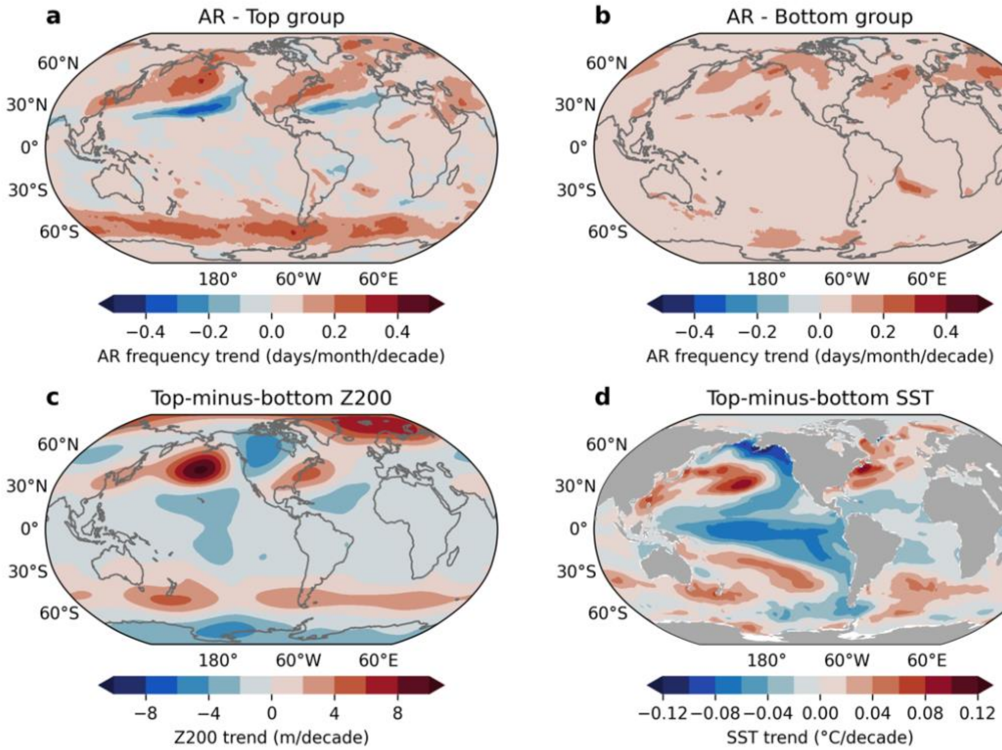

Fig. III.4. Differences in simulated AR frequency trends among CESM2-LE 40 members. **a&b**. The linear trends of DJF AR frequency from the ensemble average of six members in CESM2-LE 40 members that show the greatest similarity to the observed trend pattern of DJF AR frequency (**a**, top group) and the ensemble average of six members that show the weakest similarity to the observed trend pattern of DJF AR frequency (**b**, bottom group) for the historical period 1979-2022. **c&d**. The difference of ensemble averaged DJF Z200 (**c**) and SST (**d**) trends between the top and bottom groups for the historical period 1979-2022. The difference is divided by 2 to reference it to the ensemble mean.

We further examine the pacemaker experiment (PAC), a 10-member ensemble from CESM2, wherein SSTs in the eastern tropical Pacific are nudged to time-varying prescribed SST anomalies derived from ERSSTv5, while remaining fully coupled everywhere else (see Methods). Meanwhile, radiative and anthropogenic forcing is imposed in the PAC ensemble. Thus, the results from PAC reflect CESM2's response to both anthropogenic forcing and observed SST variability originating from the eastern tropical Pacific. DJF AR frequency trends in the PAC ensemble exhibit a poleward shift pattern as observed, with strong positive trends occurring over the North Pacific and extending from the tropics to the subtropics in the Southern Ocean, alongside negative trends in the NH subtropics (Fig. III.5a). Similarly, DJF Z200 in the PAC ensemble shows an observation-like pattern, with negligible increasing trends over the tropical Pacific compared to other regions and two belts of high-pressure wavy activity over the subtropics (Fig. III.5b).

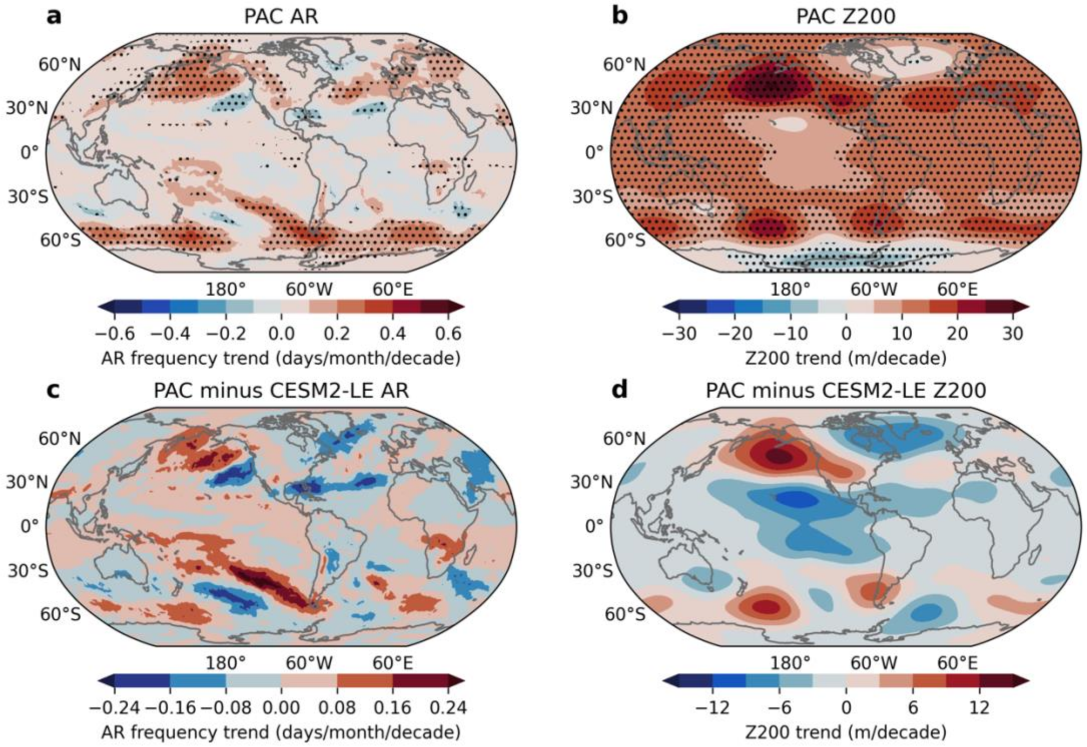

Fig. III.5. Simulated trends in AR frequency and Z200 in PAC simulations. **a-b**. The linear trends of DJF AR frequency (**a**) and Z200 (**b**) from the ensemble mean of PAC simulations for the historical period 1979-2018. **c-d**. The difference of the linear trends of DJF AR frequency (**c**) and Z200 (**d**) between the ensemble mean of PAC and CESM2-LE for the historical period 1979-2018. Black stippling in all plots indicates statistically significant trends at the 95% confidence level.

Since CESM2-LE is forced by the same anthropogenic forcing but without observed tropical Pacific SST forcing, differences between PAC and CESM2-LE simulations may provide insights into CESM2's response solely to observed eastern tropical Pacific SST forcing. The difference in AR frequency trends between PAC and CESM2-LE shows a clear out-of-phase dipole pattern, especially in the NH (Fig. III.5c), which suggests that the model with imposed tropical Pacific SST forcing effectively captures the observed AR changes there. Moreover, the difference in Z200 trends between PAC and CESM2-LE successfully replicates the observed significant negative trends in the tropical Pacific and high-pressure belts along the subtropics, particularly over the North Pacific (Fig. III.5d). However, some Z200 responses in Fig. III.5b still differ from those in the fingerprint analysis (Fig. III.4c) and observation (Fig. III.1d) over parts of the North Atlantic and close to West Antarctic, indicating that 10 members of PAC may not sufficiently reflect a robust response to tropical SST forcing in the model. This inability may also imprint its biased signal on AR in those regions. Even so, these results reinforce the importance of eastern tropical Pacific SST cooling in regulating long-term AR changes with a poleward shift pattern through altering large-scale circulation patterns in most areas of the globe, and this SST-Z200-AR coupling is partially driven by internal variability.

D. Discussion

In this study, we show low-frequency variability of ENSO strengthens subtropical high pressures on both sides of the tropics, exerting a significant impact on an intensification of boreal winter AR frequency in the mid-latitudes along 50-60ºN and 50-60ºS, and a diminish of AR frequency around 30ºN and 30ºS. A tropical eddy-mean flow feedback acts as the key mechanism to maintain the strengthening of the high-pressure anomalies and the resultant poleward shift pattern of ARs. Using state-of-the-art model ensemble and a fingerprint pattern matching method, we further suggest that global climate model simulations may better capture observed AR changes when observed low-frequency SST variability is well simulated, raising a need to close examine their future projections in the tropics and related teleconnections to the extratropics. Thus, our study provides an improved physical understanding of the mechanisms driving the recent global poleward shift of ARs, which can further assist in assessing future projections of weather extremes in a warmer climate.

Contrary to the currently widely accepted view emphasizing on a thermodynamic control of global warming on extreme precipitation via various mechanisms (Emori & Brown, 2005; O'Gorman & Schneider, 2009), our findings suggest that dynamic forcing – often underestimated by climate models – may also play an important role on extreme precipitation in the extratropics through regulating the westerly jets and AR activity. This dynamic component is critical for accurately predicting future extreme weather patterns and may either mask or amplify the signals due to global warming, depending on the phase of the low-frequency component of ENSO. Thus, in order to improve the capability of climate models in projecting future climate extremes, especially in the extratropics, we should ensure that climate models own a reasonable skill to replicate the observed tropical-circulation-AR connection and low-frequency ENSO variability.

Considering the importance of tropical SST variability in shaping global DJF AR changes over the past decades, it is plausible that tropical SST response in the future may still hold some potential to modulate ARs through a similar eddy-mean flow feedback mechanism. Comparing the final 40 years of CESM2-LE projections (2060-2099) under the SSP3-7.0 scenario with the recent four decades reveals a noticeable increase in DJF AR occurrences, extending into mid-latitudes and the Arctic, with frequencies potentially doubling by the century's end, particularly in the SH (Supplementary Fig. III.9a&c). This projected increase in ARs is expected to induce more extreme precipitation events in the extratropics. In addition, it is noted that AR changes between the two epochs exhibit a slight decline in the tropics, although this decline is much weaker than the trends observed over the past four decades. This suggests that even under significant global warming (SSP3-7.0) forcing in CESM2, the climate response in the tropics does not favor a significant long-term decrease in ARs there. Regarding seasonality, future projections for the SH reveal similar trends for JJA and DJF, while in the NH, there is a significant difference between the two seasons. JJA predictions indicate a more pronounced increase in AR activity in the Arctic, whereas DJF predictions exhibit an increase in the extratropics (Supplementary Fig. III.9a&b). This discrepancy suggests a seasonal variation in AR behavior and is likely due to the most pronounced Arctic Amplification in summer. Despite these differences, both seasons demonstrate extensive penetration of ARs into the Arctic, which could significantly impact Arctic moisture concentration and consequent impacts on the cryosphere.

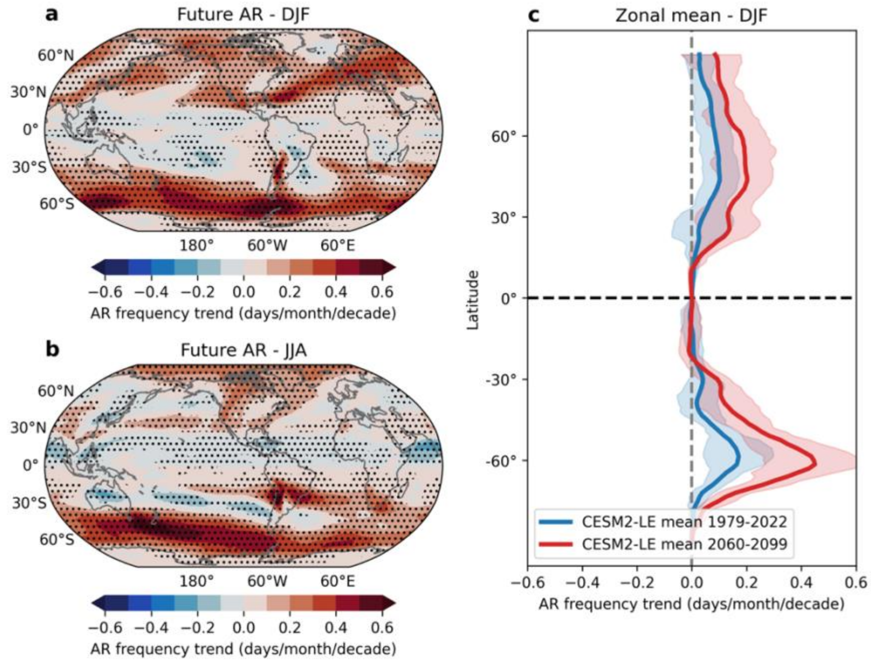

Supplementary Fig. III.9. Projected future trends of AR frequency in CESM2-LE. **a&b**. The linear trends of AR frequency from CESM2-LE ensemble mean in future simulations (2060-2099) under the SSP3-7.0 scenario in boreal winter (DJF, **a**) and boreal summer (JJA, **b**). **c**. The zonal mean of DJF AR frequency trend in CESM2-LE historical simulations (1979-2022, blue line) and future simulations (2060-2099, red line). The blue and red shadings in **c** indicate the 5th and 95th percentile of the CESM2-LE members in historical and future simulations. Black stippling in all plots indicates statistically significant trends at the 95% confidence level.

Since ENSO, usually peaking in DJF, may preferentially exhibit long-term variations during its peak season, it is understandable that the mechanisms identified in this study are most pronounced in boreal winter. To further assess whether the same mechanisms also operate at other times of the year, we extend our investigation to other seasons and find that a similar connection exists in March-April-May (MAM). However, during boreal summer and fall, when ENSO is relatively weak, the identified mechanisms seem to be greatly weakened in their global impact. This weakening may be due to changes in the extratropical basic state that do not favor a strong eddy-mean flow feedback or tropical-extratropical teleconnections emanated from the ENSO region. However, we cannot rule out the possibility that in a warmer world, the seasonal dependence of these impacts may vary, which deserves further attention.

Moreover, some recent studies have suggested that the recent tropical Pacific SST cooling could be attributed to increased aerosol forcing since the 1980s (McMonigal, 2024), which suggests that the mechanisms discussed in this study might be anthropogenically driven by aerosol-induced radiative forcing in the tropics. However, although aerosol forcing is well considered and specified in CESM2-LE, the SST cooling trend pattern suggested by the study is not clearly seen in the ensemble mean response in our analysis. It suggests that it is still premature to attribute the observed SST cooling over the eastern Pacific and related impacts on ARs solely to an anthropogenic origin. It calls for a more thorough future analysis to understand whether the SST cooling pattern is driven by internal processes or external forcing, which may also represent an important source of uncertainty in attributing observed tropical and extratropical variabilities and also in projecting future changes in tropical SST and their related impacts on extratropical ARs.

Conclusions

A. Summary

This dissertation demonstrates that large-scale atmospheric circulation is critical to understanding the recent rapid climate changes observed in high northern latitudes, such as upper ocean temperature variabilities in the Arctic and the North Atlantic, as well as the poleward shift pattern of ARs in the extratropics over the past four decades. Low-frequency atmospheric variability accounts for a substantial portion of the coexistence of the warming Arctic-cooling SNA through several mechanisms, including changes in shortwave radiation absorption, vertical mixing, poleward oceanic heat transport, and the AMOC in the region. Atmospheric teleconnection plays an important role in bridging tropical SST variations to extratropical climate phenomena, which indicates that regional atmosphere-ocean and climate-weather interactions could be remotely forced and may have internal origins. Additionally, low-frequency ENSO variability contributes to strengthening subtropical high pressures and shifting the frequency of ARs poleward, especially in NH extratropics. These findings underscore the need for improved climate model representations of these processes to better predict future atmosphere-ocean interactions and climate extremes. **Overall, this dissertation contributes insight on how large-scale atmospheric circulation shapes upper ocean variability and extreme weather patterns, particularly in high northern latitudes, highlighting the complex interactions between atmospheric and oceanic processes in the region and their teleconnections with the tropics.**

B. Key Results

Chapter I identifies the significant role of low-frequency atmospheric variability, characterized by anomalous anticyclonic circulation over the Arctic Ocean and Greenland, in driving upper Arctic Ocean warming over the past few decades. Using both observational data and modeling analyses, this study quantifies that wind-driven atmospheric variability accounts for up to 24% of the SON upper ocean warming between 1979 to 2018, and up to 60% of the warming from 2000 to 2018. The mechanisms include subsidence and adiabatic warming, which enhance shortwave and longwave radiation absorption and vertical mixing in open water areas, leading to further warming of the ocean mixed layer. The study highlights the importance of accurately replicating internal atmospheric forcing and tropical-Arctic teleconnections in climate models, emphasizing the need for improved model evaluation metrics to better represent Arctic atmosphere-sea ice-ocean coupling.

Chapter II employs various statistical and diagnostic analyses on reanalysis data and climate model results, along with a wind-nudging experiment, to elucidate the mechanisms driving climate variability in the SNA. We find that large-scale atmospheric circulation significantly influences SST, upper ocean heat transport, and AMOC variabilities in the SNA through wind-driven processes operating on both interannual and interdecadal time scales. Anticyclonic high-pressure systems and cyclonic low-pressure systems, accompanied by stronger easterly and westerly winds, contribute to the warming and cooling of the underlying ocean, sea ice melt and expansion around Greenland, and changes in the GrIS mass through driving anomalous Ekman flow and local surface flux exchange. Additionally, this atmospheric process is partially driven by forcing originating from the tropical Pacific through an atmospheric teleconnection. These internally-driven atmospheric processes are important in strengthening high northern latitude atmosphere-ocean interactions, related ocean heat transport, and AMOC, which shape multidecadal climate variability in the North Atlantic. These identified atmosphere-ocean coupling mechanisms, however, are not well captured in the CESM-LE or individual member runs, raising concerns about the models' skill in simulating multidecadal SST variability over the North Atlantic. Given the significant impact of these mechanisms on local and remote climates, this chapter emphasizes the need for a thorough understanding of the complex interplay between atmospheric processes, the upper ocean, and the cryosphere. Moreover, the diverse performance of CMIP6 models in replicating observed SST changes in the SNA suggests that further efforts are needed to assess the sources of individual model biases in simulating the key physical processes related to observed atmosphere-ocean coupling and its remote connection to tropics.

Chapter III shows that low-frequency ENSO variability strengthens subtropical high pressures on both sides of the tropics, significantly impacting AR frequency by intensifying their occurrence in mid-latitudes (50-60°N and 50-60°S) and reducing their frequency around 30°N and 30°S. We identify a tropical eddy-mean flow feedback as a key mechanism maintaining the high-pressure anomalies and resulting in the poleward shift pattern of ARs. Using state-of-the-art model ensembles and a fingerprint pattern matching method, this chapter suggests that climate models can better capture observed AR changes when they accurately simulate low-frequency SST variability, raising the need to closely examine future projections in the tropics and related tropical-extratropical teleconnections. This chapter illuminates the importance of dynamic forcing in AR activity and extreme precipitation, advocating for enhanced climate model capabilities to replicate tropical-circulation-AR connections, which is crucial for accurately predicting future climate extremes, particularly in the NH extratropics.

C. Future work

This dissertation provides a comprehensive understanding of the role of large-scale atmospheric circulation in shaping upper ocean temperature variabilities in the Arctic and North Atlantic, as well as the poleward shift pattern of ARs in high northern latitudes and even in the globe-scale. Despite these advancements, several questions remain, highlighting the need for ongoing research to refine our understanding and improve future climate projections. Future studies should aim to enhance the representation of atmospheric and oceanic interactions within climate models, with a particular focus on capturing the dynamics of high northern latitudes climate variability. It is also essential to further explore the implications of these atmospheric patterns on future climate scenarios and their potential to intensify extreme weather conditions. Future and ongoing research efforts include the following:

1. Improve the representation of internal atmospheric forcing and tropical-Arctic teleconnections to enhance the accuracy of climate models in simulating observed variability in the Arctic Ocean’s upper layer warming. This includes refining nudging experiments and developing better metrics to evaluate current climate models’ ability to replicate lead-lag relationships between atmospheric and oceanic variables.
2. Investigate the role of deeper ocean circulation and heat transport from sub-Arctic regions in influencing the Arctic ocean’s heat balance. This involves examining the effects of water mass exchanges between the Arctic and Atlantic/Pacific Oceans, as

well as processes like brine rejection and Atlantification on ocean stratification and vertical mixing. As suggested in Chapter I, further work could focus on the impact of subsurface warm Atlantic Waters on the mass balance of Greenland glaciers and the broader implications for regional climate variability. Studying the transport mechanisms of these deeper warm waters and their interactions with large-scale atmospheric circulation could potentially improve future projection of glacier dynamics and sea level rise. Understanding these deeper ocean processes may provide insights into other contributions to surface temperature changes and sea ice dynamics that may be important.

3. Improve understanding of cross-basin teleconnections, particularly the influence of the tropical Pacific on the North Atlantic and Arctic. The framework developed in Chapter II could be applied as metrics to evaluate current climate models' skill in replicating local atmosphere-ocean interactions in the SNA and their teleconnection patterns, and address the limitations of models in simulating the PARC and its effects on high northern latitudes oceans.
4. Continue to assess the role of dynamics forcing in AR activity and extreme precipitation events, and evaluate whether current climate models accurately replicate the tropical-circulation-AR connection and low-frequency ENSO variability. Refine models to better capture these dynamics atmospheric processes can improve the accuracy of future climate projections, particularly in predicting extreme weather patterns in the extratropics.
5. As suggested in Chapter III, conducting more studies on future climate scenarios, particularly under high-emission pathways, is necessary to understand potential

changes in AR frequency and intensity in a warming climate. Additionally, exploring the impacts of AR penetration into the Arctic on moisture concentration and the cryosphere in the future, and assessing how seasonal changes influence ARs and related extreme precipitation events, will provide valuable insights into how these phenomena contribute to climate extremes and climate-weather interactions in a warming climate.

References

Amory, C., Trouvilliez, A., Gallée, H., Favier, V., Naaim-Bouvet, F., Genthon, C., Agosta, C., Piard, L., & Bellot, H. (2015). Comparison between observed and simulated aeolian snow mass fluxes in Adélie Land, East Antarctica. *The Cryosphere*, *9*(4), 1373–1383. https://doi.org/10.5194/tc-9-1373-2015

Anjana, U., & Kumar, K. K. (2023). New insights into the poleward migration of tropical cyclones and its association with Hadley circulation. *Scientific Reports*, *13*(1), Article 1. https://doi.org/10.1038/s41598-023-42323-7

Årthun, M., Eldevik, T., & Smedsrud, L. H. (2019). The Role of Atlantic Heat Transport in Future Arctic Winter Sea Ice Loss. *Journal of Climate*, *32*(11), 3327–3341. https://doi.org/10.1175/JCLI-D-18-0750.1

Baldwin, J. W., Dessy, J. B., Vecchi, G. A., & Oppenheimer, M. (2019). Temporally Compound Heat Wave Events and Global Warming: An Emerging Hazard. *Earth's Future*, *7*(4), 411–427. https://doi.org/10.1029/2018EF000989

Ballinger, T. J., Hanna, E., Hall, R. J., Miller, J., Ribergaard, M. H., & Høyer, J. L. (2018). Greenland coastal air temperatures linked to Baffin Bay and Greenland Sea ice conditions during autumn through regional blocking patterns. *Climate Dynamics*, *50*(1), 83–100. https://doi.org/10.1007/s00382-017-3583-3

Ballinger, T. J., Moore, G. W. K., Garcia-Quintana, Y., Myers, P. G., Imrit, A. A., Topál, D., & Meier, W. N. (2022). Abrupt Northern Baffin Bay Autumn Warming and Sea-Ice Loss Since the Turn of the Twenty-First Century. *Geophysical Research Letters*, *49*(21), e2022GL101472. https://doi.org/10.1029/2022GL101472

Banzon, V., Smith, T. M., Steele, M., Huang, B., & Zhang, H.-M. (2020). Improved Estimation of Proxy Sea Surface Temperature in the Arctic. *Journal of Atmospheric and Oceanic Technology*, *37*(2), 341–349. https://doi.org/10.1175/JTECH-D-19-0177.1

Baxter, I., Ding, Q., Schweiger, A., L'Heureux, M., Baxter, S., Wang, T., Zhang, Q., Harnos, K., Markle, B., Topal, D., & Lu, J. (2019). How Tropical Pacific Surface Cooling Contributed to Accelerated Sea Ice Melt from 2007 to 2012 as Ice Is Thinned by Anthropogenic Forcing. *Journal of Climate*, *32*(24), 8583–8602. https://doi.org/10.1175/JCLI-D-18-0783.1

Beer, E., Eisenman, I., & Wagner, T. J. W. (2020). Polar Amplification Due to Enhanced Heat Flux Across the Halocline. *Geophysical Research Letters*, *47*(4), e2019GL086706. https://doi.org/10.1029/2019GL086706e2019GL086706. https://doi.org/10.1029/2019GL086706

Bengtsson, L., Hodges, K. I., & Keenlyside, N. (2009). Will Extratropical Storms Intensify in a Warmer Climate? *Journal of Climate*, *22*(9), 2276–2301. https://doi.org/10.1175/2008JCLI2678.1

Bengtsson, L., Hodges, K. I., & Roeckner, E. (2006). Storm Tracks and Climate Change. *Journal of Climate*, *19*(15), 3518–3543. https://doi.org/10.1175/JCLI3815.1

Bevis, M., Harig, C., Khan, S. A., Brown, A., Simons, F. J., Willis, M., Fettweis, X., van den Broeke, M. R., Madsen, F. B., Kendrick, E., Caccamise, D. J., van Dam, T., Knudsen, P., & Nylen, T. (2019). Accelerating changes in ice mass within Greenland, and the ice sheet's sensitivity to atmospheric forcing. *Proceedings of the*

National Academy of Sciences, *116*(6), 1934–1939. https://doi.org/10.1073/pnas.1806562116

Boers, N. (2021). Observation-based early-warning signals for a collapse of the Atlantic Meridional Overturning Circulation. *Nature Climate Change*, *11*(8), Article 8. https://doi.org/10.1038/s41558-021-01097-4

Bonan, D. B., & Blanchard-Wrigglesworth, E. (2020). Nonstationary Teleconnection Between the Pacific Ocean and Arctic Sea Ice. *Geophysical Research Letters*, *47*(2), e2019GL085666. https://doi.org/10.1029/2019GL085666

Booth, B. B. B., Dunstone, N. J., Halloran, P. R., Andrews, T., & Bellouin, N. (2012). Aerosols implicated as a prime driver of twentieth-century North Atlantic climate variability. *Nature*, *484*(7393), Article 7393. https://doi.org/10.1038/nature10946

Boyer, T., Baranova, O., Locarnini, R., Mishonov, A., Grodsky, A., Paver, C., Weathers, K., Smolyar, I., Reagan, J., Seidov, D., & Zweng, M. (2019). *WORLD OCEAN ATLAS 2018 Product Documentation Ocean Climate Laboratory NCEI / NESDIS / NOAA NOAA National Centers for Environmental Information*. https://doi.org/10.13140/RG.2.2.34758.01602

Brayshaw, D. J., Hoskins, B., & Blackburn, M. (2008). The Storm-Track Response to Idealized SST Perturbations in an Aquaplanet GCM. *Journal of the Atmospheric Sciences*, *65*(9), 2842–2860. https://doi.org/10.1175/2008JAS2657.1

Bretherton, C. S., Smith, C., & Wallace, J. M. (1992). An Intercomparison of Methods for Finding Coupled Patterns in Climate Data. *Journal of Climate*, *5*(6), 541–560. https://doi.org/10.1175/1520-0442(1992)005<0541:AIOMFF>2.0.CO;2

Bretherton, C. S., Widmann, M., Dymnikov, V. P., Wallace, J. M., & Bladé, I. (1999). The Effective Number of Spatial Degrees of Freedom of a Time-Varying Field. *Journal of Climate*, *12*(7), 1990–2009. https://doi.org/10.1175/1520-0442(1999)012<1990:TENOSD>2.0.CO;2

Butler, A. H., Thompson, D. W. J., & Heikes, R. (2010). The Steady-State Atmospheric Circulation Response to Climate Change–like Thermal Forcings in a Simple General Circulation Model. *Journal of Climate*, *23*(13), 3474–3496. https://doi.org/10.1175/2010JCLI3228.1

Caballero, R., & Langen, P. L. (2005). The dynamic range of poleward energy transport in an atmospheric general circulation model. *Geophysical Research Letters*, *32*(2). https://doi.org/10.1029/2004GL021581

Cabanes, C., Lee, T., & Fu, L.-L. (2008). Mechanisms of Interannual Variations of the Meridional Overturning Circulation of the North Atlantic Ocean. *Journal of Physical Oceanography*, *38*(2), 467–480. https://doi.org/10.1175/2007JPO3726.1

Caesar, L., Rahmstorf, S., Robinson, A., Feulner, G., & Saba, V. (2018). Observed fingerprint of a weakening Atlantic Ocean overturning circulation. *Nature*, *556*(7700), Article 7700. https://doi.org/10.1038/s41586-018-0006-5

Carmack, E., Polyakov, I., Padman, L., Fer, I., Hunke, E., Hutchings, J., Jackson, J., Kelley, D., Kwok, R., Layton, C., Melling, H., Perovich, D., Persson, O., Ruddick, B., Timmermans, M.-L., Toole, J., Ross, T., Vavrus, S., & Winsor, P. (2015). Toward Quantifying the Increasing Role of Oceanic Heat in Sea Ice Loss in the New Arctic. *Bulletin of the American Meteorological Society*, *96*(12), 2079–2105. https://doi.org/10.1175/BAMS-D-13-00177.1

Carton, J. A., Chepurin, G. A., & Chen, L. (2018). SODA3: A New Ocean Climate Reanalysis. *Journal of Climate*, *31*(17), 6967–6983. https://doi.org/10.1175/JCLI-D-18-0149.1

Carton, J. A., Penny, S. G., & Kalnay, E. (2019). Temperature and Salinity Variability in the SODA3, ECCO4r3, and ORAS5 Ocean Reanalyses, 1993–2015. *Journal of Climate*, *32*(8), 2277–2293. https://doi.org/10.1175/JCLI-D-18-0605.1

Cavalieri, Donald, Parkinson, Claire, Gloersen, Per, & Zwally, H. Jay. (1996). *Sea Ice Concentrations from Nimbus-7 SMMR and DMSP SSM/I-SSMIS Passive Microwave Data, Version 1* [dataset]. NASA National Snow and Ice Data Center DAAC. https://doi.org/10.5067/8GQ8LZQVL0VL

Chemke, R. (2022). The future poleward shift of Southern Hemisphere summer mid-latitude storm tracks stems from ocean coupling. *Nature Communications*, *13*(1), Article 1. https://doi.org/10.1038/s41467-022-29392-4

Chemke, R., Ming, Y., & Yuval, J. (2022). The intensification of winter mid-latitude storm tracks in the Southern Hemisphere. *Nature Climate Change*, *12*(6), Article 6. https://doi.org/10.1038/s41558-022-01368-8

Chemke, R., Zanna, L., & Polvani, L. M. (2020). Identifying a human signal in the North Atlantic warming hole. *Nature Communications*, *11*(1), Article 1. https://doi.org/10.1038/s41467-020-15285-x

Chen, G., & Held, I. M. (2007). Phase speed spectra and the recent poleward shift of Southern Hemisphere surface westerlies. *Geophysical Research Letters*, *34*(21). https://doi.org/10.1029/2007GL031200

Chen, J., Shi, X., Gu, L., Wu, G., Su, T., Wang, H.-M., Kim, J.-S., Zhang, L., & Xiong, L. (2023). Impacts of climate warming on global floods and their implication to current flood defense standards. *Journal of Hydrology, 618*, 129236. https://doi.org/10.1016/j.jhydrol.2023.129236

Chen, X., & Tung, K.-K. (2018). Global surface warming enhanced by weak Atlantic overturning circulation. *Nature*, *559*(7714), Article 7714. https://doi.org/10.1038/s41586-018-0320-y

Christian, J. I., Basara, J. B., Hunt, E. D., Otkin, J. A., Furtado, J. C., Mishra, V., Xiao, X., & Randall, R. M. (2021). Global distribution, trends, and drivers of flash drought occurrence. *Nature Communications, 12*(1), 6330. https://doi.org/10.1038/s41467-021-26692-z

Chung, E.-S., Ha, K.-J., Timmermann, A., Stuecker, M. F., Bodai, T., & Lee, S.-K. (2021). Cold-Season Arctic Amplification Driven by Arctic Ocean-Mediated Seasonal Energy Transfer. *Earth's Future*, *9*(2), e2020EF001898. https://doi.org/10.1029/2020EF001898

Cohen, J., Screen, J. A., Furtado, J. C., Barlow, M., Whittleston, D., Coumou, D., Francis, J., Dethloff, K., Entekhabi, D., Overland, J., & Jones, J. (2014). Recent Arctic amplification and extreme mid-latitude weather. *Nature Geoscience*, *7*(9), Article 9. https://doi.org/10.1038/ngeo2234

Mayer, J., Mayer, M., & Haimberger, L. (2022). *Mass-consistent atmospheric energy and moisture budget monthly data from 1979 to present derived from ERA5 reanalysis*. [accessed March 2024]. https://doi.org/10.24381/CDS.C2451F6B

Dai, A., Luo, D., Song, M., & Liu, J. (2019). Arctic amplification is caused by sea-ice loss under increasing CO2. *Nature Communications*, *10*(1), 121. https://doi.org/10.1038/s41467-018-07954-9

Danabasoglu, G., Lamarque, J.-F., Bacmeister, J., Bailey, D. A., DuVivier, A. K., Edwards, J., Emmons, L. K., Fasullo, J., Garcia, R., Gettelman, A., Hannay, C., Holland, M. M., Large, W. G., Lauritzen, P. H., Lawrence, D. M., Lenaerts, J. T. M., Lindsay, K., Lipscomb, W. H., Mills, M. J., … Strand, W. G. (2020). The Community Earth System Model Version 2 (CESM2). *Journal of Advances in Modeling Earth Systems*, *12*(2), e2019MS001916. https://doi.org/10.1029/2019MS001916

Danielson, S. L., Weingartner, T. J., Hedstrom, K. S., Aagaard, K., Woodgate, R., Curchitser, E., & Stabeno, P. J. (2014). Coupled wind-forced controls of the Bering–Chukchi shelf circulation and the Bering Strait throughflow: Ekman transport, continental shelf waves, and variations of the Pacific–Arctic sea surface height gradient. *Progress in Oceanography*, *125*, 40–61. https://doi.org/10.1016/j.pocean.2014.04.006

Dee, D. P., Uppala, S. M., Simmons, A. J., Berrisford, P., Poli, P., Kobayashi, S., Andrae, U., Balmaseda, M. A., Balsamo, G., Bauer, P., Bechtold, P., Beljaars, A. C. M., Berg, L. van de, Bidlot, J., Bormann, N., Delsol, C., Dragani, R., Fuentes, M., Geer, A. J., … Vitart, F. (2011). The ERA-Interim reanalysis: Configuration and performance of the data assimilation system. *Quarterly Journal of the Royal Meteorological Society*, *137*(656), 553–597. https://doi.org/10.1002/qj.828

Delworth, T. L., & Knutson, T. R. (2000). Simulation of Early 20th Century Global Warming. *Science*, *287*(5461), 2246–2250. https://doi.org/10.1126/science.287.5461.2246

Desbiolles, F., Bentamy, A., Blanke, B., Roy, C., Mestas-Nuñez, A. M., Grodsky, S. A., Herbette, S., Cambon, G., & Maes, C. (2017). Two decades [1992–2012] of surface wind analyses based on satellite scatterometer observations. *Journal of Marine Systems*, *168*, 38–56. https://doi.org/10.1016/j.jmarsys.2017.01.003

Dettinger, M. D., Ralph, F. M., Das, T., Neiman, P. J., & Cayan, D. R. (2011). Atmospheric Rivers, Floods and the Water Resources of California. *Water*, *3*(2), Article 2. https://doi.org/10.3390/w3020445

Diaz, H. F., Hoerling, M. P., & Eischeid, J. K. (2001). ENSO variability, teleconnections and climate change. *International Journal of Climatology*, *21*(15), 1845–1862. https://doi.org/10.1002/joc.631

Ding, Q., Schweiger, A., L’Heureux, M., Steig, E. J., Battisti, D. S., Johnson, N. C., Blanchard-Wrigglesworth, E., Po-Chedley, S., Zhang, Q., Harnos, K., Bushuk, M., Markle, B., & Baxter, I. (2019). Fingerprints of internal drivers of Arctic sea ice loss in observations and model simulations. *Nature Geoscience*, *12*(1), Article 1. https://doi.org/10.1038/s41561-018-0256-8

Ding, Q., Wallace, J. M., Battisti, D. S., Steig, E. J., Gallant, A. J. E., Kim, H.-J., & Geng, L. (2014). Tropical forcing of the recent rapid Arctic warming in northeastern Canada and Greenland. *Nature*, *509*(7499), Article 7499. https://doi.org/10.1038/nature13260

Ding, Q., & Wang, B. (2005). Circumglobal Teleconnection in the Northern Hemisphere Summer. *Journal of Climate*, *18*(17), 3483–3505. https://doi.org/10.1175/JCLI3473.1

Ditlevsen, P., & Ditlevsen, S. (2023). Warning of a forthcoming collapse of the Atlantic meridional overturning circulation. *Nature Communications*, *14*(1), Article 1. https://doi.org/10.1038/s41467-023-39810-w

Drijfhout, S., Oldenborgh, G. J. van, & Cimatoribus, A. (2012). Is a Decline of AMOC Causing the Warming Hole above the North Atlantic in Observed and Modeled Warming Patterns? *Journal of Climate*, *25*(24), 8373–8379. https://doi.org/10.1175/JCLI-D-12-00490.1 8373–8379. https://doi.org/10.1175/JCLI-D-12-00490.1

Eichler, T. P., Gaggini, N., & Pan, Z. (2013). Impacts of global warming on Northern Hemisphere winter storm tracks in the CMIP5 model suite. *Journal of Geophysical Research: Atmospheres*, *118*(10), 3919–3932. https://doi.org/10.1002/jgrd.50286

Emori, S., & Brown, S. J. (2005). Dynamic and thermodynamic changes in mean and extreme precipitation under changed climate. *Geophysical Research Letters*, *32*(17). https://doi.org/10.1029/2005GL023272

England, M. R., Eisenman, I., Lutsko, N. J., & Wagner, T. J. W. (2021). The Recent Emergence of Arctic Amplification. *Geophysical Research Letters*, *48*(15), e2021GL094086. https://doi.org/10.1029/2021GL094086

England, M. R., Polvani, L. M., Sun, L., & Deser, C. (2020). Tropical climate responses to projected Arctic and Antarctic sea-ice loss. *Nature Geoscience*, *13*(4), Article 4. https://doi.org/10.1038/s41561-020-0546-9

Espinoza, V., Waliser, D. E., Guan, B., Lavers, D. A., & Ralph, F. M. (2018). Global Analysis of Climate Change Projection Effects on Atmospheric Rivers. *Geophysical Research Letters*, *45*(9), 4299–4308. https://doi.org/10.1029/2017GL076968

Eyring, V., Bony, S., Meehl, G. A., Senior, C. A., Stevens, B., Stouffer, R. J., & Taylor, K. E. (2016). Overview of the Coupled Model Intercomparison Project Phase 6 (CMIP6) experimental design and organization. *Geoscientific Model Development*, *9*(5), 1937–1958. https://doi.org/10.5194/gmd-9-1937-2016

Feng, X., Ding, Q., Wu, L., Jones, C., Baxter, I., Tardif, R., Stevenson, S., Emile-Geay, J., Mitchell, J., Carvalho, L. M. V., Wang, H., & Steig, E. J. (2021). A Multidecadal-Scale Tropically Driven Global Teleconnection over the Past Millennium and Its Recent Strengthening. *Journal of Climate*, *34*(7), 2549–2565. https://doi.org/10.1175/JCLI-D-20-0216.1

Fetterer, F. (2017). *Sea Ice Index, Version 3 (G02135)*. National Snow and Ice Data Center. https://nsidc.org/data/g02135/versions/3

Fettweis, X. (2007). Reconstruction of the 1979–2006 Greenland ice sheet surface mass balance using the regional climate model MAR. *The Cryosphere*, *1*(1), 21–40. https://doi.org/10.5194/tc-1-21-2007

Fettweis, X., Box, J. E., Agosta, C., Amory, C., Kittel, C., Lang, C., van As, D., Machguth, H., & Gallée, H. (2017). Reconstructions of the 1900–2015 Greenland ice sheet surface mass balance using the regional climate MAR model. *The Cryosphere*, *11*(2), 1015–1033. https://doi.org/10.5194/tc-11-1015-2017

Fettweis, X., Tedesco, M., van den Broeke, M., & Ettema, J. (2011). Melting trends over the Greenland ice sheet (1958–2009) from spaceborne microwave data and regional climate models. *The Cryosphere*, *5*(2), 359–375. https://doi.org/10.5194/tc-5-359-2011

Franco, B., Fettweis, X., Lang, C., & Erpicum, M. (2012). Impact of spatial resolution on the modelling of the Greenland ice sheet surface mass balance between 1990–2010, using the regional climate model MAR. *The Cryosphere*, *6*(3), 695–711. https://doi.org/10.5194/tc-6-695-2012

Fyfe, J. C., von Salzen, K., Gillett, N. P., Arora, V. K., Flato, G. M., & McConnell, J. R. (2013). One hundred years of Arctic surface temperature variation due to anthropogenic influence. *Scientific Reports*, *3*(1), Article 1. https://doi.org/10.1038/srep02645

Gallée, H., & Schayes, G. (1994). Development of a Three-Dimensional Meso-γ Primitive Equation Model: Katabatic Winds Simulation in the Area of Terra Nova Bay, Antarctica. *Monthly Weather Review*, *122*(4), 671–685. https://doi.org/10.1175/1520-0493(1994)122<0671:DOATDM>2.0.CO;2

Gao, Y., Lu, J., & Leung, L. R. (2016). Uncertainties in Projecting Future Changes in Atmospheric Rivers and Their Impacts on Heavy Precipitation over Europe. *Journal of Climate*, *29*(18), 6711–6726. https://doi.org/10.1175/JCLI-D-16-0088.1

Germe, A., Houssais, M.-N., Herbaut, C., & Cassou, C. (2011). Greenland Sea sea ice variability over 1979–2007 and its link to the surface atmosphere. *Journal of Geophysical Research: Oceans*, *116*(C10). https://doi.org/10.1029/2011JC006960

Gervais, M., Shaman, J., & Kushnir, Y. (2018). Mechanisms Governing the Development of the North Atlantic Warming Hole in the CESM-LE Future Climate Simulations. *Journal of Climate*, *31*(15), 5927–5946. https://doi.org/10.1175/JCLI-D-17-0635.1

Gill, A. E. (1980). Some simple solutions for heat-induced tropical circulation. *Quarterly Journal of the Royal Meteorological Society*, *106*(449), 447–462. https://doi.org/10.1002/qj.49710644905

Giorgi, F., Coppola, E., & Raffaele, F. (2014). A consistent picture of the hydroclimatic response to global warming from multiple indices: Models and observations. *Journal of Geophysical Research: Atmospheres*, *119*(20), 11,695-11,708. https://doi.org/10.1002/2014JD022238

Giorgi, F., Im, E.-S., Coppola, E., Diffenbaugh, N. S., Gao, X. J., Mariotti, L., & Shi, Y. (2011). Higher Hydroclimatic Intensity with Global Warming. *Journal of Climate*, *24*(20), 5309–5324. https://doi.org/10.1175/2011JCLI3979.1

Graff, L. S., & LaCasce, J. H. (2012). Changes in the Extratropical Storm Tracks in Response to Changes in SST in an AGCM. *Journal of Climate*, *25*(6), 1854–1870. https://doi.org/10.1175/JCLI-D-11-00174.1

Guan, B., & Waliser, D. E. (2019). Tracking Atmospheric Rivers Globally: Spatial Distributions and Temporal Evolution of Life Cycle Characteristics. *Journal of Geophysical Research: Atmospheres*, *124*(23), 12523–12552. https://doi.org/10.1029/2019JD031205

Haarsma, R. J., Hazeleger, W., Severijns, C., de Vries, H., Sterl, A., Bintanja, R., van Oldenborgh, G. J., & van den Brink, H. W. (2013). More hurricanes to hit western Europe due to global warming. *Geophysical Research Letters*, *40*(9), 1783–1788. https://doi.org/10.1002/grl.50360

Hagos, S. M., Leung, L. R., Yoon, J.-H., Lu, J., & Gao, Y. (2016). A projection of changes in landfalling atmospheric river frequency and extreme precipitation over western

North America from the Large Ensemble CESM simulations. *Geophysical Research Letters*, *43*(3), 1357–1363. https://doi.org/10.1002/2015GL067392

Hanna, E., Cappelen, J., Fettweis, X., Mernild, S. H., Mote, T. L., Mottram, R., Steffen, K., Ballinger, T. J., & Hall, R. J. (2021). Greenland surface air temperature changes from 1981 to 2019 and implications for ice-sheet melt and mass-balance change. *International Journal of Climatology*, *41*(S1), E1336–E1352. https://doi.org/10.1002/joc.6771

Hanna, E., Cropper, T. E., Hall, R. J., & Cappelen, J. (2016). Greenland Blocking Index 1851–2015: A regional climate change signal. *International Journal of Climatology*, *36*(15), 4847–4861. https://doi.org/10.1002/joc.4673

Hanna, E., Fettweis, X., & Hall, R. J. (2018). Brief communication: Recent changes in summer Greenland blocking captured by none of the CMIP5 models. *The Cryosphere*, *12*(10), 3287–3292. https://doi.org/10.5194/tc-12-3287-2018

Hansen, J., Ruedy, R., Sato, M., & Lo, K. (2010). Global Surface Temperature Change. *Reviews of Geophysics*, *48*(4). https://doi.org/10.1029/2010RG000345

Hartmann, D. L. (2007). The Atmospheric General Circulation and Its Variability. *Journal of the Meteorological Society of Japan. Ser. II*, *85B*, 123–143. https://doi.org/10.2151/jmsj.85B.123

He, C., Clement, A. C., Cane, M. A., Murphy, L. N., Klavans, J. M., & Fenske, T. M. (2022). A North Atlantic Warming Hole Without Ocean Circulation. *Geophysical Research Letters*, *49*(19), e2022GL100420. https://doi.org/10.1029/2022GL100420

Hegerl, G. C., Hasselmann, K., Cubasch, U., Mitchell, J. F. B., Roeckner, E., Voss, R., & Waszkewitz, J. (1997). Multi-fingerprint detection and attribution analysis of greenhouse gas, greenhouse gas-plus-aerosol and solar forced climate change. *Climate Dynamics*, *13*(9), 613–634. https://doi.org/10.1007/s003820050186

Hersbach, H., Bell, B., Berrisford, P., Hirahara, S., Horányi, A., Muñoz-Sabater, J., Nicolas, J., Peubey, C., Radu, R., Schepers, D., Simmons, A., Soci, C., Abdalla, S., Abellan, X., Balsamo, G., Bechtold, P., Biavati, G., Bidlot, J., Bonavita, M., … Thépaut, J.-N. (2020). The ERA5 global reanalysis. *Quarterly Journal of the Royal Meteorological Society*, *146*(730), 1999–2049. https://doi.org/10.1002/qj.3803

Hofer, S., Lang, C., Amory, C., Kittel, C., Delhasse, A., Tedstone, A., & Fettweis, X. (2020). Greater Greenland Ice Sheet contribution to global sea level rise in CMIP6. *Nature Communications*, *11*(1), Article 1. https://doi.org/10.1038/s41467-020-20011-8

Holland, D. M., Thomas, R. H., de Young, B., Ribergaard, M. H., & Lyberth, B. (2008). Acceleration of Jakobshavn Isbræ triggered by warm subsurface ocean waters. *Nature Geoscience*, *1*(10), Article 10. https://doi.org/10.1038/ngeo316

Hu, S., & Fedorov, A. V. (2020). Indian Ocean warming as a driver of the North Atlantic warming hole. *Nature Communications*, *11*(1), Article 1. https://doi.org/10.1038/s41467-020-18522-5https://doi.org/10.1038/s41467-020-18522-5

Huang, B., Thorne, P. W., Banzon, V. F., Boyer, T., Chepurin, G., Lawrimore, J. H., Menne, M. J., Smith, T. M., Vose, R. S., & Zhang, H.-M. (2017). Extended Reconstructed Sea Surface Temperature, Version 5 (ERSSTv5): Upgrades, Validations, and Intercomparisons. *Journal of Climate*, *30*(20), 8179–8205. https://doi.org/10.1175/JCLI-D-16-0836.1

Huang, Y., Ding, Q., Dong, X., Xi, B., & Baxter, I. (2021). Summertime low clouds mediate the impact of the large-scale circulation on Arctic sea ice. *Communications Earth & Environment*, *2*(1), Article 1. https://doi.org/10.1038/s43247-021-00114-w

Huang, Y., Xia, Y., & Tan, X. (2017). On the pattern of CO2 radiative forcing and poleward energy transport. *Journal of Geophysical Research: Atmospheres*, *122*(20), 10,578-10,593. https://doi.org/10.1002/2017JD027221

Hurrell, J. W., Holland, M. M., Gent, P. R., Ghan, S., Kay, J. E., Kushner, P. J., Lamarque, J.-F., Large, W. G., Lawrence, D., Lindsay, K., Lipscomb, W. H., Long, M. C., Mahowald, N., Marsh, D. R., Neale, R. B., Rasch, P., Vavrus, S., Vertenstein, M., Bader, D., … Marshall, S. (2013). The Community Earth System Model: A Framework for Collaborative Research. *Bulletin of the American Meteorological Society*, *94*(9), 1339–1360. https://doi.org/10.1175/BAMS-D-12-00121.1

Hwang, Y.-T., Frierson, D. M. W., & Kay, J. E. (2011). Coupling between Arctic feedbacks and changes in poleward energy transport. *Geophysical Research Letters*, *38*(17). https://doi.org/10.1029/2011GL048546

Ilıcak, M., Drange, H., Wang, Q., Gerdes, R., Aksenov, Y., Bailey, D., Bentsen, M., Biastoch, A., Bozec, A., Böning, C., Cassou, C., Chassignet, E., Coward, A. C., Curry, B., Danabasoglu, G., Danilov, S., Fernandez, E., Fogli, P. G., Fujii, Y., … Yeager, S. G. (2016). An assessment of the Arctic Ocean in a suite of interannual CORE-II simulations. Part III: Hydrography and fluxes. *Ocean Modelling*, *100*, 141–161. https://doi.org/10.1016/j.ocemod.2016.02.004

Jahn, A., Holland, M. M., & Kay, J. E. (2024). Projections of an ice-free Arctic Ocean. *Nature Reviews Earth & Environment*, *5*(3), 164–176. https://doi.org/10.1038/s43017-023-00515-9

Jahn, A., & Laiho, R. (2020). Forced Changes in the Arctic Freshwater Budget Emerge in the Early 21st Century. *Geophysical Research Letters*, *47*(15), e2020GL088854. https://doi.org/10.1029/2020GL088854

Jones, P. D., New, M., Parker, D. E., Martin, S., & Rigor, I. G. (1999). Surface air temperature and its changes over the past 150 years. *Reviews of Geophysics*, *37*(2), 173–199. https://doi.org/10.1029/1999RG900002

Josey, S. A., de Jong, M. F., Oltmanns, M., Moore, G. K., & Weller, R. A. (2019). Extreme Variability in Irminger Sea Winter Heat Loss Revealed by Ocean Observatories Initiative Mooring and the ERA5 Reanalysis. *Geophysical Research Letters*, *46*(1), 293–302. https://doi.org/10.1029/2018GL080956

Kapsch, M.-L., Graversen, R. G., Tjernström, M., & Bintanja, R. (2016). The Effect of Downwelling Longwave and Shortwave Radiation on Arctic Summer Sea Ice. *Journal of Climate*, *29*(3), 1143–1159. https://doi.org/10.1175/JCLI-D-15-0238.1

Kashiwase, H., Ohshima, K. I., Nihashi, S., & Eicken, H. (2017). Evidence for ice-ocean albedo feedback in the Arctic Ocean shifting to a seasonal ice zone. *Scientific Reports*, *7*(1), Article 1. https://doi.org/10.1038/s41598-017-08467-z

Kay, J. E., Deser, C., Phillips, A., Mai, A., Hannay, C., Strand, G., Arblaster, J. M., Bates, S. C., Danabasoglu, G., Edwards, J., Holland, M., Kushner, P., Lamarque, J.-F., Lawrence, D., Lindsay, K., Middleton, A., Munoz, E., Neale, R., Oleson, K., … Vertenstein, M. (2015). The Community Earth System Model (CESM) Large

Ensemble Project: A Community Resource for Studying Climate Change in the Presence of Internal Climate Variability. *Bulletin of the American Meteorological Society*, *96*(8), 1333–1349. https://doi.org/10.1175/BAMS-D-13-00255.1

Kay, J. E., Holland, M. M., Bitz, C. M., Blanchard-Wrigglesworth, E., Gettelman, A., Conley, A., & Bailey, D. (2012). The Influence of Local Feedbacks and Northward Heat Transport on the Equilibrium Arctic Climate Response to Increased Greenhouse Gas Forcing. *Journal of Climate*, *25*(16), 5433–5450. https://doi.org/10.1175/JCLI-D-11-00622.1

Keil, P., Mauritsen, T., Jungclaus, J., Hedemann, C., Olonscheck, D., & Ghosh, R. (2020). Multiple drivers of the North Atlantic warming hole. *Nature Climate Change*, *10*(7), Article 7. https://doi.org/10.1038/s41558-020-0819-8

Kennedy, J. J., Rayner, N. A., Atkinson, C. P., & Killick, R. E. (2019). An Ensemble Data Set of Sea Surface Temperature Change From 1850: The Met Office Hadley Centre HadSST.4.0.0.0 Data Set. *Journal of Geophysical Research: Atmospheres*, *124*(14), 7719–7763. https://doi.org/10.1029/2018JD029867

Kodama, C., & Iwasaki, T. (2009). Influence of the SST Rise on Baroclinic Instability Wave Activity under an Aquaplanet Condition. *Journal of the Atmospheric Sciences*, *66*(8), 2272–2287. https://doi.org/10.1175/2009JAS2964.1

Köhl, A. (2020). Evaluating the GECCO3 1948–2018 ocean synthesis – a configuration for initializing the MPI-ESM climate model. *Quarterly Journal of the Royal Meteorological Society*, *146*(730), 2250–2273. https://doi.org/10.1002/qj.3790

Krishfield, R. A., Proshutinsky, A., Tateyama, K., Williams, W. J., Carmack, E. C., McLaughlin, F. A., & Timmermans, M.-L. (2014). Deterioration of perennial sea ice in the Beaufort Gyre from 2003 to 2012 and its impact on the oceanic freshwater cycle. *Journal of Geophysical Research: Oceans*, *119*(2), 1271–1305. https://doi.org/10.1002/2013JC008999

Lamjiri, M. A., Dettinger, M. D., Ralph, F. M., & Guan, B. (2017). Hourly storm characteristics along the U.S. West Coast: Role of atmospheric rivers in extreme precipitation. *Geophysical Research Letters*, *44*(13), 7020–7028. https://doi.org/10.1002/2017GL074193

Landrum, L., & Holland, M. M. (2020). Extremes become routine in an emerging new Arctic. *Nature Climate Change*, *10*(12), Article 12. https://doi.org/10.1038/s41558-020-0892-z

Lang, C., Fettweis, X., & Erpicum, M. (2015). Future climate and surface mass balance of Svalbard glaciers in an RCP8.5 climate scenario: A study with the regional climate model MAR forced by MIROC5. *The Cryosphere*, *9*(3), 945–956. https://doi.org/10.5194/tc-9-945-2015

Latif, M., Sun, J., Visbeck, M., & Hadi Bordbar, M. (2022). Natural variability has dominated Atlantic Meridional Overturning Circulation since 1900. *Nature Climate Change*, *12*(5), Article 5. https://doi.org/10.1038/s41558-022-01342-4

Lavers, D. A., & Villarini, G. (2015). The contribution of atmospheric rivers to precipitation in Europe and the United States. *Journal of Hydrology*, *522*, 382–390. https://doi.org/10.1016/j.jhydrol.2014.12.010

Lehmann, J., Coumou, D., Frieler, K., Eliseev, A. V., & Levermann, A. (2014). Future changes in extratropical storm tracks and baroclinicity under climate change.

Environmental Research Letters, *9*(8), 084002. https://doi.org/10.1088/1748-9326/9/8/084002

Lesk, C., Rowhani, P., & Ramankutty, N. (2016). Influence of extreme weather disasters on global crop production. *Nature*, *529*(7584), Article 7584. https://doi.org/10.1038/nature16467

Lewis, N. (2022). Objectively combining climate sensitivity evidence. *Climate Dynamics*. https://doi.org/10.1007/s00382-022-06468-x

Li, L., Lozier, M. S., & Li, F. (2022). Century-long cooling trend in subpolar North Atlantic forced by atmosphere: An alternative explanation. *Climate Dynamics*, *58*(9), 2249–2267. https://doi.org/10.1007/s00382-021-06003-4

Li, Z., Ding, Q., Steele, M., & Schweiger, A. (2022). Recent upper Arctic Ocean warming expedited by summertime atmospheric processes. *Nature Communications*, *13*(1), Article 1. https://doi.org/10.1038/s41467-022-28047-8

Lien, V. S., Schlichtholz, P., Skagseth, Ø., & Vikebø, F. B. (2017). Wind-Driven Atlantic Water Flow as a Direct Mode for Reduced Barents Sea Ice Cover. *Journal of Climate*, *30*(2), 803–812. https://doi.org/10.1175/JCLI-D-16-0025.1

Lind, S., Ingvaldsen, R. B., & Furevik, T. (2018). Arctic warming hotspot in the northern Barents Sea linked to declining sea-ice import. *Nature Climate Change*, *8*(7), 634–639. https://doi.org/10.1038/s41558-018-0205-y

Lindsay, R. W., & Zhang, J. (2005). The Thinning of Arctic Sea Ice, 1988–2003: Have We Passed a Tipping Point? *Journal of Climate*, *18*(22), 4879–4894. https://doi.org/10.1175/JCLI3587.1

Lique, C. (2015). Arctic sea ice heated from below. *Nature Geoscience*, *8*(3), Article 3. https://doi.org/10.1038/ngeo2357

Liu, W., Fedorov, A. V., Xie, S.-P., & Hu, S. (2020). Climate impacts of a weakened Atlantic Meridional Overturning Circulation in a warming climate. *Science Advances*, *6*(26), eaaz4876. https://doi.org/10.1126/sciadv.aaz4876

Lorenz, D. J., & DeWeaver, E. T. (2007). Tropopause height and zonal wind response to global warming in the IPCC scenario integrations. *Journal of Geophysical Research: Atmospheres*, *112*(D10). https://doi.org/10.1029/2006JD008087

Lozier, M. S., Li, F., Bacon, S., Bahr, F., Bower, A. S., Cunningham, S. A., de Jong, M. F., de Steur, L., deYoung, B., Fischer, J., Gary, S. F., Greenan, B. J. W., Holliday, N. P., Houk, A., Houpert, L., Inall, M. E., Johns, W. E., Johnson, H. L., Johnson, C., … Zhao, J. (2019). A sea change in our view of overturning in the subpolar North Atlantic. *Science*, *363*(6426), 516–521. https://doi.org/10.1126/science.aau6592

Lu, J., Chen, G., & Frierson, D. M. W. (2008). Response of the Zonal Mean Atmospheric Circulation to El Niño versus Global Warming. *Journal of Climate*, *21*(22), 5835–5851. https://doi.org/10.1175/2008JCLI2200.1

Lu, J., Chen, G., & Frierson, D. M. W. (2010). The Position of the Midlatitude Storm Track and Eddy-Driven Westerlies in Aquaplanet AGCMs. *Journal of the Atmospheric Sciences*, *67*(12), 3984–4000. https://doi.org/10.1175/2010JAS3477.1

Lu, J., Vecchi, G. A., & Reichler, T. (2007). Expansion of the Hadley cell under global warming. *Geophysical Research Letters*, *34*(6). https://doi.org/10.1029/2006GL028443

Ma, W., Chen, G., & Guan, B. (2020). Poleward Shift of Atmospheric Rivers in the Southern Hemisphere in Recent Decades. *Geophysical Research Letters*, *47*(21), e2020GL089934. https://doi.org/10.1029/2020GL089934

Ma, W., Norris, J., & Chen, G. (2020). Projected Changes to Extreme Precipitation Along North American West Coast From the CESM Large Ensemble. *Geophysical Research Letters*, *47*(1), e2019GL086038. https://doi.org/10.1029/2019GL086038

Madakumbura, G. D., Kim, H., Utsumi, N., Shiogama, H., Fischer, E. M., Seland, Ø., Scinocca, J. F., Mitchell, D. M., Hirabayashi, Y., & Oki, T. (2019). Event-to-event intensification of the hydrologic cycle from 1.5 °C to a 2 °C warmer world. *Scientific Reports*, *9*(1), Article 1. https://doi.org/10.1038/s41598-019-39936-2

Madonna, E., & Sandø, A. B. (2022). Understanding Differences in North Atlantic Poleward Ocean Heat Transport and Its Variability in Global Climate Models. *Geophysical Research Letters*, *49*(1), e2021GL096683. https://doi.org/10.1029/2021GL096683

Marshall, J., Scott, J. R., Armour, K. C., Campin, J.-M., Kelley, M., & Romanou, A. (2015). The ocean's role in the transient response of climate to abrupt greenhouse gas forcing. *Climate Dynamics*, *44*(7), 2287–2299. https://doi.org/10.1007/s00382-014-2308-0

Mattingly, K. S., Turton, J. V., Wille, J. D., Noël, B., Fettweis, X., Rennermalm, Å. K., & Mote, T. L. (2023). Increasing extreme melt in northeast Greenland linked to foehn winds and atmospheric rivers. *Nature Communications*, *14*(1), 1743. https://doi.org/10.1038/s41467-023-37434-8

Mayer, M., Haimberger, L., Pietschnig, M., & Storto, A. (2016). Facets of Arctic energy accumulation based on observations and reanalyses 2000–2015. *Geophysical Research Letters*, *43*(19), 10,420-10,429. https://doi.org/10.1002/2016GL070557

Mbengue, C., & Schneider, T. (2017). Storm-Track Shifts under Climate Change: Toward a Mechanistic Understanding Using Baroclinic Mean Available Potential Energy. *Journal of the Atmospheric Sciences*, *74*(1), 93–110. https://doi.org/10.1175/JAS-D-15-0267.1

McCarthy, G. D., Haigh, I. D., Hirschi, J. J.-M., Grist, J. P., & Smeed, D. A. (2015). Ocean impact on decadal Atlantic climate variability revealed by sea-level observations. *Nature*, *521*(7553), Article 7553. https://doi.org/10.1038/nature14491

McGowan, H., Borthwick, K., Schwartz, A., Callow, J. N., Bilish, S., & Browning, S. (2021). Atmospheric Rivers: An Overlooked Threat to the Marginal Snowpack of the Australian Alps. *Journal of Hydrometeorology*, *22*(10), 2521–2532. https://doi.org/10.1175/JHM-D-20-0293.1

McLeod, J. T., & Mote, T. L. (2016). Linking interannual variability in extreme Greenland blocking episodes to the recent increase in summer melting across the Greenland ice sheet. *International Journal of Climatology*, *36*(3), 1484–1499. https://doi.org/10.1002/joc.4440

McMonigal, K. (2024). Aerosols hold the key to recent and future Pacific warming patterns. *Proceedings of the National Academy of Sciences*, *121*(6), e2322594121. https://doi.org/10.1073/pnas.2322594121

Meehl, G. A., Chung, C. T. Y., Arblaster, J. M., Holland, M. M., & Bitz, C. M. (2018). Tropical Decadal Variability and the Rate of Arctic Sea Ice Decrease. *Geophysical Research Letters*, *45*(20), 11,326-11,333. https://doi.org/10.1029/2018GL079989

Meehl, G. A., & Tebaldi, C. (2004). More Intense, More Frequent, and Longer Lasting Heat Waves in the 21st Century. *Science*, *305*(5686), 994–997. https://doi.org/10.1126/science.1098704

Menary, M. B., & Wood, R. A. (2018). An anatomy of the projected North Atlantic warming hole in CMIP5 models. *Climate Dynamics*, *50*(7), 3063–3080. https://doi.org/10.1007/s00382-017-3793-8

Mo, K. C., & Livezey, R. E. (1986). Tropical-Extratropical Geopotential Height Teleconnections during the Northern Hemisphere Winter. *Monthly Weather Review*, *114*(12), 2488–2515. https://doi.org/10.1175/1520-0493(1986)114<2488:TEGHTD>2.0.CO;2

Mogensen, K., & Balmaseda, W. (2012). *The NEMOVAR ocean data assimilation system as implemented in the ECMWF ocean analysis for System 4*. ECMWF. https://doi.org/10.21957/x5y9yrtm

Muilwijk, M., Ilicak, M., Cornish, S. B., Danilov, S., Gelderloos, R., Gerdes, R., Haid, V., Haine, T. W. N., Johnson, H. L., Kostov, Y., Kovács, T., Lique, C., Marson, J. M., Myers, P. G., Scott, J., Smedsrud, L. H., Talandier, C., & Wang, Q. (2019). Arctic Ocean Response to Greenland Sea Wind Anomalies in a Suite of Model Simulations. *Journal of Geophysical Research: Oceans*, *124*(8), 6286–6322. https://doi.org/10.1029/2019JC015101

Muilwijk, M., Smedsrud, L. H., Ilicak, M., & Drange, H. (2018). Atlantic Water Heat Transport Variability in the 20th Century Arctic Ocean From a Global Ocean Model and Observations. *Journal of Geophysical Research: Oceans*, *123*(11), 8159–8179. https://doi.org/10.1029/2018JC014327

Musselman, K. N., Lehner, F., Ikeda, K., Clark, M. P., Prein, A. F., Liu, C., Barlage, M., & Rasmussen, R. (2018). Projected increases and shifts in rain-on-snow flood risk over western North America. *Nature Climate Change*, *8*(9), Article 9. https://doi.org/10.1038/s41558-018-0236-4

Myers, P. G., Donnelly, C., & Ribergaard, M. H. (2009). Structure and variability of the West Greenland Current in Summer derived from 6 repeat standard sections. *Progress in Oceanography*, *80*(1), 93–112. https://doi.org/10.1016/j.pocean.2008.12.003

Myhre, G., Alterskjær, K., Stjern, C. W., Hodnebrog, Ø., Marelle, L., Samset, B. H., Sillmann, J., Schaller, N., Fischer, E., Schulz, M., & Stohl, A. (2019). Frequency of extreme precipitation increases extensively with event rareness under global warming. *Scientific Reports*, *9*(1), Article 1. https://doi.org/10.1038/s41598-019-52277-4

Nakamura, T., Yamazaki, K., Iwamoto, K., Honda, M., Miyoshi, Y., Ogawa, Y., & Ukita, J. (2015). A negative phase shift of the winter AO/NAO due to the recent Arctic sea-ice reduction in late autumn. *Journal of Geophysical Research: Atmospheres*, *120*(8), 3209–3227. https://doi.org/10.1002/2014JD022848

Nash, D., Waliser, D., Guan, B., Ye, H., & Ralph, F. M. (2018). The Role of Atmospheric Rivers in Extratropical and Polar Hydroclimate. *Journal of Geophysical Research: Atmospheres*, *123*(13), 6804–6821. https://doi.org/10.1029/2017JD028130

Notz, D., & Stroeve, J. (2016). Observed Arctic sea-ice loss directly follows anthropogenic CO2 emission. *Science*, *354*(6313), 747–750. https://doi.org/10.1126/science.aag2345

O'Gorman, P. A. (2015). Precipitation Extremes Under Climate Change. *Current Climate Change Reports*, *1*(2), 49–59. https://doi.org/10.1007/s40641-015-0009-3

O'Gorman, P. A., & Schneider, T. (2009). The physical basis for increases in precipitation extremes in simulations of 21st-century climate change. *Proceedings of the National Academy of Sciences*, *106*(35), 14773–14777. https://doi.org/10.1073/pnas.0907610106

Oldenburg, D., Armour, K. C., Thompson, L., & Bitz, C. M. (2018). Distinct Mechanisms of Ocean Heat Transport Into the Arctic Under Internal Variability and Climate Change. *Geophysical Research Letters*, *45*(15), 7692–7700. https://doi.org/10.1029/2018GL078719

Oltmanns, M., Karstensen, J., Moore, G. W. K., & Josey, S. A. (2020). Rapid Cooling and Increased Storminess Triggered by Freshwater in the North Atlantic. *Geophysical Research Letters, 47*(14), e2020GL087207. https://doi.org/10.1029/2020GL087207

Orvik, K. A., & Skagseth, Ø. (2003). The impact of the wind stress curl in the North Atlantic on the Atlantic inflow to the Norwegian Sea toward the Arctic. *Geophysical Research Letters, 30*(17). https://doi.org/10.1029/2003GL017932

Papalexiou, S. M., & Montanari, A. (2019). Global and Regional Increase of Precipitation Extremes Under Global Warming. *Water Resources Research*, *55*(6), 4901–4914. https://doi.org/10.1029/2018WR024067

Perlwitz, J., Hoerling, M., & Dole, R. (2015). Arctic Tropospheric Warming: Causes and Linkages to Lower Latitudes. *Journal of Climate*, *28*(6), 2154–2167. https://doi.org/10.1175/JCLI-D-14-00095.1

Perovich, D. K., Light, B., Eicken, H., Jones, K. F., Runciman, K., & Nghiem, S. V. (2007). Increasing solar heating of the Arctic Ocean and adjacent seas, 1979–2005: Attribution and role in the ice-albedo feedback. *Geophysical Research Letters*, *34*(19). https://doi.org/10.1029/2007GL031480

Pithan, F., & Mauritsen, T. (2014). Arctic amplification dominated by temperature feedbacks in contemporary climate models. *Nature Geoscience*, *7*(3), 181–184. https://doi.org/10.1038/ngeo2071

Polyakov, I., Timokhov, L., Dmitrenko, I., Ivanov, V., Simmons, H., Beszczynska-Möller, A., Dickson, R., Fahrbach, E., Fortier, L., Gascard, J.-C., Hölemann, J., Holliday, N. P., Hansen, E., Mauritzen, C., Piechura, J., Pickart, R., Schauer, U., Walczowski, W., & Steele, M. (2007). Observational program tracks Arctic Ocean transition to a warmer state. *Eos, Transactions American Geophysical Union*, *88*(40), 398–399. https://doi.org/10.1029/2007EO400002

Polyakov, I. V., Alkire, M. B., Bluhm, B. A., Brown, K. A., Carmack, E. C., Chierici, M., Danielson, S. L., Ellingsen, I., Ershova, E. A., Gårdfeldt, K., Ingvaldsen, R. B., Pnyushkov, A. V., Slagstad, D., & Wassmann, P. (2020). Borealization of the Arctic

Ocean in Response to Anomalous Advection From Sub-Arctic Seas. *Frontiers in Marine Science*, *7*. https://doi.org/10.3389/fmars.2020.00491

Polyakov, I. V., Pnyushkov, A. V., Alkire, M. B., Ashik, I. M., Baumann, T. M., Carmack, E. C., Goszczko, I., Guthrie, J., Ivanov, V. V., Kanzow, T., Krishfield, R., Kwok, R., Sundfjord, A., Morison, J., Rember, R., & Yulin, A. (2017). Greater role for Atlantic inflows on sea-ice loss in the Eurasian Basin of the Arctic Ocean. *Science*, *356*(6335), 285–291. https://doi.org/10.1126/science.aai8204

Polyakov, I. V., Rippeth, T. P., Fer, I., Alkire, M. B., Baumann, T. M., Carmack, E. C., Ingvaldsen, R., Ivanov, V. V., Janout, M., Lind, S., Padman, L., Pnyushkov, A. V., & Rember, R. (2020). Weakening of Cold Halocline Layer Exposes Sea Ice to Oceanic Heat in the Eastern Arctic Ocean. *Journal of Climate*, *33*(18), 8107–8123. https://doi.org/10.1175/JCLI-D-19-0976.1

Polyakov, I. V., Timokhov, L. A., Alexeev, V. A., Bacon, S., Dmitrenko, I. A., Fortier, L., Frolov, I. E., Gascard, J.-C., Hansen, E., Ivanov, V. V., Laxon, S., Mauritzen, C., Perovich, D., Shimada, K., Simmons, H. L., Sokolov, V. T., Steele, M., & Toole, J. (2010). Arctic Ocean Warming Contributes to Reduced Polar Ice Cap. *Journal of Physical Oceanography*, *40*(12), 2743–2756. https://doi.org/10.1175/2010JPO4339.1

Polyakov, I. V., Walsh, J. E., & Kwok, R. (2012). Recent Changes of Arctic Multiyear Sea Ice Coverage and the Likely Causes. *Bulletin of the American Meteorological Society*, *93*(2), 145–151. https://doi.org/10.1175/BAMS-D-11-00070.1

Priestley, M. D. K., & Catto, J. L. (2022). Future changes in the extratropical storm tracks and cyclone intensity, wind speed, and structure. *Weather and Climate Dynamics*, *3*(1), 337–360. https://doi.org/10.5194/wcd-3-337-2022

Proshutinsky, A., Dukhovskoy, D., Timmermans, M.-L., Krishfield, R., & Bamber, J. L. (2015). Arctic circulation regimes. *Philosophical Transactions of the Royal Society A: Mathematical, Physical and Engineering Sciences*, *373*(2052), 20140160. https://doi.org/10.1098/rsta.2014.0160

Rahmstorf, S., Box, J. E., Feulner, G., Mann, M. E., Robinson, A., Rutherford, S., & Schaffernicht, E. J. (2015). Exceptional twentieth-century slowdown in Atlantic Ocean overturning circulation. *Nature Climate Change*, *5*(5), Article 5. https://doi.org/10.1038/nclimate2554

Rantanen, M., Karpechko, A. Y., Lipponen, A., Nordling, K., Hyvärinen, O., Ruosteenoja, K., Vihma, T., & Laaksonen, A. (2022). The Arctic has warmed nearly four times faster than the globe since 1979. *Communications Earth & Environment*, *3*(1), 1–10. https://doi.org/10.1038/s43247-022-00498-3

Ricker, R., Kauker, F., Schweiger, A., Hendricks, S., Zhang, J., & Paul, S. (2021). Evidence for an increasing role of ocean heat in Arctic winter sea ice growth. *Journal of Climate*, *1*(aop), 1–42. https://doi.org/10.1175/JCLI-D-20-0848.1

Rignot, E., Fenty, I., Menemenlis, D., & Xu, Y. (2012). Spreading of warm ocean waters around Greenland as a possible cause for glacier acceleration. *Annals of Glaciology*, *53*(60), 257–266. https://doi.org/10.3189/2012AoG60A136

Rigor, I. G., Colony, R. L., & Martin, S. (2000). Variations in Surface Air Temperature Observations in the Arctic, 1979–97. *Journal of Climate*, *13*(5), 896–914. https://doi.org/10.1175/1520-0442(2000)013<0896:VISATO>2.0.CO;2

Roach, L. A., Blanchard-Wrigglesworth, E., Ragen, S., Cheng, W., Armour, K. C., & Bitz, C. M. (2022). The Impact of Winds on AMOC in a Fully-Coupled Climate Model.

Geophysical Research Letters, *49*(24), e2022GL101203. https://doi.org/10.1029/2022GL101203

Rodgers, K. B., Lee, S.-S., Rosenbloom, N., Timmermann, A., Danabasoglu, G., Deser, C., Edwards, J., Kim, J.-E., Simpson, I. R., Stein, K., Stuecker, M. F., Yamaguchi, R., Bódai, T., Chung, E.-S., Huang, L., Kim, W. M., Lamarque, J.-F., Lombardozzi, D. L., Wieder, W. R., & Yeager, S. G. (2021). Ubiquity of human-induced changes in climate variability. *Earth System Dynamics*, *12*(4), 1393–1411. https://doi.org/10.5194/esd-12-1393-2021

Sallée, J.-B., Pellichero, V., Akhoudas, C., Pauthenet, E., Vignes, L., Schmidtko, S., Garabato, A. N., Sutherland, P., & Kuusela, M. (2021). Summertime increases in upper-ocean stratification and mixed-layer depth. *Nature*, *591*(7851), 592–598. https://doi.org/10.1038/s41586-021-03303-x

Santer, B. D., Taylor, K. E., Wigley, T. M. L., Johns, T. C., Jones, P. D., Karoly, D. J., Mitchell, J. F. B., Oort, A. H., Penner, J. E., Ramaswamy, V., Schwarzkopf, M. D., Stouffer, R. J., & Tett, S. (1996). A search for human influences on the thermal structure of the atmosphere. *Nature*, *382*(6586), Article 6586. https://doi.org/10.1038/382039a0

Scafetta, N. (2022). CMIP6 GCM ensemble members versus global surface temperatures. *Climate Dynamics*. https://doi.org/10.1007/s00382-022-06493-w

Screen, J. A., & Francis, J. A. (2016). Contribution of sea-ice loss to Arctic amplification is regulated by Pacific Ocean decadal variability. *Nature Climate Change*, *6*(9), Article 9. https://doi.org/10.1038/nclimate3011

Screen, J. A., & Simmonds, I. (2010). The central role of diminishing sea ice in recent Arctic temperature amplification. *Nature*, *464*(7293), 1334–1337. https://doi.org/10.1038/nature09051

Seager, R., Harnik, N., Kushnir, Y., Robinson, W., & Miller, J. (2003). Mechanisms of Hemispherically Symmetric Climate Variability. *Journal of Climate*, *16*(18), 2960–2978. https://doi.org/10.1175/1520-0442(2003)016<2960:MOHSCV>2.0.CO;2

Seager, R., Neelin, D., Simpson, I., Liu, H., Henderson, N., Shaw, T., Kushnir, Y., Ting, M., & Cook, B. (2014). Dynamical and Thermodynamical Causes of Large-Scale Changes in the Hydrological Cycle over North America in Response to Global Warming. *Journal of Climate*, *27*(20), 7921–7948. https://doi.org/10.1175/JCLI-D-14-00153.1

Serreze, M. C., Barrett, A. P., Slater, A. G., Steele, M., Zhang, J., & Trenberth, K. E. (2007). The large-scale energy budget of the Arctic. *Journal of Geophysical Research: Atmospheres*, *112*(D11). https://doi.org/10.1029/2006JD008230

Serreze, M. C., Barrett, A. P., Stroeve, J. C., Kindig, D. N., & Holland, M. M. (2009). The emergence of surface-based Arctic amplification. *The Cryosphere*, *3*(1), 11–19. https://doi.org/10.5194/tc-3-11-2009

Serreze, M. C., & Barry, R. G. (2011). Processes and impacts of Arctic amplification: A research synthesis. *Global and Planetary Change*, *77*(1), 85–96. https://doi.org/10.1016/j.gloplacha.2011.03.004

Sharmila, S., & Walsh, K. J. E. (2018). Recent poleward shift of tropical cyclone formation linked to Hadley cell expansion. *Nature Climate Change*, *8*(8), 730–736. https://doi.org/10.1038/s41558-018-0227-5

Shields, C. A., & Kiehl, J. T. (2016). Atmospheric river landfall-latitude changes in future climate simulations. *Geophysical Research Letters*, *43*(16), 8775–8782. https://doi.org/10.1002/2016GL070470

Shields, C. A., Payne, A. E., Shearer, E. J., Wehner, M. F., O'Brien, T. A., Rutz, J. J., Leung, L. R., Ralph, F. M., Marquardt Collow, A. B., Ullrich, P. A., Dong, Q., Gershunov, A., Griffith, H., Guan, B., Lora, J. M., Lu, M., McClenny, E., Nardi, K. M., Pan, M., … Zarzycki, C. (2023). Future Atmospheric Rivers and Impacts on Precipitation: Overview of the ARTMIP Tier 2 High-Resolution Global Warming Experiment. *Geophysical Research Letters*, *50*(6), e2022GL102091. https://doi.org/10.1029/2022GL102091

Shields, C. A., Rutz, J. J., Leung, L. R., Ralph, F. M., Wehner, M., O'Brien, T., & Pierce, R. (2019). Defining uncertainties through comparison of atmospheric river tracking methods. *Bulletin of the American Meteorological Society*, ES93–ES96. https://doi.org/10.1175/BAMS-D-18-0200.1

Shu, Q., Wang, Q., Song, Z., & Qiao, F. (2021). The poleward enhanced Arctic Ocean cooling machine in a warming climate. *Nature Communications*, *12*(1), 2966. https://doi.org/10.1038/s41467-021-23321-7

Skagseth, Ø., Eldevik, T., Årthun, M., Asbjørnsen, H., Lien, V. S., & Smedsrud, L. H. (2020). Reduced efficiency of the Barents Sea cooling machine. *Nature Climate Change*, *10*(7), Article 7. https://doi.org/10.1038/s41558-020-0772-6

Smedsrud, L. H., Link to external site, this link will open in a new window, Brakstad, A., Madonna, E., Muilwijk, M., Link to external site, this link will open in a new window, Lauvset, S. K., Spensberger, C., Link to external site, this link will open in a new window, Born, A., Eldevik, T., Drange, H., Jeansson, E., Li, C., Olsen, A., Skagseth, Ø., Slater, D. A., Straneo, F., Link to external site, this link will open in a new window, … Årthun, M. (2021). Nordic Seas Heat Loss, Atlantic Inflow, and Arctic Sea Ice cover over the last century. *Earth and Space Science Open Archive ESSOAr*. http://dx.doi.org/10.1002/essoar.10506171.1

Smeed, D. A., Josey, S. A., Beaulieu, C., Johns, W. E., Moat, B. I., Frajka-Williams, E., Rayner, D., Meinen, C. S., Baringer, M. O., Bryden, H. L., & McCarthy, G. D. (2018). The North Atlantic Ocean Is in a State of Reduced Overturning. *Geophysical Research Letters*, *45*(3), 1527–1533. https://doi.org/10.1002/2017GL076350

Staten, P. W., Lu, J., Grise, K. M., Davis, S. M., & Birner, T. (2018). Re-examining tropical expansion. *Nature Climate Change*, *8*(9), Article 9. https://doi.org/10.1038/s41558-018-0246-2

Steele, M., Ermold, W., & Zhang, J. (2008). Arctic Ocean surface warming trends over the past 100 years. *Geophysical Research Letters*, *35*(2). https://doi.org/10.1029/2007GL031651

Steele, M., Ermold, W., & Zhang, J. (2011). Modeling the formation and fate of the near-surface temperature maximum in the Canadian Basin of the Arctic Ocean. *Journal of Geophysical Research: Oceans*, *116*(C11). https://doi.org/10.1029/2010JC006803

Steele, M., Zhang, J., & Ermold, W. (2010). Mechanisms of summertime upper Arctic Ocean warming and the effect on sea ice melt. *Journal of Geophysical Research: Oceans*, *115*(C11). https://doi.org/10.1029/2009JC005849

Storto, A., Alvera-Azcárate, A., Balmaseda, M. A., Barth, A., Chevallier, M., Counillon, F., Domingues, C. M., Drevillon, M., Drillet, Y., Forget, G., Garric, G., Haines, K., Hernandez, F., Iovino, D., Jackson, L. C., Lellouche, J.-M., Masina, S., Mayer, M., Oke, P. R., … Zuo, H. (2019). Ocean Reanalyses: Recent Advances and Unsolved Challenges. *Frontiers in Marine Science*, *6*. https://doi.org/10.3389/fmars.2019.00418

Stroeve, J. C., Markus, T., Boisvert, L., Miller, J., & Barrett, A. (2014). Changes in Arctic melt season and implications for sea ice loss. *Geophysical Research Letters*, *41*(4), 1216–1225. https://doi.org/10.1002/2013GL058951

Stroeve, J. C., Mioduszewski, J. R., Rennermalm, A., Boisvert, L. N., Tedesco, M., & Robinson, D. (2017). Investigating the local-scale influence of sea ice on Greenland surface melt. *The Cryosphere*, *11*(5), 2363–2381. https://doi.org/10.5194/tc-11-2363-2017

Stroeve, J., & Notz, D. (2018). Changing state of Arctic sea ice across all seasons. *Environmental Research Letters*, *13*(10), 103001. https://doi.org/10.1088/1748-9326/aade56

Studholme, J., Fedorov, A. V., Gulev, S. K., Emanuel, K., & Hodges, K. (2022). Poleward expansion of tropical cyclone latitudes in warming climates. *Nature Geoscience*, *15*(1), Article 1. https://doi.org/10.1038/s41561-021-00859-1

Studholme, J., & Gulev, S. (2018). Concurrent Changes to Hadley Circulation and the Meridional Distribution of Tropical Cyclones. *Journal of Climate*, *31*(11), 4367–4389. https://doi.org/10.1175/JCLI-D-17-0852.1

Stuecker, M. F., Bitz, C. M., Armour, K. C., Proistosescu, C., Kang, S. M., Xie, S.-P., Kim, D., McGregor, S., Zhang, W., Zhao, S., Cai, W., Dong, Y., & Jin, F.-F. (2018). Polar amplification dominated by local forcing and feedbacks. *Nature Climate Change*, *8*(12), 1076–1081. https://doi.org/10.1038/s41558-018-0339-y

Tabari, H. (2020). Climate change impact on flood and extreme precipitation increases with water availability. *Scientific Reports*, *10*(1), Article 1. https://doi.org/10.1038/s41598-020-70816-2

Tamarin, T., & Kaspi, Y. (2016). The Poleward Motion of Extratropical Cyclones from a Potential Vorticity Tendency Analysis. *Journal of the Atmospheric Sciences*, *73*(4), 1687–1707. https://doi.org/10.1175/JAS-D-15-0168.1

Tamarin, T., & Kaspi, Y. (2017). The poleward shift of storm tracks under global warming: A Lagrangian perspective. *Geophysical Research Letters, 44*(20), 10,666-10,674. https://doi.org/10.1002/2017GL073633

Tamarin-Brodsky, T., & Kaspi, Y. (2017). Enhanced poleward propagation of storms under climate change. *Nature Geoscience*, *10*(12), Article 12. https://doi.org/10.1038/s41561-017-0001-8

Tett, S. F. B., Stott, P. A., Allen, M. R., Ingram, W. J., & Mitchell, J. F. B. (1999). Causes of twentieth-century temperature change near the Earth’s surface. *Nature, 399*(6736), Article 6736. https://doi.org/10.1038/21164

Timmermans, M.-L., & Marshall, J. (2020). Understanding Arctic Ocean Circulation: A Review of Ocean Dynamics in a Changing Climate. *Journal of Geophysical Research: Oceans*, *125*(4), e2018JC014378. https://doi.org/10.1029/2018JC014378

Timmermans, M.-L., Toole, J., & Krishfield, R. (2018). Warming of the interior Arctic Ocean linked to sea ice losses at the basin margins. *Science Advances*, *4*(8), eaat6773. https://doi.org/10.1126/sciadv.aat6773

Topál, D., & Ding, Q. (2023). Atmospheric circulation-constrained model sensitivity recalibrates Arctic climate projections. *Nature Climate Change*, *13*(7), Article 7. https://doi.org/10.1038/s41558-023-01698-1

Topál, D., Ding, Q., Ballinger, T. J., Hanna, E., Fettweis, X., Li, Z., & Pieczka, I. (2022). Discrepancies between observations and climate models of large-scale wind-driven Greenland melt influence sea-level rise projections. *Nature Communications*, *13*(1), Article 1. https://doi.org/10.1038/s41467-022-34414-2

Trenberth, K. E., Branstator, G. W., Karoly, D., Kumar, A., Lau, N.-C., & Ropelewski, C. (1998). Progress during TOGA in understanding and modeling global teleconnections associated with tropical sea surface temperatures. *Journal of Geophysical Research: Oceans*, *103*(C7), 14291–14324. https://doi.org/10.1029/97JC01444

Tripathy, K. P., Mukherjee, S., Mishra, A. K., Mann, M. E., & Williams, A. P. (2023). Climate change will accelerate the high-end risk of compound drought and heatwave events. *Proceedings of the National Academy of Sciences*, *120*(28), e2219825120. https://doi.org/10.1073/pnas.2219825120

Trusel, L. D., Das, S. B., Osman, M. B., Evans, M. J., Smith, B. E., Fettweis, X., McConnell, J. R., Noël, B. P. Y., & van den Broeke, M. R. (2018). Nonlinear rise in Greenland runoff in response to post-industrial Arctic warming. *Nature*, *564*(7734), Article 7734. https://doi.org/10.1038/s41586-018-0752-4

Tsubouchi, T., Våge, K., Hansen, B., Larsen, K. M. H., Østerhus, S., Johnson, C., Jónsson, S., & Valdimarsson, H. (2021). Increased ocean heat transport into the Nordic Seas and Arctic Ocean over the period 1993–2016. *Nature Climate Change*, *11*(1), Article 1. https://doi.org/10.1038/s41558-020-00941-3

Uotila, P., Goosse, H., Haines, K., Chevallier, M., Barthélemy, A., Bricaud, C., Carton, J., Fučkar, N., Garric, G., Iovino, D., Kauker, F., Korhonen, M., Lien, V. S., Marnela, M., Massonnet, F., Mignac, D., Peterson, K. A., Sadikni, R., Shi, L., … Zhang, Z. (2019). An assessment of ten ocean reanalyses in the polar regions. *Climate Dynamics*, *52*(3), 1613–1650. https://doi.org/10.1007/s00382-018-4242-z

Valler, V., Franke, J., Brugnara, Y., & Brönnimann, S. (2022). An updated global atmospheric paleo-reanalysis covering the last 400 years. *Geoscience Data Journal*, *9*(1), 89–107. https://doi.org/10.1002/gdj3.121

Van Roekel, L., Adcroft, A. J., Danabasoglu, G., Griffies, S. M., Kauffman, B., Large, W., Levy, M., Reichl, B. G., Ringler, T., & Schmidt, M. (2018). The KPP Boundary Layer Scheme for the Ocean: Revisiting Its Formulation and Benchmarking One-Dimensional Simulations Relative to LES. *Journal of Advances in Modeling Earth Systems*, *10*(11), 2647–2685. https://doi.org/10.1029/2018MS001336

Viale, M., Valenzuela, R., Garreaud, R. D., & Ralph, F. M. (2018). Impacts of Atmospheric Rivers on Precipitation in Southern South America. *Journal of Hydrometeorology*, *19*(10), 1671–1687. https://doi.org/10.1175/JHM-D-18-0006.1

Waliser, D., & Guan, B. (2017). Extreme winds and precipitation during landfall of atmospheric rivers. *Nature Geoscience*, *10*(3), Article 3. https://doi.org/10.1038/ngeo2894

Wallace, J. M., Smith, C., & Bretherton, C. S. (1992). Singular Value Decomposition of Wintertime Sea Surface Temperature and 500-mb Height Anomalies. *Journal of*

Climate, *5*(6), 561–576. https://doi.org/10.1175/1520-0442(1992)005<0561:SVDOWS>2.0.CO;2

Wang, Q., Wang, X., Wekerle, C., Danilov, S., Jung, T., Koldunov, N., Lind, S., Sein, D., Shu, Q., & Sidorenko, D. (2019). Ocean Heat Transport Into the Barents Sea: Distinct Controls on the Upward Trend and Interannual Variability. *Geophysical Research Letters*, *46*(22), 13180–13190. https://doi.org/10.1029/2019GL083837

Wang, Q., Wekerle, C., Wang, X., Danilov, S., Koldunov, N. V., Sein, D., Sidorenko, D., Appen, W.-J. von, & Jung, T. (2019, December 20). *Intensification of the Atlantic Water supply to the Arctic Ocean through Fram Strait induced by Arctic sea ice decline* (world) [Preprint]. Earth and Space Science Open Archive; Earth and Space Science Open Archive. https://doi.org/10.1002/essoar.10501439.1

Weijer, W., Cheng, W., Garuba, O. A., Hu, A., & Nadiga, B. T. (2020). CMIP6 Models Predict Significant 21st Century Decline of the Atlantic Meridional Overturning Circulation. *Geophysical Research Letters*, *47*(12), e2019GL086075. https://doi.org/10.1029/2019GL086075

Wendler, G., Eaton, F. D., & Ohtake, T. (1981). Multiple reflection effects on irradiance in the presence of Arctic stratus clouds. *Journal of Geophysical Research: Oceans*, *86*(C3), 2049–2057. https://doi.org/10.1029/JC086iC03p02049

Wett, S., Rhein, M., Kieke, D., Mertens, C., & Moritz, M. (2023). Meridional Connectivity of a 25-Year Observational AMOC Record at 47°N. *Geophysical Research Letters*, *50*(16), e2023GL103284. https://doi.org/10.1029/2023GL103284

Willis, J. K. (2010). Can in situ floats and satellite altimeters detect long-term changes in Atlantic Ocean overturning? *Geophysical Research Letters*, *37*(6). https://doi.org/10.1029/2010GL042372

Wood, M., Rignot, E., Fenty, I., An, L., Bjørk, A., van den Broeke, M., Cai, C., Kane, E., Menemenlis, D., Millan, R., Morlighem, M., Mouginot, J., Noël, B., Scheuchl, B., Velicogna, I., Willis, J. K., & Zhang, H. (2021). Ocean forcing drives glacier retreat in Greenland. *Science Advances*, *7*(1), eaba7282. https://doi.org/10.1126/sciadv.aba7282

Woodgate, R. A. (2018). Increases in the Pacific inflow to the Arctic from 1990 to 2015, and insights into seasonal trends and driving mechanisms from year-round Bering Strait mooring data. *Progress in Oceanography*, *160*, 124–154. https://doi.org/10.1016/j.pocean.2017.12.007

Woodgate, R. A., Weingartner, T. J., & Lindsay, R. (2012). Observed increases in Bering Strait oceanic fluxes from the Pacific to the Arctic from 2001 to 2011 and their impacts on the Arctic Ocean water column. *Geophysical Research Letters*, *39*(24). https://doi.org/10.1029/2012GL054092

Woodgate, R. A., Weingartner, T., & Lindsay, R. (2010). The 2007 Bering Strait oceanic heat flux and anomalous Arctic sea-ice retreat. *Geophysical Research Letters*, *37*(1). https://doi.org/10.1029/2009GL041621

Woodgate, R., Stafford, K., & Prahl, F. (2015). A Synthesis of Year-Round Interdisciplinary Mooring Measurements in the Bering Strait (1990–2014) and the RUSALCA Years (2004–2011). *Oceanography*, *28*(3), 46–67. https://doi.org/10.5670/oceanog.2015.57

Woollings, T., Gregory, J. M., Pinto, J. G., Reyers, M., & Brayshaw, D. J. (2012). Response of the North Atlantic storm track to climate change shaped by ocean–atmosphere coupling. *Nature Geoscience*, *5*(5), Article 5. https://doi.org/10.1038/ngeo1438

Wu, Y., Ting, M., Seager, R., Huang, H.-P., & Cane, M. A. (2011). Changes in storm tracks and energy transports in a warmer climate simulated by the GFDL CM2.1 model. *Climate Dynamics*, *37*(1), 53–72. https://doi.org/10.1007/s00382-010-0776-4

Yang, K., Cai, W., Huang, G., Hu, K., Ng, B., & Wang, G. (2022). Increased variability of the western Pacific subtropical high under greenhouse warming. *Proceedings of the National Academy of Sciences*, *119*(23), e2120335119. https://doi.org/10.1073/pnas.2120335119

Yin, J. H. (2005). A consistent poleward shift of the storm tracks in simulations of 21st century climate. *Geophysical Research Letters*, *32*(18). https://doi.org/10.1029/2005GL023684

Yuan, X., Wang, Y., Ji, P., Wu, P., Sheffield, J., & Otkin, J. A. (2023). A global transition to flash droughts under climate change. *Science*, *380*(6641), 187–191. https://doi.org/10.1126/science.abn6301

Zelinka, M. D., Myers, T. A., McCoy, D. T., Po-Chedley, S., Caldwell, P. M., Ceppi, P., Klein, S. A., & Taylor, K. E. (2020). Causes of Higher Climate Sensitivity in CMIP6 Models. *Geophysical Research Letters*, *47*(1), e2019GL085782. https://doi.org/10.1029/2019GL085782

Zhang, J. (2005). Warming of the arctic ice-ocean system is faster than the global average since the 1960s. *Geophysical Research Letters*, *32*(19). https://doi.org/10.1029/2005GL024216

Zhang, J., Rothrock, D. A., & Steele, M. (1998). Warming of the Arctic Ocean by a strengthened Atlantic Inflow: Model results. *Geophysical Research Letters*, *25*(10), 1745–1748. https://doi.org/10.1029/98GL01299

Zhang, L., Zhao, Y., Cheng, T. F., & Lu, M. (2024). Future Changes in Global Atmospheric Rivers Projected by CMIP6 Models. *Journal of Geophysical Research: Atmospheres*, *129*(3), e2023JD039359. https://doi.org/10.1029/2023JD039359

Zhang, R. (2015). Mechanisms for low-frequency variability of summer Arctic sea ice extent. *Proceedings of the National Academy of Sciences*, *112*(15), 4570–4575. https://doi.org/10.1073/pnas.1422296112

Zhang, R. (2017). On the persistence and coherence of subpolar sea surface temperature and salinity anomalies associated with the Atlantic multidecadal variability. *Geophysical Research Letters*, *44*(15), 7865–7875. https://doi.org/10.1002/2017GL074342

Zhang, W., Wang, Q., Wang, X., & Danilov, S. (2020). Mechanisms Driving the Interannual Variability of the Bering Strait Throughflow. *Journal of Geophysical Research: Oceans*, *125*(2), e2019JC015308. https://doi.org/10.1029/2019JC015308

Zhang, X., Tang, H., Zhang, J., Walsh, J. E., Roesler, E. L., Hillman, B., Ballinger, T. J., & Weijer, W. (2023). Arctic cyclones have become more intense and longer-lived over the past seven decades. *Communications Earth & Environment*, *4*(1), Article 1. https://doi.org/10.1038/s43247-023-01003-0

Zhu, J., Poulsen, C. J., & Otto-Bliesner, B. L. (2020). High climate sensitivity in CMIP6 model not supported by paleoclimate. *Nature Climate Change*, *10*(5), Article 5. https://doi.org/10.1038/s41558-020-0764-6

Zhu, Y., & Newell, R. E. (1994). Atmospheric rivers and bombs. *Geophysical Research Letters*, *21*(18), 1999–2002. https://doi.org/10.1029/94GL01710

Zhu, Y., & Newell, R. E. (1998). A proposed algorithm for moisture fluxes from atmospheric rivers. *Monthly Weather Review*, *126*(3), 725–735.

Zuo, H., Balmaseda, M. A., Tietsche, S., Mogensen, K., & Mayer, M. (2019). The ECMWF operational ensemble reanalysis–analysis system for ocean and sea ice: A description of the system and assessment. *Ocean Science*, *15*(3), 779–808. https://doi.org/10.5194/os-15-779-2019